ADVANCED MATERIALS
www.advmat.de

Trends in Micro-/Nanorobotics: Materials Development, Actuation, Localization, and System Integration for Biomedical Applications

*Ben Wang, Kostas Kostarelos, Bradley J. Nelson, and Li Zhang**

Micro-/nanorobots (m-bots) have attracted significant interest due to their suitability for applications in biomedical engineering and environmental remediation. Particularly, their applications in in vivo diagnosis and intervention have been the focus of extensive research in recent years with various clinical imaging techniques being applied for localization and tracking. The successful integration of well-designed m-bots with surface functionalization, remote actuation systems, and imaging techniques becomes the crucial step toward biomedical applications, especially for the in vivo uses. This review thus addresses four different aspects of biomedical m-bots: design/fabrication, functionalization, actuation, and localization. The biomedical applications of the m-bots in diagnosis, sensing, microsurgery, targeted drug/cell delivery, thrombus ablation, and wound healing are reviewed from these viewpoints. The developed biomedical m-bot systems are comprehensively compared and evaluated based on their characteristics. The current challenges and the directions of future research in this field are summarized.

1. Introduction

The concept of miniature robots that can be actuated and localized inside the human body to help the diagnosis and treatment of diseases has been popular for decades.[1–7] Indeed, this was exactly the theme of the movie *Fantastic Voyage* (1966), in which a submarine and its crew were shrunk to the microscale so that they can voyage inside a patient's body for treatment of a blood clot. As nanoscience and nanotechnology are developing rapidly, functional nanomaterials form a bridge between robotics and nanomedicine through applications that feature the execution of assigned tasks in an on-demand manner through remote control by a programmable energy input.[1,4] Unlike traditional robots[8] that are larger in size, microrobots characteristically possess sizes less than 1 mm while nanorobots have sizes less than 1 µm. When the size of an object is reduced to the micro-/nanoscale, unexpected challenges may appear and thus, the propulsion of micro-/nano-objects in liquid environment is not as straightforward as those at the macroscale. Owing to their small size, m-bots can access complex and narrow regions inside human body, such as the distal of cerebral vessels and bile duct, which are sometimes inaccessible with existing minimally invasive medical devices and traditional robots, while being minimally invasive. Up to now, several micro- and nanoscale robots of different designs, types of functionalization, modes of actuations, and imaging strategies for localization and feedback have been reported for biomedical applications.[9–14]

It is worth mentioning that another type of nanorobot, known as molecular motor, has also been developed with proven potential for targeted drug delivery. As a typical molecular motor, DNA nanorobots are generally fabricated as initially folded structures with DNA aptamer-based locks. The locked DNA structure can be mechanically opened by certain proteins in the cells by the specific recognition of the sensing strand, typically the aptamer, causing the release of inner payloads for therapeutic purposes.[15–18] The targeting ability of DNA nanorobots primarily depends on the protein recognition of the aptamer whereas the targeting ability of programmed energy powered m-bots depends either on the energy supply strategies or the combined effect of energy supply and site recognition. Though molecular motors exhibit the typical features of robots to some extent, they are different from m-bots in that their function is

Dr. B. Wang, Prof. L. Zhang
Department of Mechanical and Automation Engineering
The Chinese University of Hong Kong
Shatin N.T., Hong Kong, China
E-mail: lizhang@mae.cuhk.edu.hk
Dr. B. Wang
College of Chemistry and Environmental Engineering
Shenzhen University
Shenzhen 518060, China
Prof. K. Kostarelos
Nanomedicine Lab
Faculty of Biology, Medicine & Health
The University of Manchester
AV Hill Building, Manchester M13 9PT, UK
Prof. K. Kostarelos
Catalan Institute of Nanoscience and Nanotechnology (ICN2)
Campus UAB, Bellaterra, Barcelona, Spain
Prof. B. J. Nelson
Institute of Robotics and Intelligent Systems (IRIS)
ETH Zurich
Tannenstrasse 3, Zurich CH-8092, Switzerland
Prof. L. Zhang
CUHK T Stone Robotics Institute
The Chinese University of Hong Kong
Shatin N.T., Hong Kong, China
The ORCID identification number(s) for the author(s) of this article can be found under https://doi.org/10.1002/adma.202002047.

DOI: 10.1002/adma.202002047

mostly limited to conformational motion. This review deals with the following aspects of energy powered m-bots: design, functionalization, actuation, localization, and application.

To navigate the miniature robots in a low Reynolds number environment where the inertia is negligible compared to the viscous force, special strategies should be designed for locomotion. Generally, micro- and nanorobots can be divided into biological, artificial, and biohybrid types depending on the material with which they are made. Biological m-bots are made of natural biological materials and show exceptional biocompatibility. Artificial m-bots may either be self-propelled or driven by an external field depending on the energy supplied. Self-propelled micro- and nanorobots generate the driving force directly from the surroundings and their driving mechanisms can be cataloged into self-electrophoresis-, self-thermophoresis-, self-diffusiophoresis- and microbubble-based propulsion.[19] The self-propulsion of m-bots is very attractive, however, some of the chemical fuels in the surrounding environment seriously restricted their practical applications in biomedical engineering due to the cytotoxicity of the fuels.[20–24] In contrast to self-propelled m-bots, external-field-propelled micro- and nanoscale robots, a type of m-bots that can be controlled using a remote, external field for steering and propulsion, has the advantage that it does not require the presence of chemical fuels inside the fluid environment.[25] External fields contain magnetic fields, electric fields, light, ultrasonic waves, Marangoni effect, and so forth.[26] Biohybrid m-bots combine the advantages of natural organisms, such as their geometry, auto-fluorescent properties, and biocompatibility, with the multifunctionality of artificial m-bots that results from the use of different materials.

M-bots have many attractive practical applications, such as cargo manipulation,[27,28] environmental remediation,[29–34] and targeted therapy,[35,36] and so on.[37,38] Surface functionalization is of critical importance for achieving biocompatibility and therapeutic efficiency. Specific functionalization processes based on both physical absorption and chemical grafting should be selected to endow the surface of the m-bots with certain polymers, proteins, and quantum dots (QDs) for completing various biomedical and environmental tasks.

Localization of the m-bots, especially for the in vivo situation, is also crucial for biomedical applications. A variety of imaging techniques, including fluorescent imaging (FI), computed tomography (CT), magnetic resonance imaging (MRI), ultrasonic (US) imaging, positron emission tomography (PET), and single-photon emission computed tomography (SPECT), have been investigated with regard to the localization of micro- and nanoscale robots. Benefiting from the synergy of localization and navigation, the resultant micro-/nanoscale robots can not only be tracked in real time in vitro and even in vivo, but also be used toward targeted delivery and therapy in specific locations with vision-based control. Moreover, the introduction of the movement of the micro-/nanoagents may also enhance the imaging contrast when compared with the static micro-/nanoagents. The combination of medical imaging techniques and actuation of the m-bots offers a brand-new active tool for targeting specific sites and performing medical procedures in a minimally invasive fashion.[39,40]

In a practical situation, the individual micro- and nanorobots may not have the capability to deliver enough drugs and cure the disease completely. Thus, the synergy and cooperation of a batch of micro- and nanorobots is important, and the motion control of a batch of m-bots differs widely from that of individual m-bots. Individual m-bots inside the swarming integration are not only governed by the external applied field/energy, but also influenced by their neighboring bots. In recent years, in addition to studying individual m-bots, the motion control of swarms has also been widely studied as they offer several advantages for practical biomedical applications.[41–43] First, swarm motion and control of m-bots are promising for the delivery of large doses of drugs, cargo materials, or cells, as well as energy such as the heat based on photothermal conversion and magnetic thermal conversion. Second, the swarming pattern may, as an entity, provide much better imaging contrast than that provided by individual agents at the micro- or nanoscale due to the accumulative effect, thereby facilitating the localization.[44] Therefore, apart from the individual micro- and nanorobots, the collective behavior of batches of m-bots and their application for in vivo delivery are separately discussed.

As shown in **Figure 1**, in this review, we examine five aspects of m-bots, namely, their design, functionalization, actuation, localization, and applications. The design of the m-bots is defined by their chemistry and geometry. The functionalization of the m-bots is depending on the types of cargos/molecules that are either physically anchored or chemically conjugated on the surface of the m-bots. The actuation is systematically summarized according to the type of energy for the propulsion, and the bots may be propelled using magnetic fields, ultrasonic fields, light, electric fields, fuel, heat, and the Marangoni effect. There are also hybrid m-bots and those propelled based on the collective behavior of the m-bots. The collective behavior of m-bots is dependent not only on the propulsion under the applied energy field, but also on the internal interactions between the individual m-bots. For in vivo tracking purpose, the localization of the m-bots is discussed based on the adopted medical imaging techniques and are classified into fluorescent imaging, MRI, US imaging, and radionuclide imaging. The applications, especially for the in vivo use of the m-bots, have been reviewed in terms of the following aspects: diagnostics, isolation and cell growth, targeted therapy with peroral and injected manners, thrombus ablation, and other bioapplications.

2. Design of m-Bots

2.1. Structure and Chemistry

Micro- and nanorobots can be divided into biological, artificial, and biohybrid types. Typical dimensions of a micro- and nanorobot can vary from dozens of nanometers to dozens of micrometers. Biological and biohybrid m-bots commonly contain natural organisms and are highly biocompatible; however, the difficulty in shaping them presents a considerable limitation. The majority of the m-bots are artificial m-bots, which are fabricated using either a top-down or a bottom-up strategy. Top-down strategies applied for m-bots fabrication include physical vapor deposition (direct deposition and glancing angle deposition), roll-up technique for the fabrication of micro/-nanotubes and helical microrobots, and 3D printing techniques such as direct laser writing.[69] The bottom-up strategies applied for m-bots fabrication include electrochemical/electroless deposition, wet chemical synthesis, and

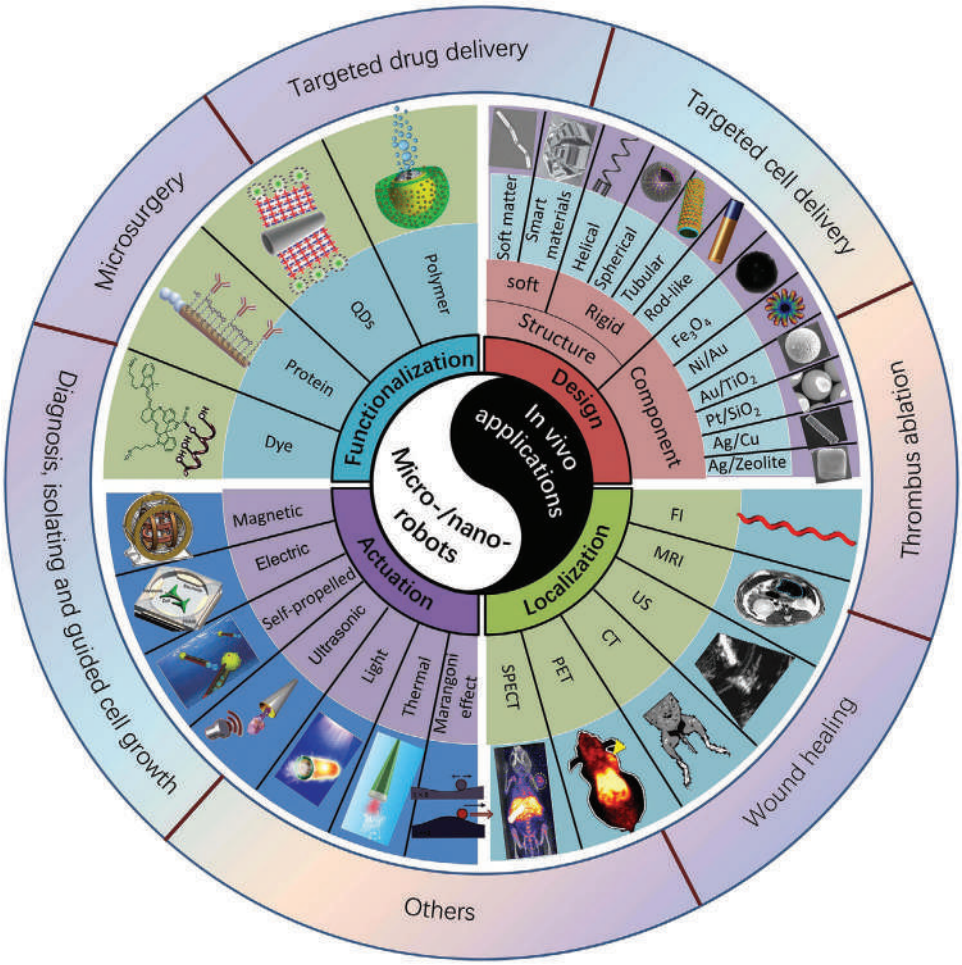

Figure 1. Schematic illustration of the types of m-bots for biomedical applications, classified into the design, functionalization, actuation, and localization (four aspects). Further details of the four aspects are depicted using images for a visual introduction. The in vivo applications of the m-bots are listed in the outer ring, including diagnosis, isolating and guided cell growth, microsurgery, targeted drug delivery, targeted cell delivery, thrombus ablation, and wound healing, and others. Figure created by the authors with the insets reproduced from the following references. Helical: Reproduced with permission.[45] Copyright 2012, Wiley-VCH; Tubular: Reproduced with permission.[46] Copyright 2014, American Chemical Society. Rod-like: Reproduced with permission.[47] Copyright 2017, Wiley-VCH. Ni/Au: Reproduced with permission.[48] Copyright 2005, Royal Society of Chemistry. Au/TiO_2: Reproduced with permission.[49] Copyright 2016, American Chemical Society. Pt/SiO_2: Reproduced with permission.[50] Copyright 2010, Wiley-VCH. Ag/Cu: Reproduced with permission.[51] Copyright 2016, Royal Society of Chemistry. Ag/Zeolite: Reproduced with permission.[52] Copyright 2015, Wiley-VCH. Soft matter: Reproduced with permission.[53] Copyright 2016, Wiley-VCH. Smart materials: Reproduced with permission.[54] Copyright 2009, National Academy of Sciences. Functionalization, Dye: Reproduced with permission.[44] Copyright 2015, Wiley-VCH. Polymer: Reproduced with permission.[55] Copyright 2014, American Chemical Society. QDs: Reproduced with permission.[56] Copyright 2015, Royal Society of Chemistry. Protein: Reproduced with permission.[57] Copyright 2011, Wiley-VCH. Actuation, Electric: Reproduced with permission.[58] Copyright 2016, Springer Nature. Self-propelled: Reproduced with permission.[59] Copyright 2018, Wiley-VCH. Ultrasonic: Reproduced with permission.[60] Copyright 2012, Wiley-VCH. Light: Reproduced with permission.[61] Copyright 2016, Wiley-VCH. Thermal: Reproduced with permission.[62] Copyright 2017, American Chemical Society; Marangoni effect. Reproduced with permission.[63] Copyright 2017, Wiley-VCH. Localization, FI and MRI: Reproduced with permission.[64] Copyright 2017, AAAS. CT and SPECT: Reproduced with permission.[65] Copyright 2017, Royal Society of Chemistry. US: Reproduced with permission.[66] Copyright 2014, SAGE. PET: Reproduced with permission.[68] Copyright 2015, American Chemical Society.

self-assembly process. All fabrication methods of the m-bots will run through the review.

The design of the artificial m-bots includes the structural design and component design. On the basis of structure, artificial m-bots may be divided into rigid and soft, and on the basis of their appearance, into micro-/nanospheres, rigid/flexible nanowires, micro-/nanotubes, helical m-bots, and microbullets, as shown in **Figure 2**.[70–86] Rigid m-bots have been extensively investigated in the past decades, while the attention has been shifted to soft m-bots in recent years due to their overwhelming advantages that can interface with the human body and adapt to unpredictable surroundings when they are used for biomedical applications.[87–97] Soft m-bots can be further classified into active soft matter and smart materials.

Active soft matter refers to the soft-bodied m-bots fabricated using the polymers and organic components. The modulus and stiffness of the soft matter is generally comparable to real biological cells, tissues, and organs, making the as-fabricated m-bots resemble biological material more closely and thus, making them more suitable for biomedical applications. Some of the soft-bodied robots can change shape during the navigation.[98] Smart materials do not simply integrate soft matter into their design, but is also

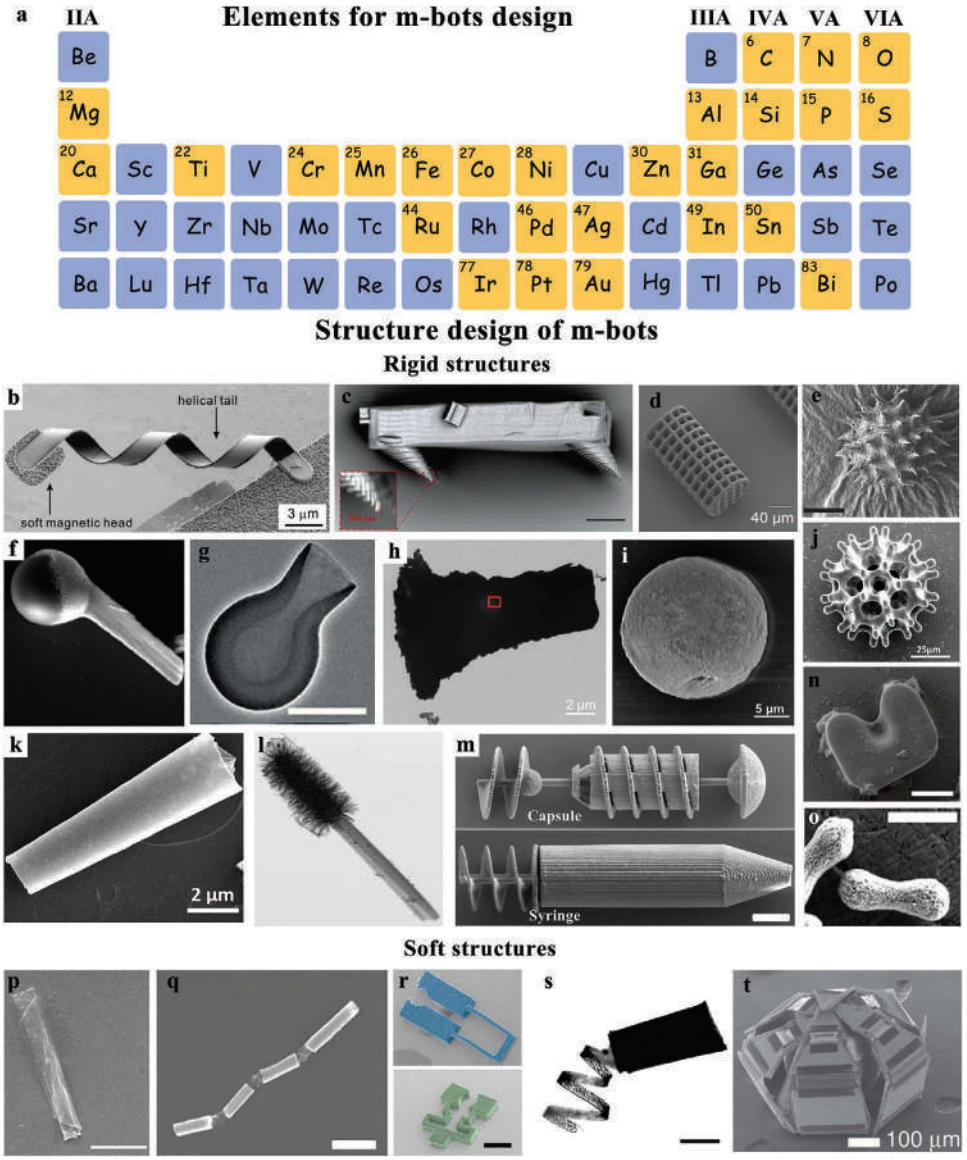

Figure 2. a) Periodic table (partial) shows the elements favored in the composition design of m-bots. The highlighted elements with the orange boxes represent the elements that are frequently applied for design of m-bots. b) FESEM image of an artificial bacterial flagellum. Reproduced with permission.[109] Copyright 2009, American Chemical Society. c) SEM image of the microwalker. Scale bar is 10 μm. Reproduced with permission.[110] Copyright 2015, Wiley-VCH. d) SEM image of a cylindrical-shaped microrobot. Reproduced with permission.[111] Copyright 2015, Wiley-VCH. e) SEM image of a Janus sporopollenin exine capsules micromotor partially coated with Pt. Reproduced with permission.[112] Copyright 2017, American Chemical Society. f) SEM image shows the Pt-coated microbead with a TiO_2 arm. Reproduced with permission.[113] Copyright 2011, American Chemical Society. g) TEM image of a single carbonaceous nanobottle motor. Reproduced with permission.[114] Copyright 2018, Wiley-VCH. h) TEM image of a T7 AuNS (PAH/PSS)20 PtNP microengine. Reproduced with permission.[46] Copyright 2014, American Chemical Society. i) SEM image of a representative red blood cell membrane-coated magnesium Janus micromotor. Reproduced with permission.[115] Copyright 2015, Wiley-VCH. j) SEM image of the burr-like porous spherical microrobot. Reproduced with permission.[116] Copyright 2018, AAAS. k) SEM image of torpedoes microrobots. Reproduced under a Creative Commons Attribution 4.0 International License.[117] Copyright 2017, The Authors, published by Springer Nature. l) TEM image of an individual Janus nanotree. Reproduced with permission.[85] Copyright 2016, Springer Nature. m) SEM images of 3D printed microcapsule (top) and microsyringe (bottom). Scale bar is 20 μm. Reproduced with permission.[118] Copyright 2015, Wiley-VCH. n) SEM image shows the U-shaped microrobot that can be actuated by magnetic field gradient. Reproduced with permission.[119] Copyright 2013, SAGE. o) SEM image of the hematite peanut microparticles. Scale bar is 1 μm. Reproduced with permission.[120] Copyright 2013, American Chemical Society. p) SEM image shows the rolled-up polyelectrolyte multilayer microrockets. Scale bar is 10 μm. Reproduced with permission.[59] Copyright 2018, Wiley-VCH. q) SEM image of a multilinked artificial nanofish. Scale bar is 800 nm. Reproduced with permission.[53] Copyright 2016, Wiley-VCH. r) SEM images of two types of untethered magnetic microgripper that are deformable based on magnetic torque and magnetic force, respectively. Scale bar is 500 μm. Reproduced with permission.[121] Copyright 2014, Wiley-VCH. s) Optical image of a flagellated soft microrobot. Scale bar is 500 μm. Reproduced under a Creative Commons Attribution 4.0 International License.[122] Copyright 2016, The Authors, published by Springer Nature. t) SEM image of a thermo-biochemically actuated microgripper. Reproduced with permission.[54] Copyright 2009, National Academy of Sciences.

adaptable and changeable throughout their entire structure (such as spring-mass systems) or at the predesigned hinges (such as segmented micro-/nanostructures with several soft joints)[99–101] when they are exposed to external stimuli like heat, light, ultrasound, magnetic field, electric field, and mechanical force. Li et al.[102] developed a magnetic nanorobot with two soft linking arms that can perform "freestyle" swimming even in liquids with low Reynolds number. The degrees of freedom of these soft robots during motion are much higher than that of the rigid robots.

The component design of the m-bots should also depend on the propulsion regime. In the case of magnetically actuated m-bots, magnetic materials such as Fe_3O_4, Ni, γ-Fe_2O_3, and FePt,[28,45,54,103] should be considered. For bubble-propelled m-bots in the environment that contains fuel, catalytic materials such as Au, Pt, Ag, MnO_2, TiO_2, and enzyme may need be used to obtain asymmetric bubble propulsion. In self-propelled m-bots without bubble release, robots with anisotropic geometry or composition, commonly called Janus particles, are usually applied. Currently, the design and fabrication of micro- and nanorobots mainly depend on ≈20 elements and most of them are the transition metals with a few coming from main group, as shown in Figure 2a (the frequently used elements in m-bot design are highlighted with orange boxes). In the future, design and fabrication may be realized by exploring other multifunctional elements.

2.2. Biocompatibility and Biodegradability

The biocompatibility and biodegradability of the building blocks of the micro-/nanomachines should be also satisfied during the design stage, which can be deduced according to the elementary properties. Generally, biodegradable materials are preferred during the design since they disappeared gradually after use without any postremoval process. These materials can be degraded into noncytotoxic solute in the biological environment and show little harm to the human body while they are controlled to a moderate amount. In fact, when limited to the relatively mild environment of the biological environment, only a small part of the materials shows biodegradability. Several biodegradable micro-/nanomachines have been developed as building blocks/functional layers for in vivo uses, such as the inorganic materials like Mg, Zn, and $CaCO_3$, and organic materials such as polydopamine, polysaccharides, liposomes, and hydrogel gelatin methacryloyl,[104] which will be illustrated based on the different catalogs of applications in the Section 6. In most cases, the applied materials cannot be maintained to be biodegradable because of the diverse requirements for actuation, imaging, and applications. Anyhow, the building blocks of the micro-/nanomachines should fulfill the minimum requirement of biocompatibility during the design.

2.3. Robot Size

The size of the robots may be another important aspect for biomedical applications since it directly determines the final direction in which the m-bots have proceeded in vivo. There are several biological barriers such as the blood-brain barrier, vascular endothelial barrier, and glomeruli filter that prevent the passage of m-bots of specific sizes.[105] For the nanorobots with a small enough size, they may be discharged from the body with the kidney removal regime. As for the larger m-bots, they may be captured by the immune cells in the circulatory system such as the monocytes, leukocytes, platelets, and dendritic cells, and in the tissues/organs such as the resident phagocytes. The resident phagocytes are of various types and exist in many organs, including the Kupffer cells in the liver, alveolar macrophages in the lung, and B cells in the spleen.[106,107] Accordingly, the size of the micro-/nanomachines should be taken into consideration for clearance during the design of the m-bots.

In addition, the size of the m-bots can also affect the localization and motion during the remote control. The motion of the microscale robots and nanoscale robots is quite different. As the robot size decreases, the interference caused by Brownian motion becomes increasingly obvious. The random changes in the direction of motion, caused by Brownian motion of the nanorobots, make the trajectories much more disorganized and disordered than that of the microrobots. The trajectories originate from the guided actuation, and in some cases, should be assessed by analyzing the statistics, instead of by intuitive evaluation.[108]

3. Functionalization of m-Bots

The functionalization of the m-bots is a crucial step to endow the m-bots with extra functionalities to perform distinct tasks other than navigation. For bioapplications, the functionalization process can be applied not only toward targeted delivery/therapy but also for the visualization and tracking (i.e., localization) of the m-bots both in vitro and in vivo. Moreover, the functionalization process also improves the biocompatibility and prevents the immune system from recognizing m-bots as foreign objects and attacking them, which would increase the retention time in vivo. To date, several functionalization strategies and methods have been explored for specific bioapplications via both physical absorption and chemical bonding to absorb and anchor molecules of drugs, polymers, proteins, and QDs onto the m-bots.[123,124,125]

Wang et al.[126] proposed a self-propelled Au/Ni/PANI/Pt microtubular device via a template-based method and followed it up with functionalization with concanavalin A lectin bioreceptor for the recognition of *Escherichia coli*. The authors found that the m-bots are extremely effective for the easy real-time isolation of *E. coli* in a fuel-enhanced environment and clinical samples as illustrated in **Figure 3**a. The captured *E. coli* could also be released from the tubular microrobots in the solution with low pH because of the dissociation of the sugar-lectin complex. Apart from the protein, the grafting of polymer on the m-bots can also facilitate their bioapplications. Guan et al.[55] developed Mg/Pt-poly(*n*-isopropylacrylamide) (PNIPAM) Janus micromotors that show autonomous motion in simulated body fluids and blood plasma and can effectively uptake, transport, and affect the temperature-controlled release of drugs due to the partially functionalized thermoresponsive PNIPAM polymer layers (Figure 3d). Other polymers, such as PEG, have been widely applied for the functionalization of m-bots for the enhancement of the biocompatibility. To further enhance the biocompatibility and prevent the immune system from recognizing the micro-/nanodevices as foreign molecules and attacking them, the researchers developed strategies to coat the micro-/nanodevices with cell membranes.[127–132] Conversely, bacteria membranes can be also utilized for coating the m-bots to enhance the phagocytosis by

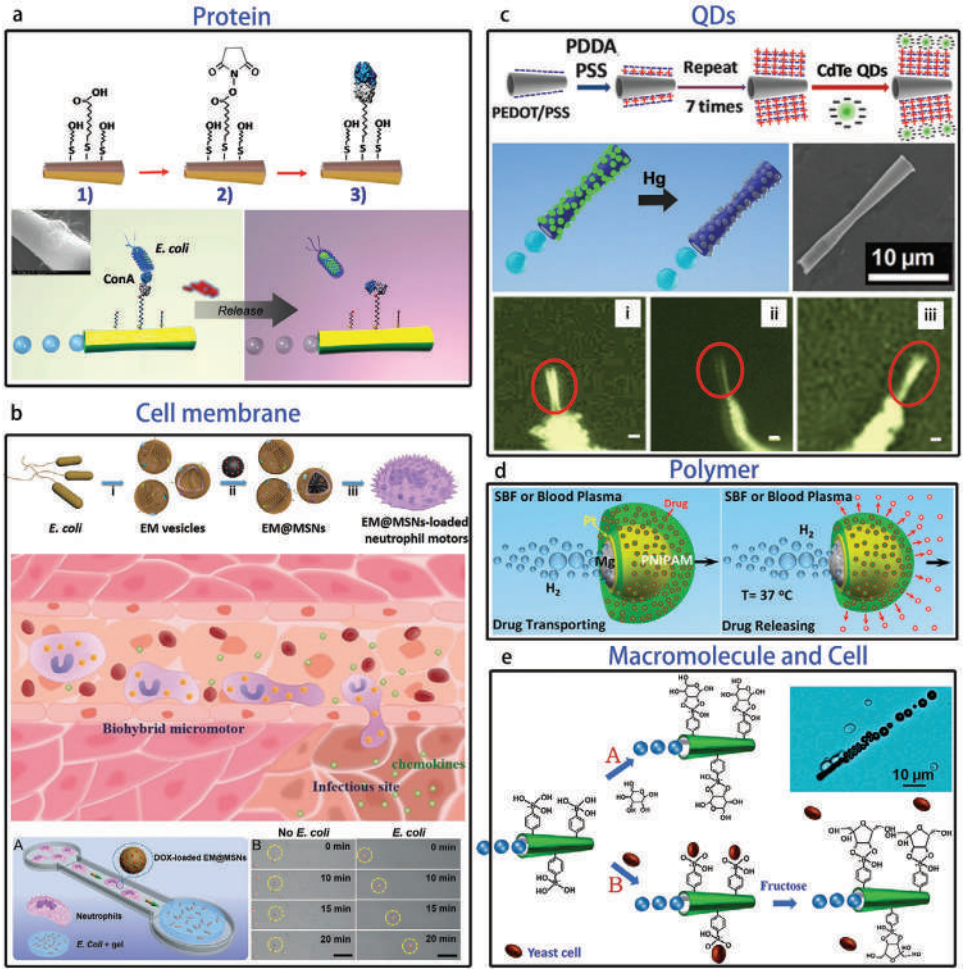

Figure 3. a) Schematic of the functionalization procedure of protein (concanavalin A lectin bioreceptor) on the microtube for the recognition of *E. coli*. Reproduced with permission.[126] Copyright 2012, American Chemical Society. b) Schematic of the fabrication of the hybrid neutrophil microrobots composed with mesoporous silica NPs coated with *E. coli* membranes. Reproduced with permission.[133] Copyright 2017, Wiley-VCH. c) Schematic of the functionalization procedure of the CdTe QDs on to the tubular micromotor via electrostatic self-assembly process. Schematic and fluorescent images of a QDs functionalized microrobot before and after 30 s locomotion in solutions containing Hg^{2+} (3 mg L^{-1}) and Pb^{2+}+Cu^{2+} (5 mg L^{-1}), demonstrating the selective detection of the Hg^{2+}. Scale bar is 2 mm. Reproduced with permission.[56] Copyright 2015, Royal Society of Chemistry. d) Schematic of the temperature-caused controlled drug releasing by Mg/Pt-PNIPAM Janus micromotors. Reproduced with permission.[55] Copyright 2014, American Chemical Society. e) Schematic of the poly(3-aminophenylboronicacid)/Ni/Pt microrocket and the interaction with glucose and yeast cell along with fructose triggered release of the cell. Reproduced with permission.[134] Copyright 2012, American Chemical Society.

the phagocytic cell. He et al.[133] developed a kind of chemotaxis-guided hybrid neutrophil microrobots fabricated from the camouflaging approach of the drug-loaded mesoporous silica NPs with the *E. coli* membranes and followed it by phagocytosis by the neutrophils because of their characteristic chemotaxis capability (Figure 3b). This type of chemotaxis-guided hybrid neutrophil microrobots exhibit good cellular activity and motility, and can be applied for enhanced neutrophil-guided drug delivery for targeted therapy. The functionalization of the m-bots with the cells on them was also proposed by Wang et al.,[134] who proposed a poly(3-aminophenylboronic acid)/Ni/Pt microtube functionalized by a boronic acid-based outer layer with an inner platinum layer. The outer boronic acid layer could perform selective monosaccharide recognition while the inner platinum worked for catalyst-based propulsion. The resultant microrobots could recognize and bind to the yeast cells and glucose and transport them in the media (Figure 3e). The DNA flagella was also anchored onto the magnetic microparticles by Maier et al.[135] using a self-assembly process to the flexible tails which made the microswimmer easily steerable by the external magnetic field. In addition to the organic agents and organisms, the inorganic functional nanoparticles can also be anchored to the m-bots with ease. Sanchez et al.[56] proposed tubular microrobots which were functionalized with QDs via electrostatic self-assembly for the real-time optical visualization due to the fluorescence property of the QDs (Figure 3c).

4. Actuation of m-Bots

The actuation of m-bots is essentially the energy conversion that transforms various energy, such as magnetic energy, electric energy, light energy, and chemical energy to kinetic energy. The kinetic energy of m-bots can be used for several

Table 1. Summary of the features of the mainstream actuation systems toward the biomedical applications.

Actuation field	Features	Notice for biomedical applications
Magnetic field	High penetration of tissue and body Multiple motion modes for adapting different environments, including corkscrew motion in suspended environment and tumbling motion in boundary condition Collective motion of the magnetic agents for collaborative purpose in realizing an assigned task and dynamic contrast Precise and multi-dof control of the tiny robots Safe and good biocompatibility	Attenuation with distance Applicable for the patients without metal implants (such as pacemaker)
Acoustic field	High penetration of tissue and body Broad selectivity of the motor materials Fast response and long lifetime Locally aggregating effect Can trigger instantaneous ejection of tiny agents with ultrahigh speed Good biocompatibility Safe	Heat generation during the actuation
Light field	Can be focused and scattered for collaborative tasks by multiple agents High motion speed of individual robot	Applicable for superficial tissue Suitable for sensing and diagnosis
Fuel	Biochemical fuels such as enzyme-triggered biocatalytic reaction are safe and biocompatible No external actuation system/setup is required High motion speed Chemotaxis	Bubble-propelled motors (e.g., Mg and $CaCO_3$) are promising in the gastrointestinal disease and wound healing with low cytotoxicity and no further removal is required for clearance
Electric field	Contact free and the low-cost of the set-up	Applicable in ionic media such as the interstitial fluid and blood
Marangoni effect	Surface energy guided motion of the tiny agents in contact free mode	Applicable for in vitro applications
Magnetic field + Acoustic field	High penetration of tissue and body Collective behavior with locally enhanced contrast and dose Reversible swarming behavior Safe Untethered Good biocompatibility	Applicable for the patients without any metal implants
Magnetic field + Fuel	Steerable with high motion speed High penetration of tissue and body Untethered	Combine the high speed of fuel powered motion and high precision of magnetic field actuation Applicable for the patients without any metal implants

types of specific motion forms such as rectilinear motion, circular motion, and spiral motion. According to the forms of the supplied energies, the m-bots can be divided into self-propelled and external field-propelled types. In self-propelled m-bots, the energy is generally supplied by water, H_2O_2 solution, and acidic solutions. The reported m-bots actuated by the concentration gradient, self-electrophoresis, and bubbles all belong to the chemical-powered/self-propelled m-bots. The external field-propelled m-bots are powered by the external magnetic/electric/ultrasonic field and do not need chemical fuels inside the environment, making them much more suitable for bioapplication compared with the chemical-powered ones. **Table 1** summarizes the features of mainstream actuation systems for biomedical applications. The following sections will pay more attention to the introduction of the m-bot actuation based on the requirements of the biomedical applications.

4.1. Magnetic Field-Propelled m-Bots

Magnetic field-propelled m-bots can transform magnetic energy into mechanical energy in the form of the magnetic field gradient and magnetic torque, to realize their specific applications like cargo manipulation and transportation, targeted/directed therapy, and environmental remediation. Since low-intensity magnetic fields are regarded as harmless to living organisms, m-bots actuated and steered by external magnetic fields show great promise for in vivo applications. Basically, the magnetic force (F) and magnetic torque (T) on a magnetic object inside a magnetic field can be expressed as[137]

$$F = V(M\cdot\nabla)B \tag{1}$$

$$T = VM\times\mathbf{B} \tag{2}$$

Therein, V is the volume of the magnetic object, $\boldsymbol{M}$ represents the magnetization and $\boldsymbol{B}$ represents the magnetic flux density. From the above equations, we can conclude that the magnetic force on a magnetic object is zero under a uniform magnetic field. The magnetic torque on the magnetic object depends on the direction of the magnetic dipole moment and the external magnetic field. In order to obtain a continuous motion of a magnetic object, the magnetic field must be either temporal-varying or spatial-varying. Rotating, oscillating, and pulsed magnetic fields belong to the category of temporal-varying magnetic fields, while gradient magnetic field is a typical spatial-varying magnetic field. Based on the type of magnetic

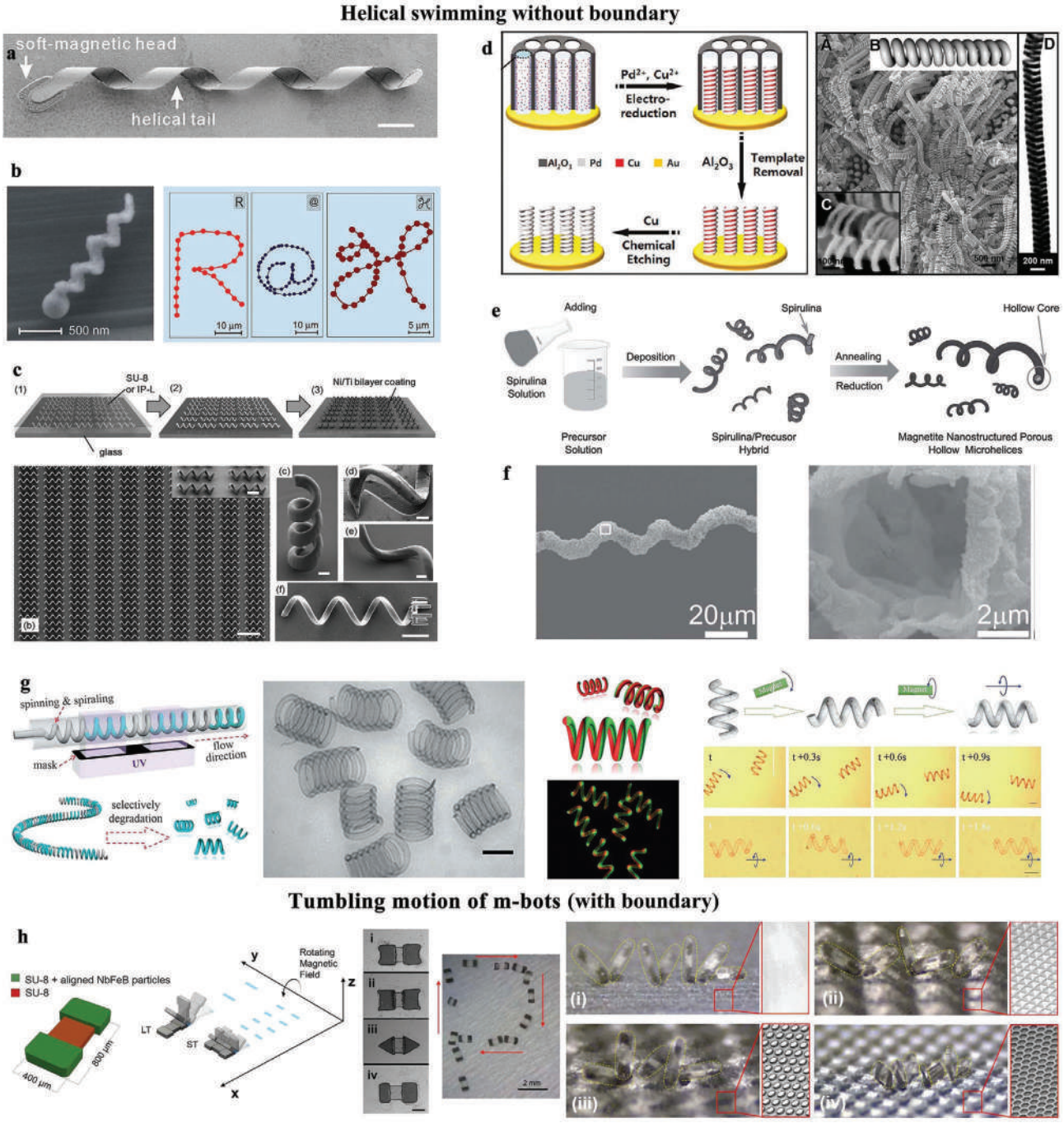

Figure 4. a) FESEM image of the artificial bacterial flagella with InGaAs/GaAs/Cr helical tail. The scale bar is 4 μm. Reproduced with permission.[143] Copyright 2006, American Chemical Society. b) SEM image shows the helical nanorobots fabricated by GLAD and the trajectories of individual nanoswimmers navigate the preprogrammed "R@H" tracks in solution. Reproduced with permission.[144] Copyright 2009, American Chemical Society. c) Fabrication procedure of helical microrobots by direct laser writing and the SEM images of the prepared microrobots. Reproduced with permission.[45] Copyright 2012, Wiley-VCH. d) Schematic of the fabrication process of helical microstructures by template-based electrodeposition and SEM image of large numbers of Pd nanosprings fabricated based on commercial AAO template. Reproduced with permission.[153] Copyright 2011, American Chemical Society. e) Fabrication process of the porous hollow microhelices by biotemplate method and the SEM and TEM images f) of the prepared sample. Reproduced with permission.[155] Copyright 2015, Wiley-VCH. g) Schematic of the fabrication of the helical microrobots. SEM image of the prepared helical microrobots. Scale bar is 300 μm. Confocal laser scanning microscopy image of the prepared Janus helical microrobots. Magnetic rotation and corkscrew motion of the helical microrobots incorporated with magnetic NPs. Reproduced with permission.[157] Copyright 2017, Wiley-VCH. h) Schematic of the magnetic tumbling microrobots and the tumbling modes (lengthwise tumble and sideways tumble can be performed depending on the alignment of the magnetic agents) under a rotating magnetic field. Optical images show different geometries of the magnetic tumbling microrobots. Optical image shows the programmable trajectory of a rounded rectangle tumbling microrobot with "P" shape. Navigation of the tumbling microrobots on various terrains (flat paper, cylindrical bumps, knurled surface, and honeycomb terrain) in dry environment with field strength of 10 mT and frequency of 0.5 Hz. Reproduced under the terms of the Creative Commons CC-BY license.[167] Copyright 2018, The Authors, published by MDPI.

field, and inspired by the motion of natural microorganisms, various magnetic field-actuated m-bots/actuators have been developed,[136–141] including the m-bots driven by the magnetic force (F) and the magnetic torque (T).

With the simple magnetic force (F) generated with a nonuniform magnetic field, the magnetic objects can be actuated along the direction of magnetic field, regardless of their geometry and structure. Another typical magnetic field-actuated m-bot is the magnetic torque-(T) powered propulsion in a uniform magnetic field with changing field direction. Artificial bacterial flagellum is a kind of typical magnetic m-bot that can be actuated under a uniform rotating magnetic field. The theory related to the magnetization and propulsion of helical m-bots under a rotating magnetic field is well established by Morozov and Leshansky.[142] The helical m-bots are either made of uniformly magnetic materials or composed of magnetic heads and helical tails. In 2006, Zhang et al.[143] fabricated a micro-artificial bacterial flagellum that contains a magnetic Cr/Ni/Au head and an InGaAs/GaAs helical tail based on the self-crimping technique (**Figure 4**a). The artificial bacterial flagellum can be actuated to move ahead, turn a corner, and move back under a uniform rotating magnetic field with a translational speed of 4.6 μm s^{-1} in DI water. Thereafter, researchers have developed many other methods, such as glancing angle deposition (GLAD) (Figure 4b),[144–146] direct laser writing (Figure 4c),[45,147–151] template-based electrodeposition (Figure 4d),[152–154] natural-template method (Figure 4e,f),[155,156] flow lithography integrated microfluidic spinning and spiraling system (Figure 4g)[157] to fabricate the magnetic helical robots with smaller size[144] and environment oriental properties.[122] Fischer et al.[144,146,147] fabricated a nanoscale helical swimmer with a diameter of only 200–300 nm and a length of only 1–2 μm using the GLAD technique. It is the smallest helical robot fabricated to date, and can be precisely controlled under a magnetic field to reach a speed of 40 μm s^{-1}. Zhang and Nelson et al.[45] developed the direct laser writing method to fabricate helical microswimmers one by one on a substrate, followed by the vapor deposition of Ni and Ti. Magnetic microswimmers show good biocompatibility and can be actuated in water with a speed of up to 180 μm s^{-1}. Park et al.[153] also fabricated the Pt helical structure by electrodeposition on the anodic aluminum oxide template. Gao et al.[154] applied spiral xylem vessel plant fibers as the natural template and fabricated the microhelical swimmers after the e-beam evaporation process of Ti/Ni. Yan et al.[155] used *Spirulina* as the biotemplate to fabricate the biocompatible helical microrobots via a coprecipitation method. The flow-lithography integrated microfluidic spinning and spiraling system was also designed by Zhao et al.[157] for the continuous generation of helical microrobots. With the method, the length, diameter, and pitch of the helical microrobots could be precisely controlled. The helical microrobots could be imparted with Janus, triplex, and core–shell structures with ease from the fast-online gelation and polymerization by UV illumination. After spatially controlling the encapsulation of NPs in the helical structure, the helical microrobots could be actuated not only in the manner of fuel-free magnetic rotation and corkscrew motion but also through fuel-catalyzed bubble propulsion mode. Although the helical magnetic m-bots can be efficiently propelled under a uniform rotating field, the design and fabrication procedures are complicated and time-consuming. In recent years, several research groups have developed much simpler designs and structures that perform well under a rotating field without any boundary, including the ensemble of beads,[158–160] planar structures,[161–163] and even randomly arranged clusters.[104–106] In comparison with the helical m-bots, these simpler designs and structures possess their advantage in that they can be mass produced due to the simple designs and fabrication approaches.

In a practical situation, the magnetic micro-/nanoagents may not reside in a suspended state and have boundary interactions with respective boundaries of the confined spaces. The magnetic micro-/nanoagents can, therefore, be navigated using an external magnetic field; this is true even in a uniform case, in the form of tumbling/rolling which benefits from the boundary interaction forces. Cappelleri et al.[167] developed magnetic tumbling microrobots by photolithography with various geometrical shapes that can be navigated on complex surface topographies with precise trajectory (Figure 4h). The microtumblers use friction to grip the surface and move forward. They can not only tumble into the valleys but also climb steep inclines. Apart from the actuation and control of individual microrobots, magnetic tumbling is also applicable for the swarming of a batch of m-bots (will be introduced in Section 6.6). This mode of magnetic motion shows its advantages in universality in terms of a wide selection of magnetic-objects and applicability of various surface topographies.

4.2. Ultrasonic Field-Propelled m-Bots

Ultrasound field, when used as external energy input to m-bots, can realize noninvasive and on-demand motion control with long lifetime and good biocompatibility. Control and actuation of the m-bots by ultrasound, therefore attracted extensive attention during the past decades.[168–175] The m-bots suspended in the solution are driven by the acoustic radiation forces that consist of a primary radiation force (responsible for the migration of m-bots) and a secondary radiation force (responsible for the repulsion and attraction between the m-bots).[168] The ultrasound field-related actuation is adaptable for various m-bots including the propulsion of metallic nanowires and tubular microagents, rotation of microbeads, and the patterning of nanoparticles.[168] Mallouk et al.[169] developed a kind of nanowire via template-assisted electrodeposition on the AAO substrate, and the nanowire could be levitated into node plane with an adjustable random motion speed by the MHz frequency acoustic waves through the variation of the amplitude and frequency of the acoustic wave. The asymmetry of the nanorods in the composition/geometry can lead to unidirectional motion of the nanorobots, which is attributed to the self-acoustophoresis mechanism. Ultrasound can also offer precise and reversible control of the motion speed of the chemical-powered m-bots. Wang et al.[170] found that the bubble-propelled microrobots respond to the ultrasound field instantaneously for the speed modulation. While the ultrasound field is applied on the bubbling tubular microrobots, the generated O_2 inside the catalytic tubular microrobots is ejected immediately without the growth process and the gas was driven to the nodes/antinodes, causing the microrobots to stop. Different from the rigid m-bots, Nelson et al.[171] described a flexible nanoswimmer composed of a rigid

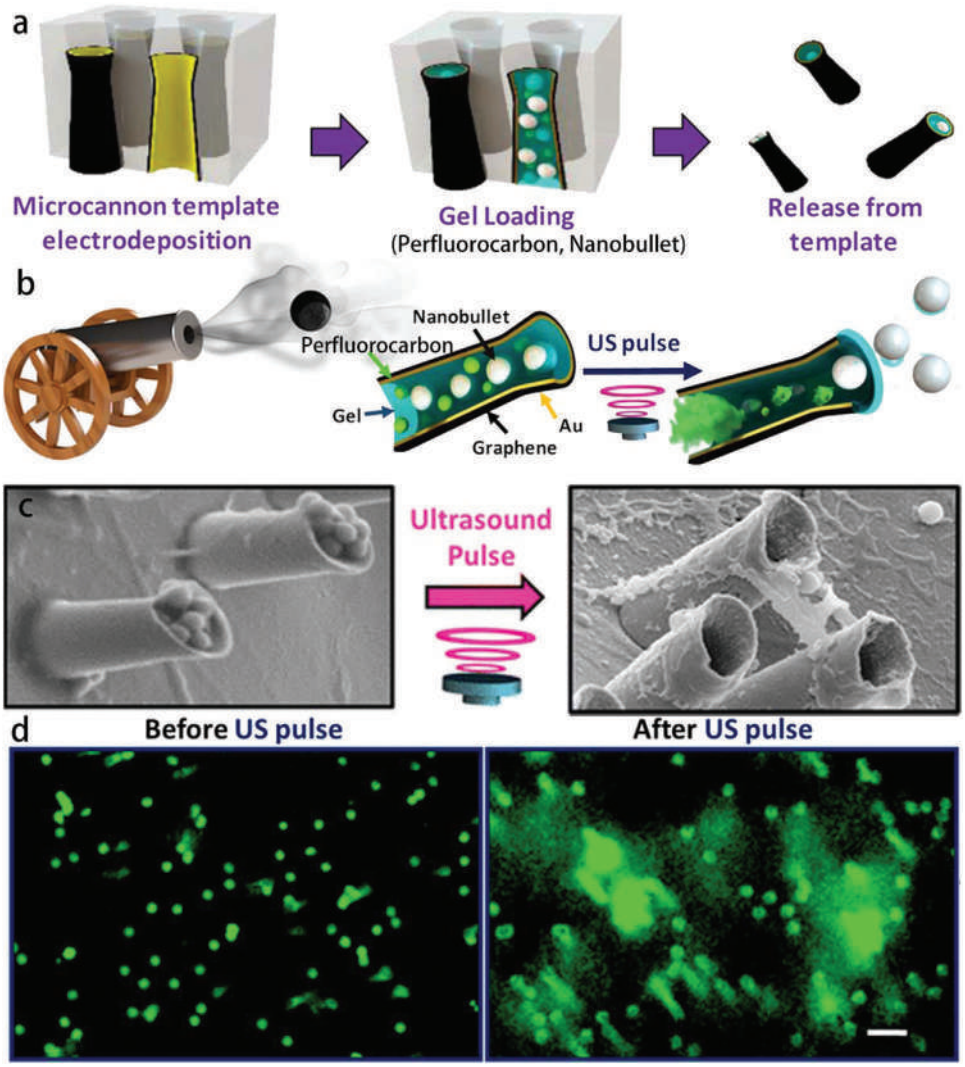

Figure 5. a) Schematic illustration of the fabrication procedure of microcannons by template electrodeposition and the loading of cargos by infiltrating them inside a gel matrix into the interior of the microcannons. b) Schematic illustration of the firing of nanobullets inside the microcannons. c) SEM images show the microcannons loaded with nanobullets before and after the US triggered firing. d) Fluorescence images show the fluorophore loaded in microcannons before and after the US triggered firing. Reproduced with permission.[176] Copyright 2016, American Chemical Society.

bimetallic head and a flexible tail. The flexible microswimmer can be propelled by the small-amplitude oscillation of its flexible tail in both the standing and traveling acoustic waves which may facilitate in vivo uses of the US-propelled m-bots since it is may be hard to form predictable standing waves in vivo.

Apart from the sustainable actuation of the m-bots, the ultrasound field could trigger an instantaneous ejection of the micro-/nanoobjects with ultrahigh instantaneous speed, which might be in favor of the penetration of the tissue barriers. Wang et al.[176] developed a controlled and powerful microballistic tool that realized the loading and firing of nanobullets, such as silica and fluorescent microspheres, using electrochemically fabricated microcannons (**Figure 5**a) via acoustical trigger action. The focused ultrasound pulse could cause the spontaneous evaporation of the perfluorocarbon emulsions of the nanobullets; the nanobullets were ejected at a remarkably high speed, as shown in Figure 5b. Figure 5c,d shows the SEM images and fluorescent images of the microcannons before and after the US pulse trigger action. The strategy not only offered a controlled firing method of nanobullets from a microstructure but also provided improved accessibility to target locations and enhanced tissue penetration for in vivo applications.

4.3. Light-Propelled m-Bots

Light, as an environment friendly and renewable energy source, shows its unique merits in the actuation of m-bots based on the light-sensitive molecules and atoms.[177,178] Compared with other external fields such as magnetic, electric, and ultrasonic, the light field is generally a highly localized field with a focused light beam that is favorable for conducting collaborative tasks by a group of m-bots, which is intensively reviewed in Section 4.7.[179–182] Due to the limitation of the penetration depth of the tissue, the

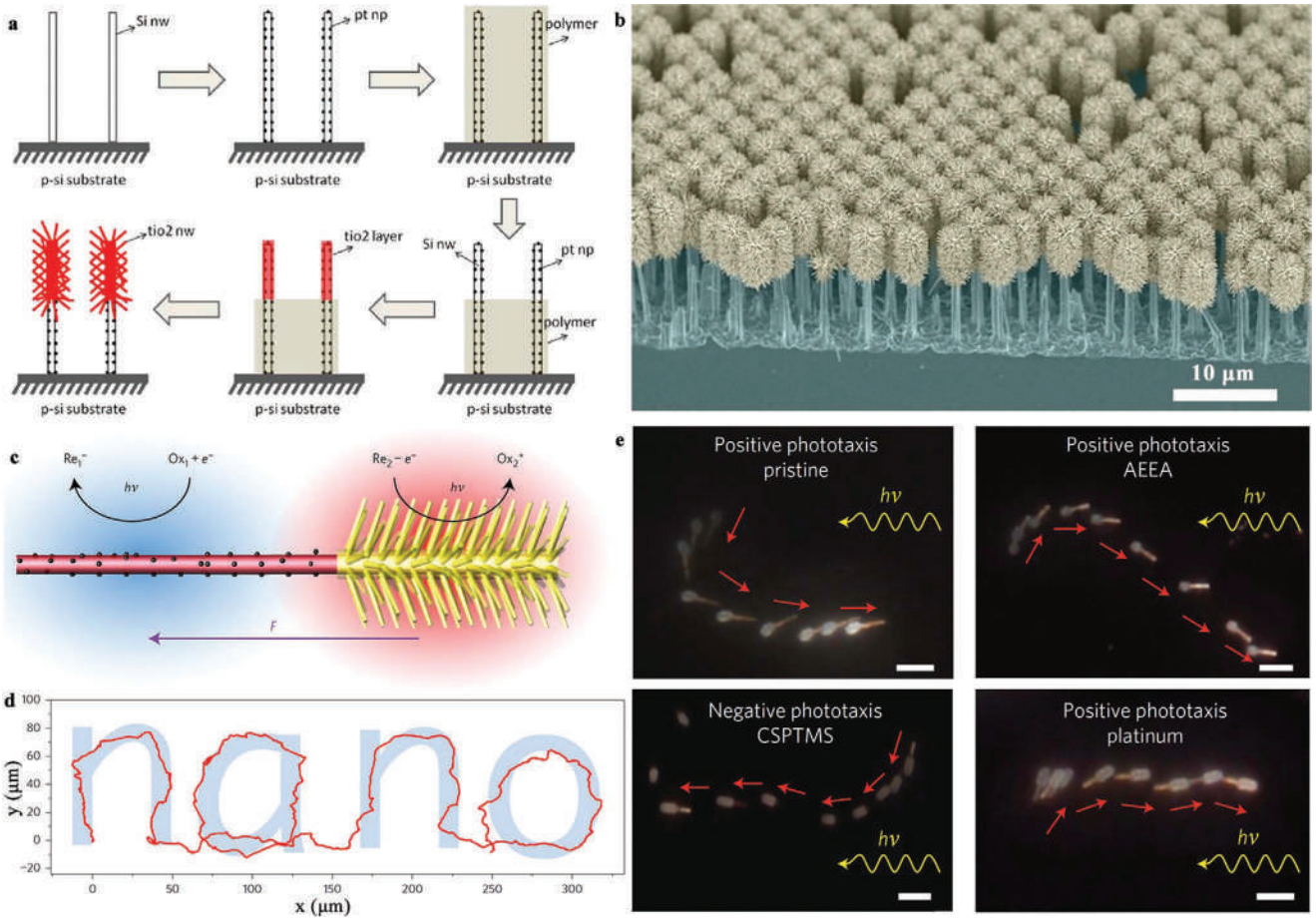

Figure 6. a) Schematic of the fabrication procedure of TiO_2/Si Janus nanotree. b) False-colored SEM image of the Janus nanotree forest prepared on Si substrate. c) Schematic of the propulsion mechanism of the Janus nanotree under illumination. The photoexcited minority carriers drive the photoelectrochemical reaction on the nanotree surface and the electric field generated by the unbalanced ions propels the charged nanotree forward. d) Controlled locomotion of a nanotree. e) Superimposed images of the top two images show the original and 3-[2-(2-aminoethylamino)-ethylamino]-propyltrimethoxysilane- (AEEA, positive charged) treated Janus nanotrees migrate in tail-forward form with positive phototaxis. The bottom left image shows the 2-(4-chlorosulfonylphenyl)ethyltrimethoxysilane (CSPTMS, negative charged) treated Janus nanotree migrates in head-forward form with negative phototaxis. The right bottom image shows the Pt NPs coated Janus nanotree migrates in head-forward form with positive phototaxis. Reproduced with permission.[85] Copyright 2016, Springer Nature.

light-propelled micro-/nanomachines are extremely suitable for diagnosis and treatment at near-skin positions. The structures of the m-bots contain Janus spherical micro-/nanoparticles,[183–188] rod/wire-like m-bots,[189–191] tubular micro-/nanomotors, and other irregular structures with diverse motion modes, including self-electrophoresis, self-thermophoresis, and self-diffusiophoresis. All the motion generated from the energy conversion of the external light energy to the mechanical energy of the m-bots due to the light caused nonuniform gradient field (such as concentration, thermal field, and electric field) around the m-bots. The nonuniform gradient field can be generated by either the nonuniform light field or the asymmetric structure of the m-bots. As the nonuniform light field can be applied to actuate the particles which contain the light-sensitive materials, we mainly focus on light-propelled m-bots with asymmetrical structures.

Tang et al.[85] developed light-propelled microswimmers called Janus TiO_2/Si nanotrees that were fabricated through a partly growth process of TiO_2 on the Si nanowire (**Figure 6**a,b). The Janus TiO_2/Si nanotree can sense and orient itself to the illumination direction of the outer light source via a self-electrophoresis with photoelectrochemical reaction that generates anions and cations at opposite ends of the nanotree and mimics the phototaxis of natural motile algae (Figure 6b,d). Both the positive and the negative phototaxis of the microswimmer can be realized by controlling the zeta potential of the photoanode (Figure 6e).[85] Another example of the self-electrophoresis microrobots is the visible-light-driven bismuth oxyiodide (BiOI) based Janus microspheres powered by photocatalytic reactions reported by Cai et al.[192] The BiOI was selected due to the narrow band gap (17 eV) which makes the materials activated by the visible light. The propulsion of the microrobots can be controlled by adjusting the wavelength and power of the visible light.

Apart from the self-electrophoresis driven m-bots, self-thermophoresis can be also applied for efficient m-bot propulsion. He et al.[46,61] developed polymer multilayer rockets with tubular shape through the template-assisted layer-by-layer assembly and deposition of platinum NPs inside and gold shell outside, followed by the functionalization of tumor-targeted peptide and

antifouling polymer on the gold shell. The NIR illumination can be applied to rapidly trigger the motion of microrobots via self-thermophoresis, and the targeted recognition ability and treatment of the tumor by the photothermal effect using NIR are also demonstrated.

Another type of light-propelled m-bots used light as the switch to promote photocatalysis of the m-bots which can generate gas bubbles to propel the m-bots. Compared with the self-propelled m-bots, external light energy is required for this type of m-bots, the on/off of the motion is switchable, and the speed of the motion is controllable. To date, several types of light-triggered bubbling m-bots have been reported, such as the UV-propelled TiO_2-Au Janus microspheres, and UV-driven TiO_2 microtube. Guan et al.[193] fabricated a light-controlled bubble-propelled tubular TiO_2 microrobot that generated O_2 in the inner tube surface by the photocatalysis of H_2O_2 under UV irradiation. The motion of the microtube can be triggered by UV with a controllable speed by adjusting the intensity of the UV light.

4.4. Self-Propelled m-Bots

Self-propelled m-bots are fuel dependent that convert chemical energy and biochemical energy from the surrounding environment to mechanical energy for autonomous propulsion. Several aspects of the design should be evaluated for the self-propelled m-bot system. Particular attention is to be paid to the structural design of the m-bots and the component of the m-bots that are responsible for the chemical/biochemical reactions. These m-bots are mainly in the form of bimetallic nanowires, tubular microjets, Janus micro-/nanospheres and so on.[194–196] For self-propelled m-bots, motility is commonly achieved from either the decomposition of a fuel by a catalyst or the degradation of the micro/nanorobots in the liquid environment.[194–199] From the literature regarding self-propelled m-bots, a considerable portion of the research focuses on the catalytic decomposition of hydrogen peroxide (H_2O_2).[30,200–211] By integrating proper catalysts onto the m-bots such as Au, Pt, and MnO_2, H_2O_2 can be decomposed to water and oxygen for gas propulsion.[212,213] Although the H_2O_2-fueled m-bots could achieve a much higher propulsion speed than other motors, hydrogen peroxide is regarded as toxic to the organs and tissues in the in vivo environment and shows limitation for biomedical applications.[214]

Enzyme-based m-bots open up a brand-new strategy to promote biocompatible self-propelled m-bots for biomedical applications owing to the good reaction rate and availability of various choices in enzyme/fuel combinations. As one of the special self-propelled m-bots, enzyme-based m-bots commonly use the enzymes as catalysts in lieu of metals like Au, Pt, Ag, and MnO_2, and show high activity and biocompatibility.[215–218] Sanchez et al.[84,219] developed a self-propelled Janus nanorobot based on hollow mesoporous silica nanoparticles which were actuated by biocatalytic reactions based on the three types of enzymes fixed on the surface of the Janus nanoparticles, i.e., catalase, urease, and glucose oxidase. The biocompatible enzyme-based active nanomotors offered exciting potential of using the biological benign fuels for biomedical applications.[219] Some other researchers have also verified that enzymes showed propulsion ability after being anchored onto the artificial micromachines like carbon nanotubes[220] and tubular microrobots.[221,222] Sanchez et al.[223] proposed bubble-free tubular nanojets propelled by an enzyme-triggered biocatalytic reaction that uses urea as the mild fuel. The longitudinal self-actuation and excellent biocompatibility make tubular nanojets promising for bioapplications. Most recently, Mao, Shen, and coworkers[224] developed nitric-oxide-driven nanomotors made of hyperbranched polymide/L-arginine. The NO was generated by the conversion of amino acid L-arginine. The challenge in this field is the combination of the controlled propulsion, biological m-bots, and multiple benign fuels into an uncomplicated design that will enable the actuation and control of the m-bots in a variety of biological media without any change in the m-bots.[225]

4.5. m-Bots Propelled by Other Types of Fields

Apart from the above-mentioned actuation strategies, several other strategies have been also investigated for the propulsion of m-bots. These may require much harsher environment and are not yet suitable for in vivo use. Therefore, here we have lumped them into a single category to provide a brief introduction.

4.5.1. Electric Field-Propelled m-Bots

Just as magnetic field-propelled m-bots must necessarily have integrated magnetic materials in their structures, electric field-propelled m-bots must be conductive/semi-conductive or charged. Electrical actuation has the merit of being contact-free and inexpensive. Remote driving of the m-bots by DC and AC electric fields is emerging as a new wireless controllable and fuel-free actuation method that uses electrophoretic motion, electro-osmotic flow, and electrorotation.[226–236] When a uniform DC electric field is applied, the charged objects migrate toward the electrode having opposite charge due to the Coulomb interactions.[227] When an AC electric field is applied, m-bots can be also actuated in a controlled manner. The AC electric field can be utilized to actuate the objects at the microscale as well due to the dielectrophoretic forces; the torque exerted on the objects by the electric field caused dipole moments and electro-osmotic flow.[230,231] The motion of the microagents actuated by the DC electric field is typically simple and cannot adapt to the complex fluid environment with the roundabout trajectory. In most of the previous works, AC electric fields were applied for m-bot propulsion instead of DC electric fields.[227,228] Electrorotation of magnetic and nonmagnetic nanowires with precisely controlled rotational speed can be also achieved by four phase-shifted AC voltages with a sequential phase shift of 90°.[226,236] Wang et al.[229] developed poly(pyrrole)-cadmium (PPy-Cd) and CdSe–Au–CdSe semiconductor nanowires and actuated them under an external AC electric field by the electro-osmotic flow mechanism to obtain the directional locomotion of nanowires because of the electro-osmotic flow. Unlike electro-osmotic flow-propelled micromachines, the electric field can also trigger asymmetric bubble production via redox reaction at the two faces of the Janus particles. The

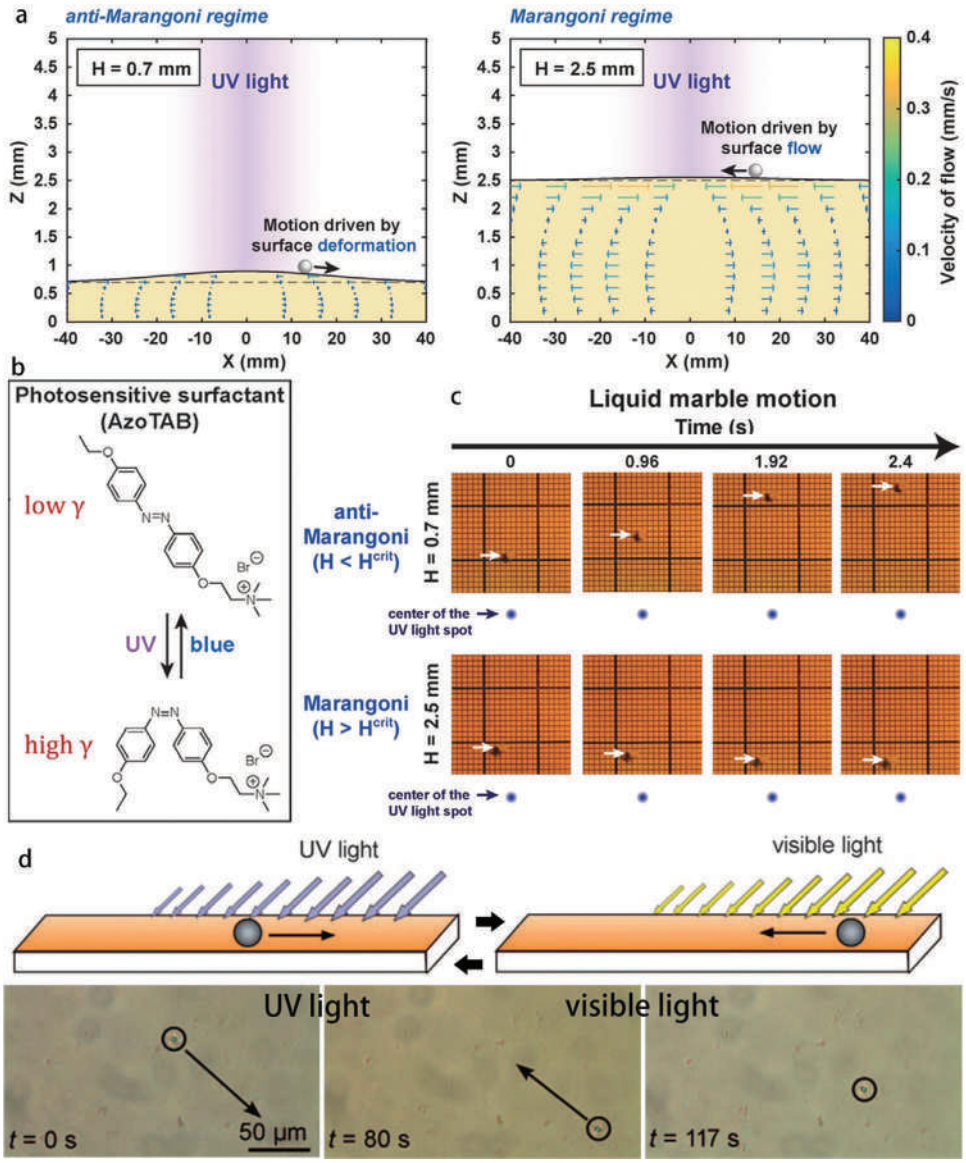

Figure 7. a) Schematic illustration of the propulsion mechanism of anti-Marangoni and Marangoni effects. b) Illustration of the reversible photoisomerization of the photosensitive azobenzene-containing surfactant AzoTAB. c) Time lapse images show the propulsion of a liquid marble (white arrow) by UV irradiation induced Marangoni effects and anti-Marangoni effect. The purple dot denotes the center of the light spot. Reproduced with permission.[242] Copyright 2016, Wiley-VCH. d) Translational motion of a PS solid particle on the surface of a liquid crystal film doped with dl-azomenth. by UV and visible light irradiations. Reproduced with permission.[246] Copyright 2009, Wiley-VCH.

released bubbles can propel the micromotors continuously with both translational and rotational motions.

However, the bioapplications of electric field-propelled m-bots may be limited due to their short locomotion range that is resulted from the rapid attenuation of the electric field with the distance, and the electric field may be incompatible[232] with highly ionic media such as the interstitial fluid and blood.

4.5.2. Marangoni Effect-Propelled m-Bots

Marangoni effect is a liquid flow motion that occurs on the interface between two different phases (e.g., liquid and air), caused by the gradient of the interfacial tension. In most cases, the Marangoni effect is utilized to actuate the motors and droplets of the visible scale; however, the study is still instructive for the design and fabrication of the next-generation m-bots, especially for applications at the surface and interface of solid, liquid, and air. The Marangoni effect-propulsion occurs chiefly at the liquid/air or solid/liquid interfaces.[237–240] Baigl et al.[241] developed a technique that can actuate the oil droplets on the water surface for controlled liquid transportation and high precision droplet coalescence. The authors dissolved *cis*-AzoTAB into the solution as this molecule could change configuration under light irradiation due to photoisomerization (**Figure 7**a,b), resulting in a change in the surface tension

of the water solution. The local change in the surface tension would cause the liquid to flow toward the low liquid-tension region (Figure 7a). Therefore, the droplet can be transported on demand using the Marangoni effect. Apart from the actuation of the liquid droplets, the actuation of the solid objects and even the liquid marbles composed of both liquid and solid phases, can be propelled using the Marangoni flow and anti-Marangoni flow (Figure 7c), as reported by Baigl et al..[242] Kurihara et al.[246] showed the translational motion of the micro-objects (i.e., PS microspheres) on the surface of a liquid-crystalline thin film caused by the Marangoni effect. With the irradiation of the surface by UV and visible light, the PS microsphere was actuated and the direction of motion was dependent on the direction and position of the irradiation (Figure 7d). Besides the actuation of the single microrobots, the collective motion of many tiny microrobots could be also archived by the Marangoni effect. Zhao et al.[247] reported a Janus catalytic micromotor that could generate the O_2 bubbles in an H_2O_2 environment. As the bubbles coalesced and grew, the micromotors moved collectively toward the bubble and eventually formed an aggregation around the perimeter of the bubble because of the evaporation-induced Marangoni flow around the bubble. Several other researchers have also demonstrated the existence of Marangoni flow-induced propulsion of tiny agents, as described in the works by Shi et al.[243,244] and Sun et al..[245] Accordingly, the actuation of the objects on the liquid surface is independent on the objects but highly dependent on the liquid surface. Marangoni and anti-Marangoni propulsion are versatile strategies for the actuation of such tiny machines.

4.6. Hybrid m-Bots

4.6.1. Multiple Energy-Propelled m-Bots

Hybrid m-bots use two or more energy sources for their navigation and control, and thus, extend the scope of manipulation of the m-bots in complicated and changeable environments.[248–253] Wang et al.[253] fabricated a catalytically/magnetically powered adaptive nanowire swimmer composed of a flexible multisegmented Pt–Au–Agflex–Ni nanowire (**Figure 8**a,b), with the Pt–Au and Au–Agflex–Ni portions responsible for catalytic and magnetic actuation, respectively. Hybrid m-bots powered by two energy sources can switch their mode of motion from catalytic to magnetic and thus, respond better to the changes in the surrounding environment (Figure 8c). Mallouk et al.[112] presented a synthetic bimetallic micromotor, which can be actuated with both the positive and negative rheotaxis property by the hybrid driving force of the chemical fuel and acoustic field (Figure 8d). Other m-bots actuated with two energy sources, such as UV and NH_3, have also been reported.[254]

In addition to the self-propelled and external field-steered hybrid m-bots, the motion and direction of the m-bots can be controlled with the external fields, avoiding the use of chemical fuels.[255] Wang et al.[249] developed a magnetic/acoustic hybrid fuel-free nanorobot composed of a segment of Au nanorod and Ni-coated Pd helical structure (Figure 8e), which can be actuated by either a magnetic or an ultrasonic field in an on-demand manner (Figure 8f,g). More importantly, this work demonstrated that the hybrid power actuation of the m-bots can realize the reversible swarming states and collective behaviors, which is hardly possible by the single propulsion mode.

4.6.2. Hybrid of Natural Microorganism and the Artificial Microdevices

Apart from the artificial m-bots, hybrid m-bots that are a combination of natural microorganisms and artificial microdevices have also been developed.[256–263] Sanchez et al.[256] developed sperm-propelled biohybrid microrobots comprising of a motile sperm cell and a magnetic microtube (**Figure 9**a). The micro-bio-robots are self-propelled by the sperm cell and steered with an external magnetic field (Figure 9c). No toxic fuel is used in the system unlike other chemically fueled m-bots. Another sperm-propelled, helical micro-bio-robot actuated and steered using a magnetic field was fabricated by 3D direct laser writing and subsequent Ni coating by the same research group.[257] The sperm-propelled micro-bio-robot could serve as an assistor to deliver healthy but immotile sperm to an egg, which may aid in infertility treatments (Figure 9b,d). Further, they[259] found that these biohybrid microswimmers may also be used as targeted drug delivery carriers. The motile sperm cell in this biohybrid microswimmer not only served the purpose of providing propulsion, but also acted as the carrier. A 3D-printed magnetic tubular microstructure was used for precisely steering the sperm and the hitting-induced release of the sperm cell for drug release, as demonstrated in Figure 9e. Wang et al.[258] developed an intelligent self-guided biomotor with chemotactic motile behavior, which is prepared by the functionalization of various nanoscale payloads such as quantum dots, doxorubicin hydrochloride drug-coated iron-oxide NPs, and fluorescein isothiocyanate-modified Pt nanoparticles with the sperm micromotors. These micromotors can be applied for the targeted drug delivery carriers with the transportation of the cargo guided by the intrinsic chemotaxis of the sperm micromotors. Besides, the bacteria biohybrid microswimmers[264–267] were also proposed by Sitti and Sanchez et al.[264] to propel the microtubes with the motile *E. coli* in biological media prepared via adhesive bonding of *E. coli* with the inner side of a microtube with a PDA layer. To further increase the loading-carrying efficiency, biocompatibility, and biodegradability, they reported another bacteria-propelled biohybrid microswimmer that used red blood cells as autologous cargo carriers for active and guided drug delivery.[268] The red blood cells loaded with drugs and superparamagnetic iron oxide NPs were fixed on the motile bacteria by chemical bonding, and the microswimmers were steered using an external magnetic field. After the treatment, the bacteria can be killed using the on-demand light-activated hyperthermia process for the controlling of the bacteria population to a safe range in the organisms.

4.7. Collective Behavior of m-Bots

The actuation and control of single m-bots using different energy sources have been extensively studied. However, in

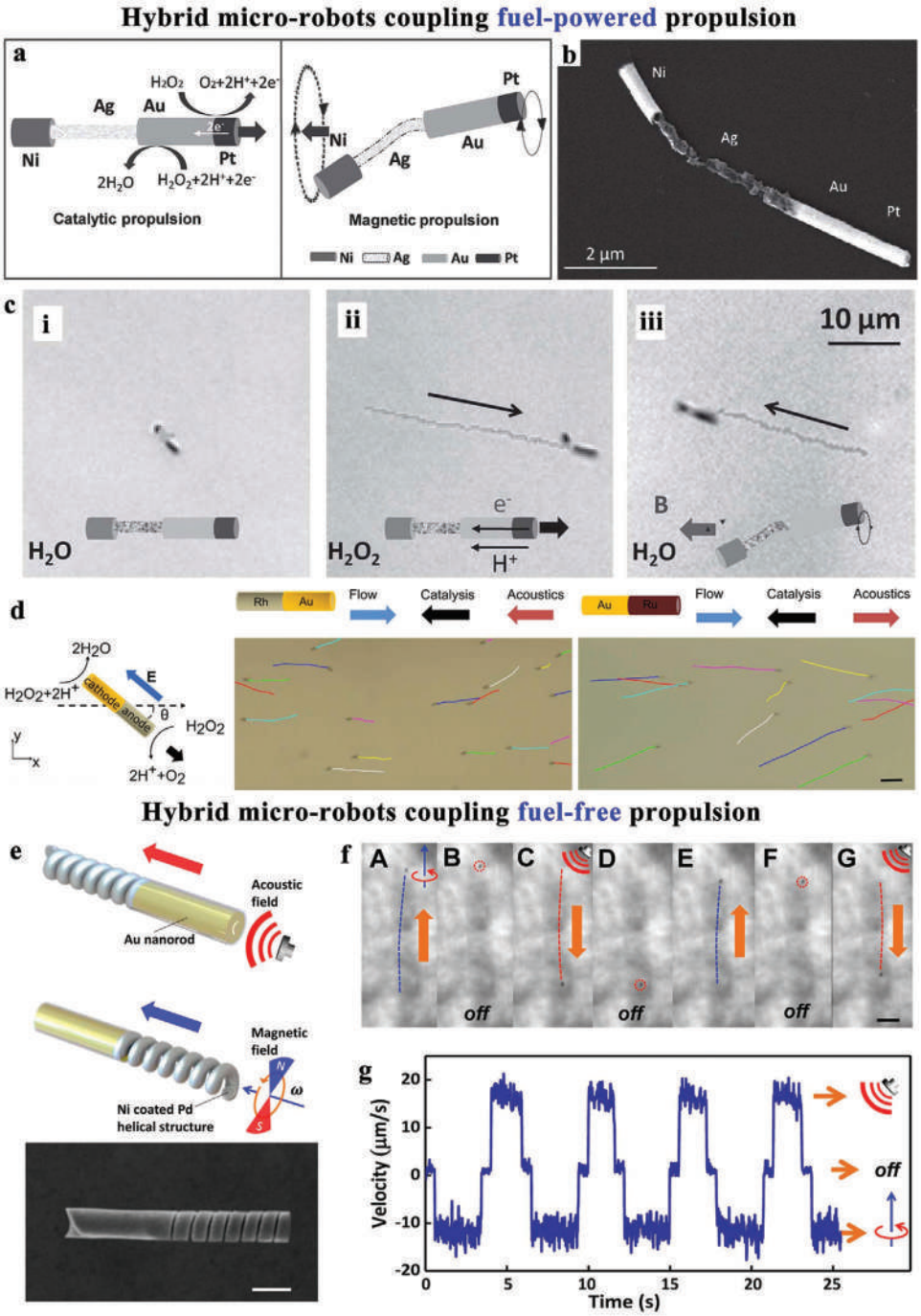

Figure 8. a) Schematic illustration of the catalytic and magnetic actuations of the hybrid Pt–Au–Agflex–Ni nanowire. b) SEM image shows the flexible Pt–Au–Agflex–Ni nanowire motor. c) Motion of the hybrid nanowire motors i) without fuel and magnetic field, ii) with fuel, and iii) with magnetic field. Reproduced with permission.[253] Copyright 2011, Wiley-VCH. d) Schematic illustration of the design of the magnetoacoustic hybrid microrobot and the two types of actuation modes under acoustic and magnetic fields, respectively. Reproduced with permission.[112] Copyright 2017, American Chemical Society. e) SEM image of a magnetoacoustic hybrid microrobot. Scale bar is 500 nm. The cycling motion processes shows the f) tracking lines and g) speed changes between the magnetic propulsion, acoustic propulsion and without any fields. Reproduced with permission.[249] Copyright 2015, American Chemical Society.

practical applications, the single m-bot may be subject to its limited capacity and unable to realize the expected objectives. The use of multiagents may become indispensable for the completion of the designated tasks. The locomotion and control of the multiagents have two modes, i.e., independent motion and dependent motion. In the independent motion mode of the multiagents, the microagents are all independent without any restriction of origin from their neighbors. Their actuation is, therefore, similar to that of the single m-bots. Inspired by the natural collective behavior indicated in **Figure 10**a,b,

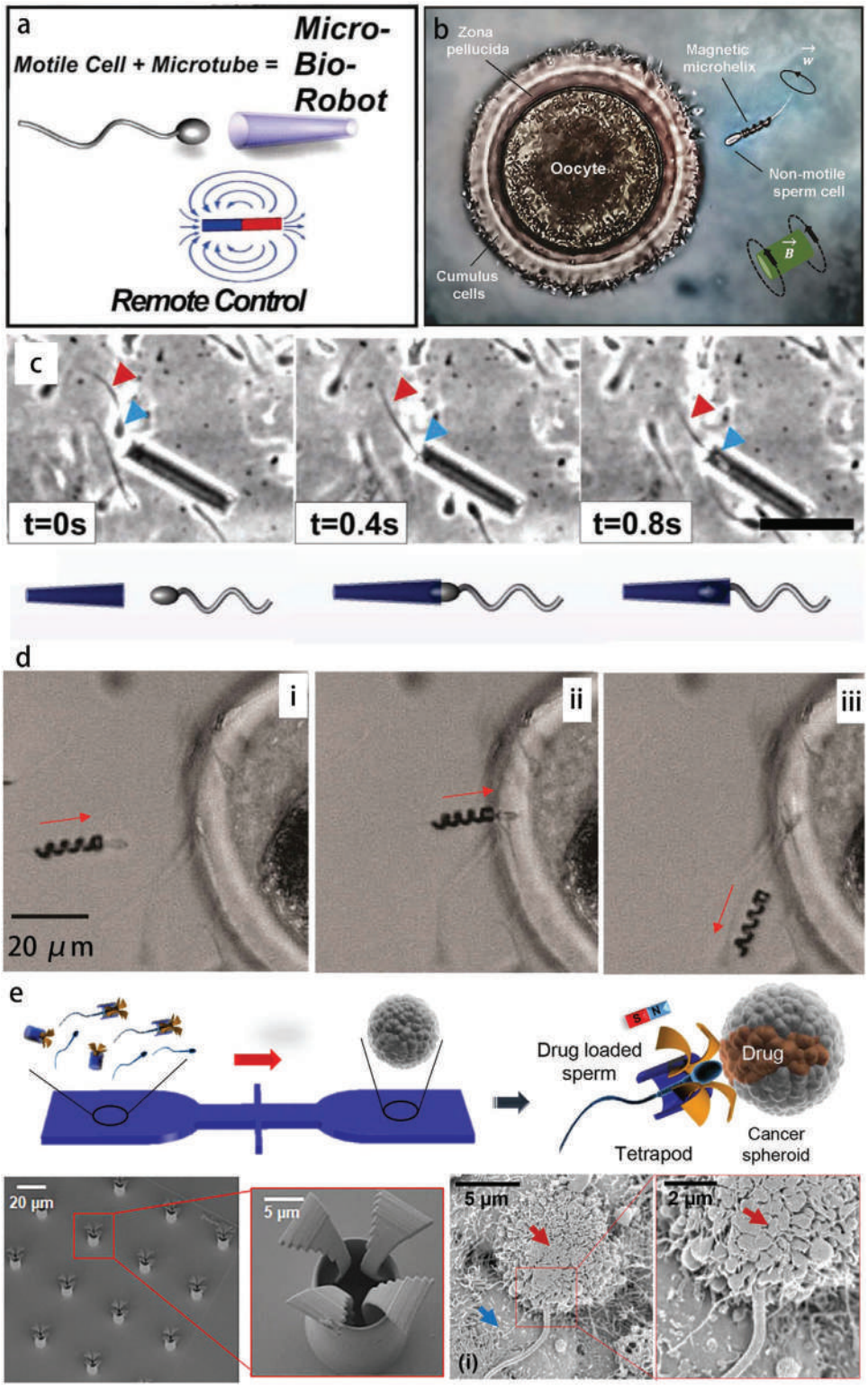

Figure 9. a) Schematic of a micro-bio-robot comprised of a motile sperm cell trapped inside a microtube. Reproduced with permission.[256] Copyright 2013, Wiley-VCH. b) Capture process of an immotile sperm by a magnetic helical microrobot controlled with external magnetic field to the oocyte for fertilization. Reproduced with permission.[257] Copyright 2016, American Chemical Society. c) Coupling process shows a bull spermatozoon swarm trapped inside a microtube. Reproduced with permission.[256] Copyright 2013, Wiley-VCH. d) Successive images show the i) sperm cell coupling, ii) transportation, iii) approaching the oocyte membrane, and iv) releasing processes. Reproduced with permission.[257] Copyright 2016, American Chemical Society. e) Schematic of the transport and delivery of drug-loaded sperm by the hybrid microrobot to the tumor cells. SEM image of the microrobots. SEM images show the sperm–HeLa cell fusion by the hit process. Reproduced with permission.[259] Copyright 2018, American Chemical Society.

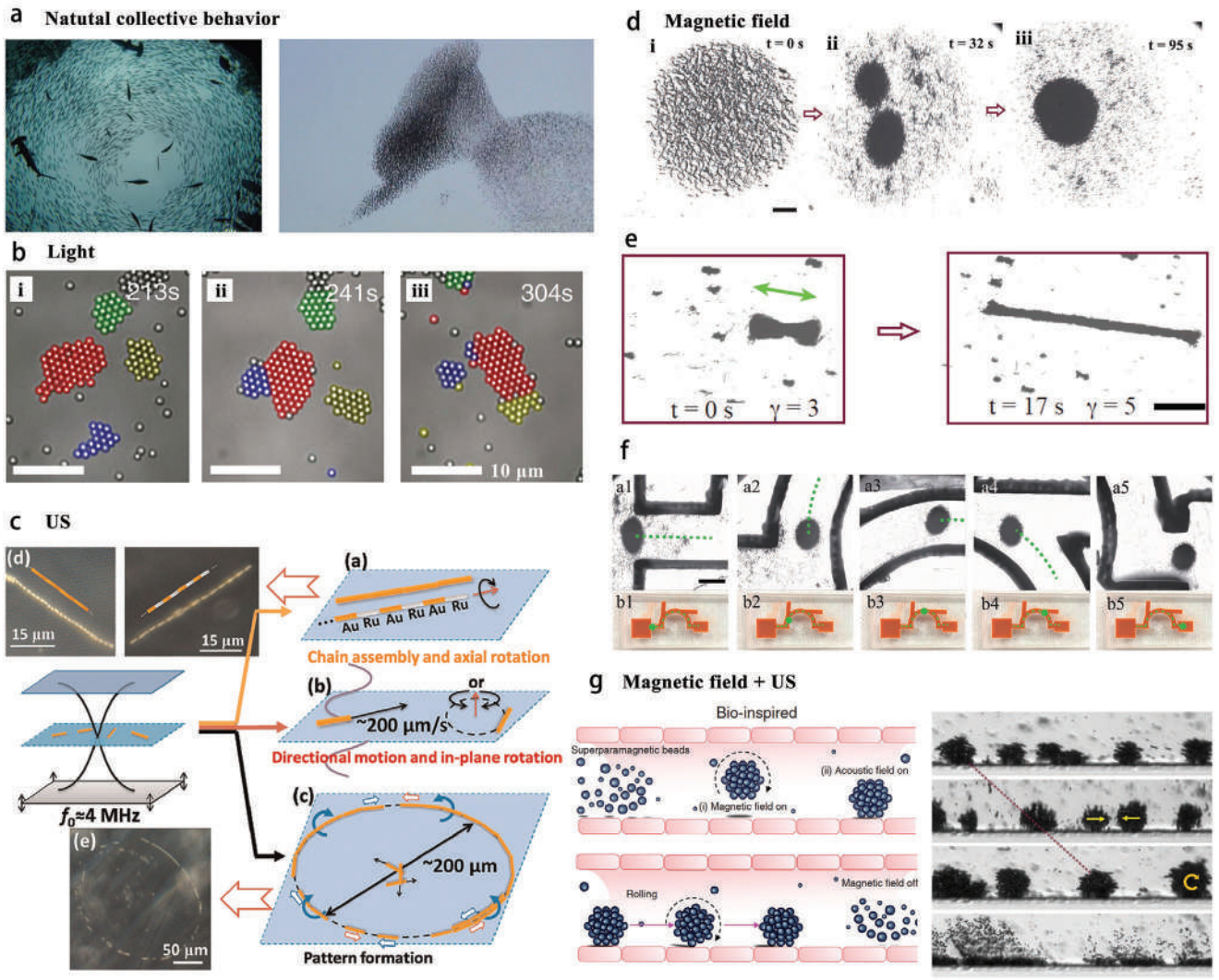

Figure 10. a) Collective behavior of fish and starling birds. Left image: Reproduced under the terms of a Creative Commons Attribution 4.0 International License.[289a] Copyright 2016, The Authors, published by Springer Nature. Right image: Reproduced under the terms of a Creative Commons Attribution 4.0 International License.[289b] Copyright 2019, The Authors, published by Springer Nature. b) Light-propelled collective motion. The false color images show the time dynamic evolution of the collective behavior of Janus particles belonging to diverse clusters under light radiation. Reproduced with permission.[276] Copyright 2013, AAAS. c) US-propelled collective behavior. Schematic of the different motions of metal microrods under acoustic field and dark field views of the typical chain structures and ring patterns formed by the microrods. Reproduced with permission.[169] Copyright 2012, American Chemical Society. d–f) Magnetic field-propelled collective behavior. d) Reconfigurable swarm of magnetic particles with controlled particles swelling and shrinking. e) Reversible elongation of ribbon-like swarming pattern. Reproduced with permission.[287] Copyright 2018, The Authors, published by Springer Nature. Scale bar is 600 μm. f) Locomotion of magnetic particles in channel through swarming mode under magnetic field. Reproduced with permission.[284a] Copyright 2018, SAGE. g) Hybrid energy input-propelled collective motion. Schematic and optical images show the collective motion mode of clusters of superparamagnetic particles rolling along the wall of a channel under the magnetic field and acoustic field. The aggregation of the particles is caused by the dipole–dipole interaction in the magnetic field and the migration of the particle clusters toward the wall is due to the radiation force in the acoustic field. Reproduced under the terms of a Creative Commons Attribution 4.0 International License.[290] Copyright 2017, The Authors, published by Springer Nature.

i.e., schooling of fish (Figure 10a) and swarming of starling birds (Figure 10a), the investigation of the collective behavior and swarming motion of the m-bots have also been put on the agenda.[269,270] The collective behavior is strongly distance dependent. The short-range forces with either attraction or repulsion such as van der Waals attraction, electrostatic interaction, steric repulsion all work during the swarming. Each unit generates a flow field that is experienced by the surrounding units and induces aligning interactions.[36,271–273] The micro-/nanoagents inside the collective motion are all dependent and communicate with their neighbors, even with the inert micro-/nanoparticles inside the efficient region, in the form of either attraction or repulsion. While the concentration of the m-bots is low, more than one swarm pattern may be generated because the short-range interactions between the active particles may not strong enough to merge all the particles. The collective motion and swarm formation of the m-bots allow the coordinated locomotion of dissimilar objects, making it easier

Table 2. Comparison of and biomedical application scope of single m-bot, multiple m-bots, and swarming m-bots.

	Pros	Cons	Biomedical application scope
Single m-bot	1) High precision control 2) Applicable for 2D motion and 3D motion	1) Limited imaging contrast 2) Significant interference by Brownian motion for tiny robot	1) Sensing 2) Diagnosis 3) Guided nerve cell growth direction 4) Surgery
Independent actuation of multiple m-bots	1) Large-area therapeutic effect; 2) Relatively high motion speed 3) Effective motion mode for unbranched vessel	1) Potential loss during locomotion in curved and branched channels 2) Limited imaging contrast due to the dispersion	1) Drug delivery toward broad region 2) Gastrointestinal drug delivery 3) Would healing
Swarming of multiple m-bots	1) Reconfigurable and self-adaptable motion through narrow channels and small cavities with low agents' loss 2) High imaging contrast due to the aggregation effect and dynamic motion 3) High precision control toward the target	1) Relatively low motion speed 2) Motion along an interface 3) Hard to move on a stepped surface	1) Drug delivery toward specific site 2) Targeted thrombolysis in 3D branched vessel

to transport and deliver cargoes to the designated regions. **Table 2** summarized the pros and cons of the single m-bot, multiple m-bots, and swarming m-bots toward their biomedical applications.

Light induced collective behavior has been extensively studied.[274–276] Sen et al.[274] reported the light-driven collective behavior of the AgCl microparticles in aqueous solution under UV radiation. The mechanism of the collective motion was attributed to diffusiophoresis. The UV radiation caused the dissolution of AgCl to generate the protons and chloride ions.[275] As a result, an electric field was generated in the solution that acted both on the particles and on any nearby wall double layer as the diffusivity of protons is much higher than that of the chloride ions. The electrolyte gradient creates a pressure difference, which induces a flow of liquid from the region with high electrolyte concentration to the region with lower electrolyte concentration, describing the collective behavior. The study also offered a nonbiological model for the investigation of the cell signaling and collective behavior. Similarly, the 2D collective behavior of the Janus particles composed of polymer microspheres with an antiferromagnetic hematite cube on one side is also demonstrated with the activation by light by Palacci et al.,[276] termed as living crystals. The osmotically driven motion and steric hindrances caused the formation of dynamic living crystals. A thermally induced collective is also reported by Buttinoni et al.,[277] who presented an experimental study of a colloid suspension of Janus particles that are self-propelled by the heating (532 nm) of carbon-coated hemispheres in a mixture of water and lutidine. In this system, a number of small dynamical clusters appear at low densities and one big cluster appears at high densities, which is rationalized in terms of a dynamical instability because of the self-trapping. Other photocatalytic and photosensitive m-bots are also developed, such as SiO_2–TiO_2 micromotors,[278] Fe_2O_3 micromotors,[276,279] and TiO_2-Pt micromotors.[247,280–282] For instance, Sen et al.[278] developed SiO_2–TiO_2 microparticles that can be reversibly assembled and disassembled under UV illumination. The authors suggested that the TiO_2 generated O_2^-, $\cdot OH$, and H^+ under the UV light and the collective behavior of the particles may attributed to the osmotic propulsion or diffusiophoresis.

The magnetic field-controlled swarming motion was recently reported.[271,283–286] The magnetite nanoparticles fabricated from the solvothermal method can be assembled to a planar dynamic cluster and disassembled to dispersed nanoparticles after the application of the rotational and dynamic magnetic fields, respectively. The final particle concentration can be increased to ≈500% of the initial concentration for the assembly process and decreased to ≈20% of the initial concentration for the disassembly process. The assembled vortex swarm pattern can also realize the reversible merging and splitting process as shown in Figure 10.[283,284] The swarming motion can be also well performed on uneven surfaces.[283b] The entity of swarm pattern can be actuated to pass through the curved and branched channels to the designated site with high precision with negligible particle loss less than 10%, which is much more efficient than that of the conventional tumbling motion. Furthermore, they also extended the magnetic swarm behavior from 2D to 3D by introducing the dynamic bubbles for the purpose of crosslinking and vertical axis stacking of the nanomotors.[271] Compared with the 2D swarming motions without bubbles, the integral rotation and translation was improved due to the dynamic dewetting and increased slip length caused by the continuously ejected tiny bubbles.

Apart from the isotropic swarming clusters, anisotropic swarming clusters can be also formed. Zhang et al.[287] developed a reconfigurable ribbon-like swarming pattern with dynamic-equilibrium structure in fluid under a programmed oscillating magnetic field. The reversible elongation with high aspect ratio and controlled splitting and merging of subswarms are realized. The authors also demonstrated that the ribbon-like dynamic swarming pattern can pass through a confined channel toward multiple targets with high access rates and perform noncontact micromanipulation in the fluid. Apart from the planar swarming pattern, they further extended the swarming behavior into 3D form by the introduction of NIR light.[288a] To promote the biomedical applications of the swarming m-bots, they have archived and systematically studied

Table 3. Summary and comparison of bioimaging modalities for tracking the m-bots.

	Advantages	Limitation	Imaging probe
Fluorescent imaging	Excellent planar resolution (≈100 nm); high sensitivity	Shallow imaging depth (≈2 mm); poor biocompatibility and biodegradability	M-bots decorated with fluorescent dyes and nanoparticles
MRI	Nonionizing radiation; high soft tissue contrast	High cost; long imaging time	Magnetic m-bots
US imaging	Noninvasive; portable; low-cost; safe; fast	Limited penetration/sensitivity; low signal noise ratio; low resolution; interfered by bone	M-bots generating microbubbles
Radionuclide imaging	High sensitivity; fast imaging time	Low spatial resolution (≈1–2 mm); ionizing radiation	Radioactive tracer functionalized m-bots
PACT	High resolution; fast imaging time	Limited penetration depth	M-bots with high absorption of NIR

the active generation and magnetic actuation of microrobotic swarms in various biofluids under the real-time tracking by clinical imaging tools such as US imaging.[288b]

The input of hybrid energies into a cluster of particles can cause a more diversified motion behavior. As showed in Figure 10g, Nelson et al.[290] combined the magnetic field with the acoustic field and applied to the particles system with boundaries to mimic the vasculature environment. They found that the superparamagnetic particles that assembled to form multiple clusters inside the vasculature exhibited rolling motion along the wall of the vessel. From the combination of the multiple external energies, this new motion behavior may overcome the limitations encountered by single-energy actuation and shows its potential in targeted therapeutics. Li et al.[291] proposed another hybrid energy-driven collective behavior of nanomotors. The light and ultrasound fields were applied to control the aggregation and separation of the nanomotors with ease.

The motion of the swarming m-bots can be easily impacted by the fluidic environment, such as viscosity, mobility of the liquid, boundary effect, and other impurities. Further investigations about this field may require the development of highly responsive m-bots with rational structural and componential design for overcoming the potential motion inhibition in real biological systems.

5. Localization of m-Bots

Localization of m-bots is essential for their practical applications. The location of the m-bots and the target inside the practical application system is crucial for the next-step navigation of the m-bots. For in vitro applications such as sensing, the m-bots are generally localized readily with an optical microscope and as a feedback, the location information also provides the manipulator with the next step to control the m-bots. If the m-bots are applied for in vivo applications such as tumor therapy and thrombus ablation, optical microscopy is unsuitable, and other imaging techniques should be explored to visualize the m-bots across the tissue. Newer imaging techniques including fluorescent imaging (FI), magnetic resonance imaging (MRI), ultrasonic (US) imaging, computed tomography (CT), positron emission tomography (PET), single-photon emission computed tomography (SPECT), and photoacoustic computed imaging (PACT) have been tried for m-bot localization (**Table 3**). The synergy of imaging and motion control makes it possible for targeted delivery/therapy in a destined location with vision-based control. Moreover, the additional motion of the m-bots may also enhance the imaging contrast because of the dynamic behavior in contrast with the static m-bots. Enormous advances in biomedical imaging[39,40] have made the visualization of movable micro- and nanorobots a novel tool for targeting specific locations with high precision and accomplishing certain medical tasks in a minimally invasive fashion.

5.1. Fluorescent Imaging

Fluorescent imaging is an efficient imaging technique that is widely used both in vitro and in vivo. Compared with other imaging techniques, fluorescent imaging has the advantages that it applies only nonionizing radiation to the tissues and that the probe materials are relatively inexpensive. Various fluorescent probes like semiconductor quantum dots (QDs), fluorescent metal organic frameworks and organic dyes have been developed to label the cells at specific areas and peculiar biomolecules.[292–294] Fluorescent imaging has also been miniaturized and integrated in catheterization and endoscopy systems for enabling minimally invasive inspection of deep tissue.[295] Owing to these advantages of fluorescent imaging, the integration of the actuation and control of m-bots with fluorescent imaging simplifies the localization and next-step actuation of the m-bots and broadens the bioapplication to active bioimaging and diagnosis. To date, several fluorescent m-bots have been reported to achieve the fluorescence-based tracking of m-bots with precisely targeted imaging under the visible locomotion using external fields. Based on the raw materials used for imaging, the fluorescent m-bots can be classified into autofluorescence- material based microrobots, dye-based microrobots, and quantum dot-based microrobots.

In nature, part of the biological organisms possesses intrinsic fluorescence properties in the range from UV-visible light to the near-IR light.[296] The autofluorescence of these organisms originates from complicated molecules that serve as endogenous fluorophores. If autofluorescent organisms are used as the template to prepare m-bots, the as-prepared devices may inherit the fluorescent property and facilitate the tracking of the devices even in real-time mode. The SU-8 photoresist is a fluorescent material that shows its emission near the blue and green light region. Steager et al.[119] fabricated autofluorescent and biocompatible magnetic microrobots by printing using a mixture of the photoresist and iron oxide NPs. The autofluorescent microrobots could be actuated with an external magnetic

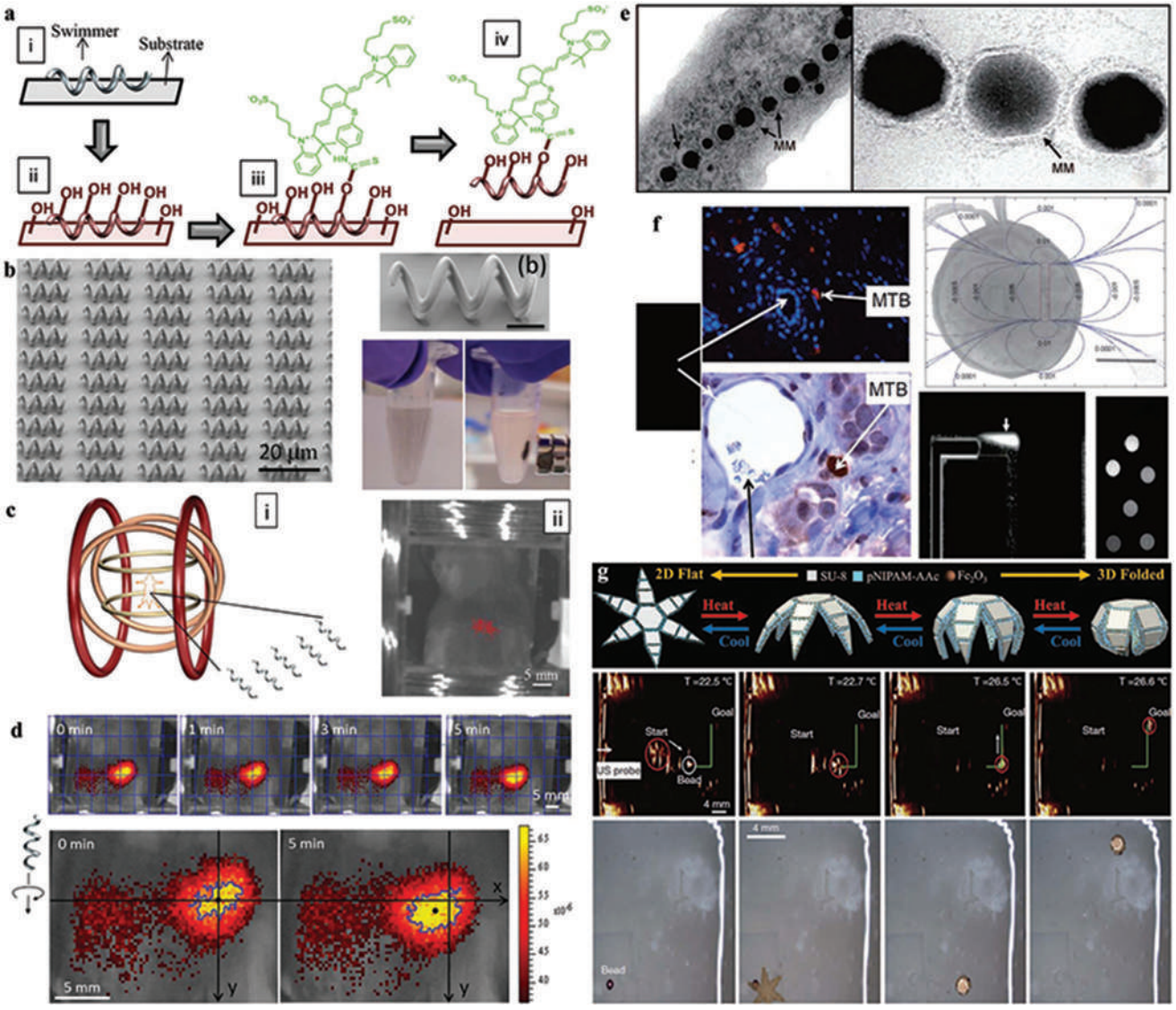

Figure 11. a) Schematic of the surface functionalization process of the artificial bacterial flagellum microswimmers with NIR-797 dyes. b) SEM images show the integral and enlarged views of the artificial bacterial flagellum microswimmers and the optical image shows the magnetic property of the microswimmers. c) Schematic of the in vivo experiment conducted under the magnetic coil system, and the image of an anesthetized mouse inside the coils. The red spot is the fluorescent signal generated by the injected artificial bacterial flagellum microswimmers. d) Successive images show the in vivo tracking of the motion of artificial bacterial flagellum microswimmers. a–d) Reproduced with permission.[44] Copyright 2015, Wiley-VCH. e) TEM images show the magnetotactic bacteria and the magnetosomes inside the bacteria. Reproduced with permission.[304] Copyright 2008, American Chemical Society. f) The left microscope images show the bacteria after targeting to the interstitial area of tumor. The SEM image at the right side is a magnetotactic bacteria with a chain of two flagella with the superposed distortion of the spatial magnetic field distribution. The MRI image shows the magnetotactic bacteria swarm motion along the predesigned trajectory in microchannels. The MRI contrast of the magnetotactic bacteria with various concentrations. Reproduced with permission.[305] Copyright 2009, SAGE. g) The upper image illustrated the folding and unfolding processes of the microgripper controlled by temperature variation. The middle and lower images show the successive snapshots of the gripper during manipulation and transportation of a beads captured by US and microscope imaging techniques, respectively. Reproduced with permission.[319] Copyright 2017, IEEE.

field and tracked in a dark field, demonstrating the potential of fluorescence-based real-time tracking of the microswimmers. Another example used natural autofluorescent organisms as the template. Zhang et al.[64] developed a biohybrid helical magnetic microrobot by using *Spirulina* as the template to coat iron oxide NPs via a dip-coating procedure. The resultant biohybrid helical magnetic microrobots show autofluorescence that could emit red light under the green light illumination. The authors demonstrated in vivo the real-time tracking and diagnostic sensing under the guidance of an external magnetic field integrated with a fluorescent microscope, in the subcutaneous tissue and intraperitoneal cavity of nude mice.

Apart from autofluorescence, organic dyes are also widely used as contrast agents for the imaging of biomolecules, cells, and organisms due to their easy availability and small molecule size, which lower the risk of possible steric hindrance that may interfere with biomolecule function.[297] Due to its ability for easy conjugation that aids anchoring, organic dyes are applied with m-bots for imaging. Servant et al.[44] proposed an artificial bacterial flagellum microswimmer modified with near-infrared probes

NIR-797 (**Figure 11**a,b). While the artificial bacterial flagellum microswimmers were injected into the intraperitoneal cavity of a 4-week-old Balb/C mouse, an obvious fluorescent signal was detected in the abdominal cavity that was consistent with the location of the artificial bacterial flagellum microswimmers (Figure 11c). When the microswimmers were actuated toward the lower part of the mouse body, the red and yellow signals moved simultaneously, which was captured by the fluorescent microscope in real-time (Figure 11d). The results demonstrated the effectiveness of in vivo targeted imaging under the guidance of an external magnetic field in realizing the whole-body fluorescence imaging with the usage of long-wavelength dyes.

Quantum dots, which are ultrasmall size nanomaterials in the range of 1–10 nm, have been used for imaging in the form of pure QDs and complexes that integrate QDs with different nanomaterials/nanoparticles including m-bots. QDs exhibit remarkable optical properties such as high quantum yields, broad absorption range, narrow and size-adjustable emission, and good resistance to photobleaching.[298,299] Jurado-Sánchez et al.[56] developed for the first time a kind of microtube fixed with CdTe QDs via a layer-by-layer self-assembly process which coupled the optical properties of QDs and autonomous motion of the microrobots. Moreover, the change in fluorescence was monitored for evaluating the capability of detection of the toxic organic and inorganic agents. However, QDs generally exhibit severe cytotoxicity and the functionalization process of QDs on m-bots may easily cause the quenching of the fluorescence, which limit the in vivo bioapplication of the QD-based m-bots. To overcome the cytotoxicity, carbon quantum dots, which are QDs with good optical properties and biocompatibility, have been developed for bioimaging applications.[300] Jurado-Sánchez et al.[301] loaded graphene quantum dots into the Janus microrobots to obtain the fluorescence microscope trackable micromachines under a dark field, which could be applied for the detection of bacteria endotoxins.

As demonstrated by the above-mentioned three types of fluorescent m-bots, the fluorescence imaging-based m-bots have the advantages of high sensitivity, high selectivity, and diverse features. But commonly, they possess the limitation of the low penetration of biological tissues that renders them unsuitable for deep-tissue imaging. Different fluorescent m-bots have their own limitations. In autofluorescence-material based microrobots, the autofluorescence phenomenon is ubiquitous in biological systems that may interfere with microrobot signals and thus restrict the in vivo applications of the microrobots. Moreover, the autofluorescence material-based microrobots have a nontunable emission range, which is commonly blue or green emission. The short wavelength of the emitted light makes the microrobots unsuitable for application in deep tissue imaging. As for the dye-based microrobots, most of the dyes are toxic to the biological systems and may cause side effects. Moreover, dyes like fluorescein, cyanine, and rhodamine, have limited application in long-term imaging and multicolor detection.[302] For QD-based microrobots, the limitation include the complex functionalization process of m-bots with QDs, and the cytotoxicity of QDs for in vivo applications. Future research regarding these m-bots may focus on long-wavelength fluorescent probes for deep-tissue imaging and development of biocompatible/biodegradable fluorescent m-bots for in vivo applications.

5.2. MRI

For m-bots guided by the magnetic field, MRI is a very efficient tool to localize the magnetic m-bots both in vitro and in vivo with high contrast.[303] Imaging of m-bots with MRI possesses several advantages over other imaging techniques, especially CT. First, MRI does not expose biological systems to ionizing radiation. Second, MRI can achieve 3D section imaging without reconstruction. Third, MRI also gives better imaging contrast for soft tissues such as bladder when compared with other techniques, and higher imaging resolution than CT. Basically, two types of imaging modes are applied for MRI, namely, d longitudinal relaxation (T1-recovery) and transverse relaxation (T2-recovery). The T1 contrast agents generate bright contrast and T2 contrast agents generate dark contrast, respectively. Commonly, superparamagnetic nanoparticles which are widely used for the construction of magnetic m-bots is applied as T2 contrast agents. The contrast can be enhanced with the increase in the concentration of the contrast agents and the magnitude of magnetization (applied external magnetic field). As a type of external field actuated m-bots, magnetic m-bots can be powered either by the magnetic field itself or powered by other means but steered by the magnetic field as illustrated in section on actuation. To date, both natural and artificial magnetic m-bots have been reported for visualization with MRI. Magnetotactic bacteria can align their body with an external magnetic field. The chain of magnetosomes inside the body of magnetotactic bacteria, as shown in Figure 11e, causes them to arrange their body in an orderly fashion along the external magnetic field.[304] Martel et al.[305–308] systematically studied the motion behavior of the magnetotactic bacteria and found that they navigate through the microvasculature for directed chemotherapy under MRI. The authors established a medical interventional system that used MRI as an imaging technique for feeding back locational information to the controller, which takes responsibility for the real-time navigation of the magnetotactic bacteria and the artificial m-bots along preplanned paths in blood vessels to conduct targeted delivery tasks (Figure 11f). They also showed that the MRI platform can be applied for the tracking of polar magnetotactic bacterial robots to load cargo.[309,310] They suggested that steerable magnetotactic bacteria may be applied for the treatment of cancer and thrombosis by using MRI as an imaging technique. Apart from natural magnetotactic bacteria, the artificial magnetic m-bots were also visualized under MRI with magnetic propulsion.[64,311] Zhang et al.[64] prepared biohybrid magnetite helical microrobots that can not only be localized by the fluorescence imaging, but also inspected with MRI in vivo. The dual mode imaging of biohybrid microrobots broadened the application range of the specific environment for in vivo imaging-guided therapy.

5.3. US Imaging

US imaging is an imaging technique for the tracking of the micro-nanorobots. Compared with other imaging techniques, US imaging has the advantages of real-time control of m-bots with instantaneous image feedback, no adverse health effects, low cost of diagnosis, no requirement of contrast agents, and

high imaging depth of ≈10 cm for human tissue. In the case of other clinical imaging techniques, such as CT and MRI, contrast agents in the micromolar to millimolar range may be required for the detection of the target position, which may cause the potential side effects to the biological system. These advantages of US imaging have attracted extensive interest for its potential in tracking m-bots.

Sanchez et al.[312] reported self-propelled microjets controlled by an ultrasound system in which the navigation of the microjets is affected by the continuous ejection of O_2 bubbles originating from a catalytic reaction on the inner platinum surface in the presence of H_2O_2. The direction of motion of the microjets was determined by the magnetic field and the motion paths of the microjets were recorded by tracing the position of the microbubbles generated by the microjets via microscope and US imaging. The trajectories of the microjet recorded by these two imaging modes all indicate that the microjet can locomote in a relatively precise manner following the preprogramed closed-loop trajectories. By comparison, the location accuracy of US imaging feedback is somewhat lower than that of microscopic imaging.

Apart from the self-propelled microrobots, which are generally tracked by the indirect imaging of the microbubbles,[312,313] some other studies demonstrated the US imaging of microrobots actuated by the magnetic field without any bubbles, such as the works conducted by Khalil et al.,[314] Peng et al.,[315] and Zhang et al.[316–318] Moreover, Scheggi et al.[319] prepared soft miniaturized untethered grippers which respond to the temperature to perform the grasping and releasing with the 2D flat shape and 3D folded shape, respectively. The miniaturized grippers were fabricated from materials that contained 3% Fe_2O_3 to endow the grippers with magnetic properties. The gripper was navigated with US imaging, providing the feedback along both the step path and sinusoidal path (Figure 11g). The soft miniaturized gripper was proved to possess the ability to grasp the bead (500 μm) and transport it along the designed path to the destination.

5.4. Radionuclide Imaging

Radionuclide imaging (RI) is another imaging technique that can be applied for deep tissue inspection and imaging. The imaging by RI can be whole-body imaging, which shows an obviously larger scan range than other imaging techniques. It also has the advantage of high sensitivity.[320] The RI commonly includes γscintigraphy, PET, and SPECT. RI usually requires the introduction of exogenous agents such as radionuclides. In SPECT, the γ ray is emitted directly, while the γ ray generation is indirect for PET. The resulting γ ray can penetrate biological tissues and be tracked in the real-time mode using imaging. The actuation of m-bots by using RI inspection to obtain the feedback was proposed based on the encapsulation of positron or gamma emitters. Recently, Vilela et al.[67] applied the PET-CT to track 124I-functionalized bubble-propelled microtubes that were fabricated by the template-directed electrodeposition method followed by the metal evaporation process. The radiolabeling process of the 124I microrobots through chemisorption on the gold surface is crucial for imaging using PET-CT, which broadenes the application of such microrobots from in vitro to in vivo. The authors used linear phantoms to demonstrate location tracking of the microtubes by applying PET combined with X-ray CT. The study involved the investigation of direct tracking of m-bots using commercially available medical imaging platforms, making clinical microrobots foreseeable in the near future.

RI has two main limitations: despite many safety regulations in place, exposure to ionizing radiation due to the X-ray and radionuclides is inevitable. The optimal dosage that balances imaging performance with patient safety must necessarily be determined.[321] Research on the propulsion of m-bots with RI-based tracking is in its infancy and has a long way to go.

Apart from the above-mentioned imaging techniques, other kinds of imaging tools, such as PACT[322] and clinical optical coherence tomography (OCT),[345] are also integrated for the in vivo tracking of the m-bots. Gao et al.[322] developed a kind of m-bot capsules that can be tracked in real-time fashion by PACT in the GI tract of mouse with high-resolution and fast imaging speed. Due to the limited penetration depth of NIR, the PACT may be a good candidate for the localization and tracking of m-bots inside the tissue and organs with a depth less than ≈7 cm.

For in vitro use of m-bots, as well as for nonbiomedical applications, the actuation of m-bots using the optical microscopic tracking for simultaneous feedback is an affordable option. However, the optical microscope cannot penetrate the tissue to track the bots when applied to in vivo situations. Thus, other medical and clinical imaging techniques suitable for in vivo inspections must, therefore, be used. Although studies on the imaging of the micro-nanorobots have progressed significantly, the field is still in its infancy. Compared with the other aspects of m-bot research, i.e., design, functionalization and actuation, researchers may need to focus more on this aspect due to its decisive role in realizing in vivo applications of the technology. In vitro applications of micro-/nanorobots is well-documented, and deeper study of the microrobot imaging will promote the development of in vivo applications.

6. Biomedical Applications of m-Bots

Although a large number micro-/nanomachines have been proposed in the past two decades and their applications in various surroundings explored, the in vivo use of such devices had not received extensive attention until recent years. Extensive research in this area is slowly bridging the gap between research and actual in vivo application of these machines. The micro-/nanomachine applied for in vivo applications include the micro-/nanomachines applied in actual in vivo environments as well as those under study in in vitro environments and show promise for in vivo applications. Based on the above discussions regarding the design, functionalization, actuation, and localization of the micro-/nanomachines, in vivo applications, such as diagnostics, cell isolation, guided cell growth, targeted delivery, and thrombus ablation, can be addressed by combining these aspects ingenuously (**Figure 12**). Current micro/nano robotic systems toward in vivo applications are mainly adopted in the organs/tissues indicated in Figure 12.

6.1. Diagnosis, Isolation, and Guided Cell Growth

M-bots can be applied for DNA/RNA sensing, isolation and detection of biomacromolecules, and isolation of cells and bacteria from biological samples. Therein, the functionalization of

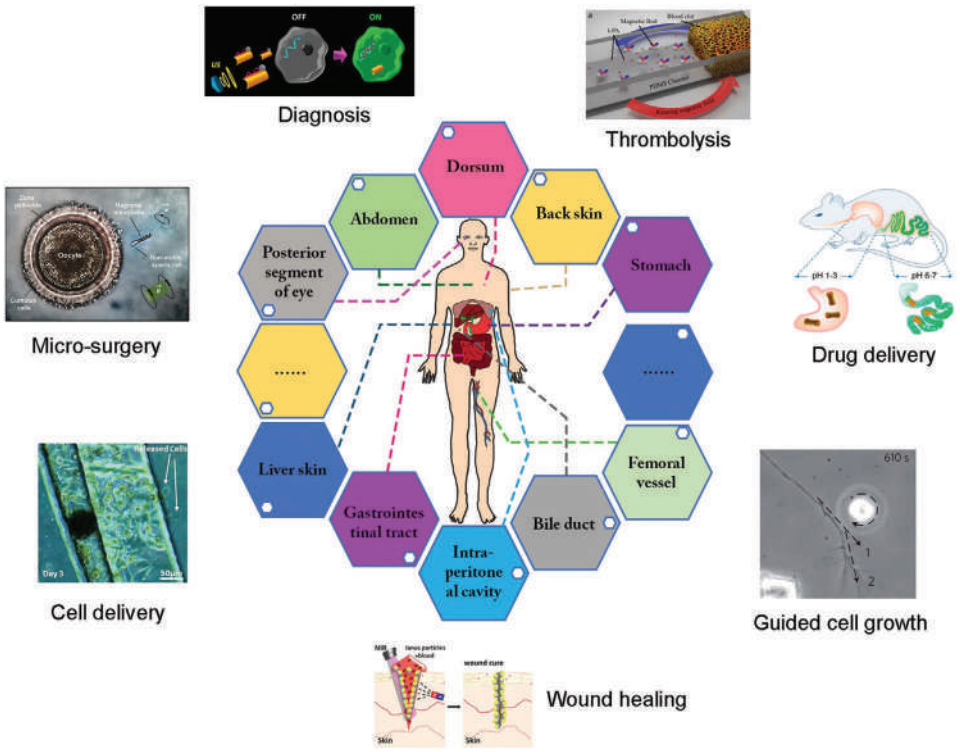

Figure 12. Available biomedical application of m-bots. Insets: Drug delivery: Reproduced with permission.[81] Copyright 2016, American Chemical Society. Cell delivery: Reproduced with permission.[116] Copyright 2018, AAAS. Micro-surgery: Reproduced with permission.[257] Copyright 2016, American Chemical Society. Diagnosis: Reproduced with permission.[334] Copyright 2016, American Chemical Society. Guided cell growth: Reproduced with permission.[336] Copyright 2012, Springer Nature. Thrombolysis: Reproduced with permission.[385] Copyright 2014, American Chemical Society. Wound healing: Reproduced under the terms of the Creative Commons CC-BY license.[360] Copyright 2016, The Authors, published by Wiley-VCH.

m-bots is crucial for diagnostics, isolation, and biosensing applications.[225,323–327] Based on the donor–receptor interactions, m-bots can capture, transport, and release biomacromolecules and cells for isolation purposes.[328–332] Concanavalin A lectin shows strong coupling effect with polysaccharides. As mentioned earlier, microrobots equipped with concanavalin A lectin bioreceptors were efficient in the selective recognition and isolation of *E. coli* owing to the polysaccharides on the cell surface.[126] Boronic acid shows strong interactions with monosaccharides. In a similar approach, Wang et al.[134] also proposed a boronic acid-functionalized microrobot that can selectively recognize and bond with the monosaccharide on the yeast cell, therefore performing the transportation of the yeast cells in media. Another example of donor–receptor interactions is between the anti-carcinoembryonic antigen monoclonal antibody (mAb) and the carcinoembryonic antigen (CEA). CEA is an antigen that is overexpressed in ≈95% of colorectal, gastric, and pancreatic cancers. Zhang and Wang et al.[57] developed an in vitro strategy for the isolation of cancer cells by selective binding and transportation of the cancer cells on the mAb-grafted microrobots. They[333] also proposed ultrasound-actuated nanorobots composed of gold nanowires cloaked with a hybrid of red blood cell membranes and platelet membranes. The intrinsic functional proteins on the hybrid membranes endow the nanorobots with some attractive biological capabilities, such as adhesion and anchoring to Staphylococcus aureus bacteria, and neutralization of α-toxins. The ultrasound-actuated nanorobots moved like naturally occurring motile cells and showed nonadhesive property with respect to blood vessels. These bots exhibited significant potential for applications such as the isolation and removal of different biological threats for detoxification.

Sensing and diagnosis may also be conducted using the micro-/nanomotors. As is known, miRNA is an important biomarker that can be used for diagnosis and therapy. The abnormal expression of miRNA is an indicator of many conditions, which makes the detection of the intracellular miRNA important in clinical diagnosis. For instance, miRNA-21 is found to be overexpressed in 80% of the tumor tissues. Zhang and Wang et al.[334] developed a nanomotor-based strategy that can be efficiently applied to intracellular biosensing and detection of the miRNA-21, which is expressed in intact cancer cells at the single cell level (**Figure 13**a). The nanomotor was composed of a gold nanorod that wrapped the DNA (ssDNA)/graphene-oxide (GO) (Figure 13b), which shows a quenched fluorescence signal due to the π–π interaction between GO and a dye-labeled ssDNA. Under an ultrasound field, the ssDNA@GO-coated gold nanowires can be actuated to penetrate intact cancer cells (Figure 13c). The internalized nanomotor in cancer cell showed an intracellular "OFF–ON" fluorescence switching because of the replacement of the dye-ssDNA by miRNA-21 as schematically illustrated in Figure 13a. The authors applied cancer cell lines, i.e., MCF-7 and HeLa cells, to demonstrate the intracellular detection of the miRNA-21 at the single-cell level. Previous findings[335] indicate that the level of expression in MCF-7 cells is much higher than that in the HeLa cells. The authors then propelled the ssDNA@GO-modified AuNWs with US field under incubation (10 min) and found that the

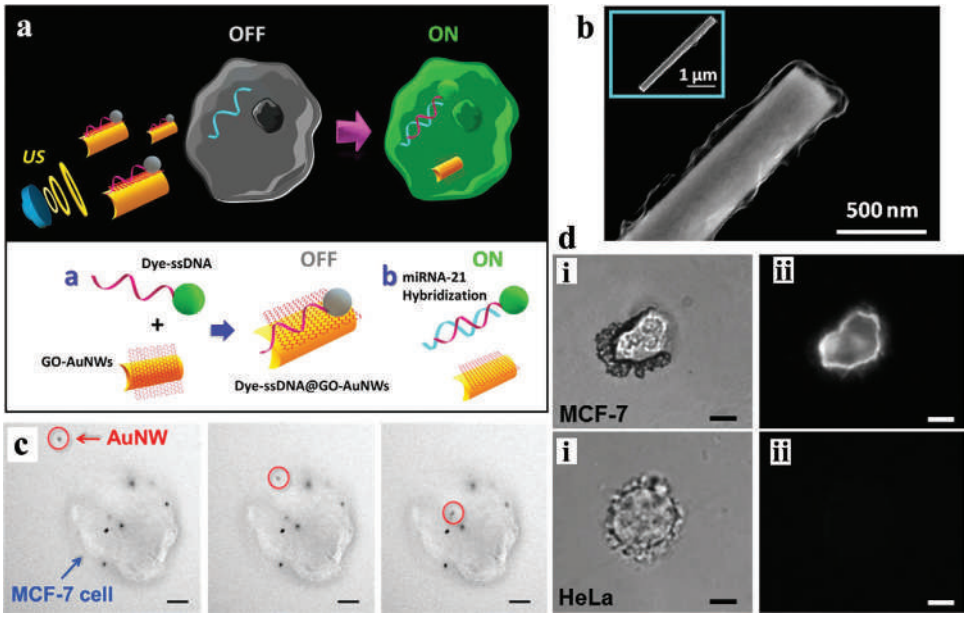

Figure 13. Diagnosis and sensing. a) Schematic illustration of the intracellular detection of the miRNA by the US-actuated functional nanomotors from the OFF-ON switching of the fluorescence of the cells. b) SEM image shows the GO modified Au nanomotor. c) Time-lapse images show the internalization process of a nanomotor (interval is 4 s). d) Optical and fluorescent images give the detection results of the miRNA-21 in the MCF-7 and HeLa cell lines. The scale bars in c) and d) are 10 μm. Reproduced with permission.[334] Copyright 2015, American Chemical Society.

fluorescence intensity of the MCF-7 cells is 44 times higher than that of the HeLa cells (Figure 13d), thus verifying the reliability of their strategy for the detection of miRNA among different type of cells. Such micromotor-based sensing indicates the potential for real-time monitoring of intracellular miRNA expression and cancer diagnosis.

Apart from the transportation and release of the cells, notable microrobot-guided cell growth was also achieved by Berns.[336] The authors developed an optics-based system to guide and control the direction of growth of the individual nerve fibers using a light-actuated spinning microsphere. The rotating micromotor created a localized microfluidic flow with a shearing force of ≈0.17 pN that could control the direction of growth of the nerve cells as shown in **Figure 14**. Another recent finding shows that the delivered micromotors can also induce the differentiation of the neural stem-like cell by converting ultrasonic energy to an electrical signal in situ because of the piezoelectric effect.[337] These micromotor-guided cell growth and differentiation may show potential for in vivo regeneration of axons to mediate brain and spinal cord repair.

6.2. Microscale Surgery

Minimally invasive surgery (MIS) is traditionally carried out by inserting a tethered tool outside the body to the targeted site in body, and it is commonly equipped with a light source, tiny cameras, and mechanical devices for grasping, cutting, and suturing.[338] However, navigation of the tethered tool to the targeted area is difficult and as the tools are not collapsible, they are not useful for tissues with small interspace. To tackle the disadvantages of tethered tools for MIS, wireless capsules that include light sources, tiny cameras, batteries, radio transmitter, and antenna have been developed and commercialized by several companies.[339] These tetherless capsular devices have sizes in the centimeter range and may not be applicable for small vessels and channels in the body. Moreover, most commercial capsules without any external moving parts may only be applied for imaging and sensing, and mechanical operations can hardly be realized with them.

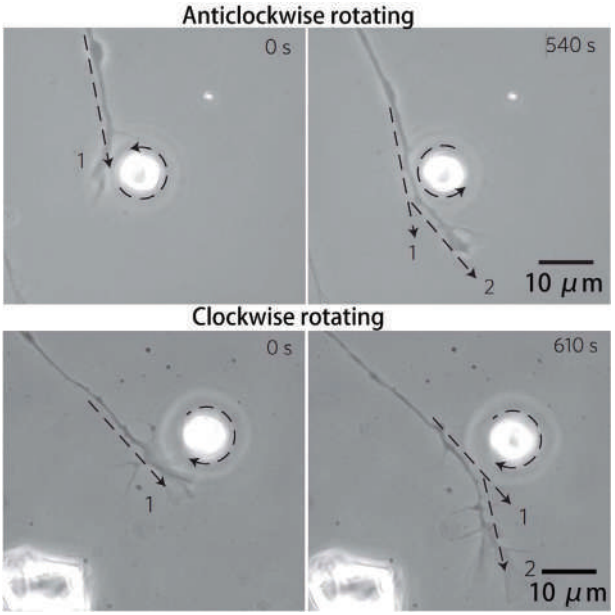

Figure 14. Guided cell growth. The photon-driven micromotor rotating to facilitate guided nerve fiber growth. Reproduced with permission.[336] Copyright 2012, Springer Nature.

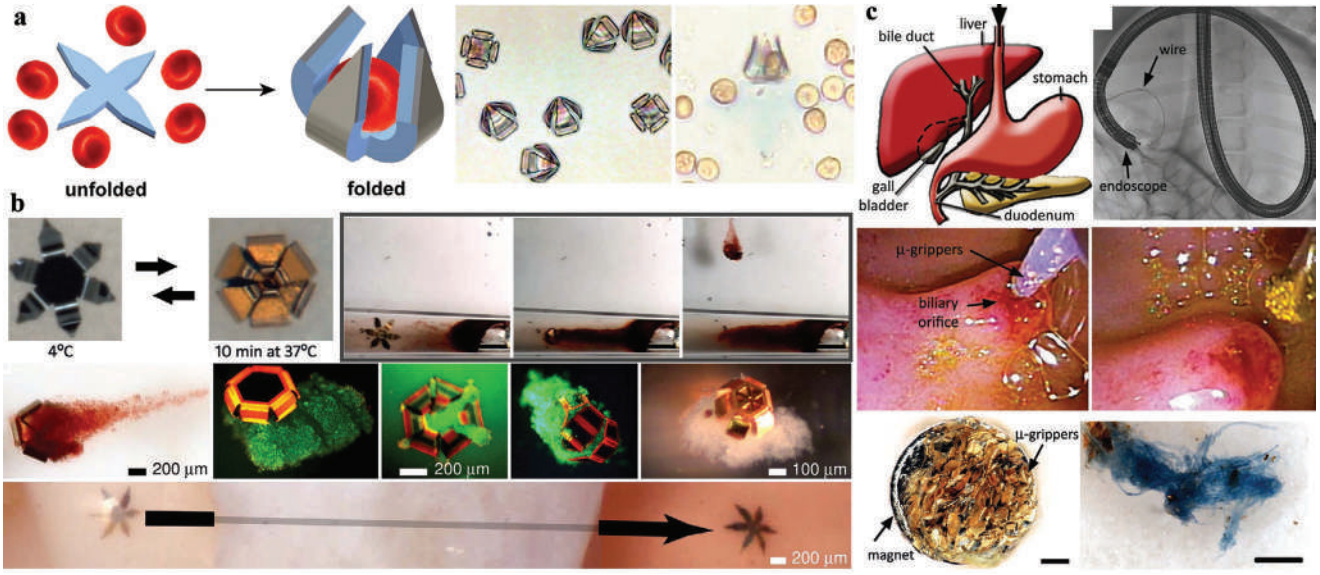

Figure 15. Minimally invasive surgery with microrobots in vessels. a) In vitro capture of the blood cells by self-folding microgrippers. Reproduced with permission.[340] Copyright 2014, American Chemical Society. b) In vitro results show the thermally and biochemically triggered capture of cells mass stained with neutral red in a tube (diameter is 1.5 mm). Reproduced with permission.[54] Copyright 2009, National Academy of Sciences. c) In vivo biopsy of the bile duct by the microgrippers. Schematic of the porcine upper gastrointestinal track. Fluoroscopic image shows the endoscope entering the pig body from mouth and arriving at the duodenum. Endoscopic images show the delivery of the microgrippers to porcine biliary orifice via a catheter and their removal via a magnetic catheter tip. Optical image shows the removed microgrippers on the magnetic catheter tip. The tissue obtained by microgrippers after staining with trypan blue. Reproduced with permission.[341] Copyright 2013, Wiley-VCH.

The well-developed field of remotely actuated micro-nanomachines filled the gap in the microscale world to achieve mechanical motion and operations at the microscale for deep-tissue therapy.

Gracias et al.[340] developed tetherless cell microgrippers composed of biocompatible and bioresorbable silicon monoxide and silicon dioxide that can be applied for grasping the single cells. The tetherless grasping of the cell is realized by the release of the residual stress (**Figure 15**). Further, they[54] proposed a tetherless, thermo-biochemically actuated microgripper with magnetic properties, which was fabricated by photolithography. The microgripper was sized in the range of hundreds of micrometers and navigated magnetically to areas in the body that were inaccessible to tethered or wireless-capsule devices. The thermo-responsive polymer hinges of the microrobots made them rigid at cold temperatures, keeping the star-fish like tool flat and open, and when the temperature was raised to body temperature, these polymer hinges softened and closed to grasp the tissue. After that, the in vivo MIS by the microgrippers were also realized through a delivery process with a catheter and camera for localization. As shows in Figure 15c, the authors[341] showed that the microgrippers could excise tissue samples from real organs and hard-to-reach regions in a live pig. Up to 95% of microgrippers with the obtained tissues could be retrieved with a magnetic catheter tip. Future research may focus on the complete recovery of the microgrippers and elimination of the cytotoxicity of such micromachines. Moreover, the more efficient localization approaches may be applied for the real-time guidance of microrobots to replace the catheter and camera-based imaging system that has limited imaging scope and resolution.

MIS by magnetic microrobots may also be used in the treatment of eye disorders. Due to the transparency of the vitreous body of the eyes, real-time localization of the microrobots in vivo can be addressed quite simply with an optical microscope. Nelson et al.[342–344] proposed an invasive, wirelessly steered and powered microrobot for application in ocular medicine. These microrobots are made of magnetic materials such as CoNi with a coating of Au and PPy (**Figure 16**c). These can be injected without suture along with a hyaluronic acid solution into the eye and precisely steered with an external remote magnetic field with five degrees of freedom (Figure 16a,b).[343] Figure 16d shows the injection process. The microrobots may be precisely navigated to the areas in the eyes that traditional tools can hardly reach. As shown in Figure 16e, the microrobots could arrive at the posterior part of the vitreous cavity close to the retina for the surgery. However, long-term implantation of the microrobots may cause optic nerve inflammation and permanent detachment of the retina (Figure 16f), depending on the implantation period of the microrobots. Histopathologic studies further confirmed the inflammation as showed in Figure 16g. Most recently, Fischer et al.[345] developed a swarm of slippery micropropellers (Figure 16h) that can be magnetically actuated to penetrate the vitreous body (a tight macromolecular matrix) and reach the retina after the surface functionalization of the micropropellers with a perfluorocarbon coating for reducing drag (Figure 16i).

These results suggested that the microrobots are good candidates for the new-generation MIS for the eye, and targeted delivery and diagnostic techniques via implantation in the posterior part of the eye. However, microrobots may be unsuitable for long-term implantation and should be removed after the

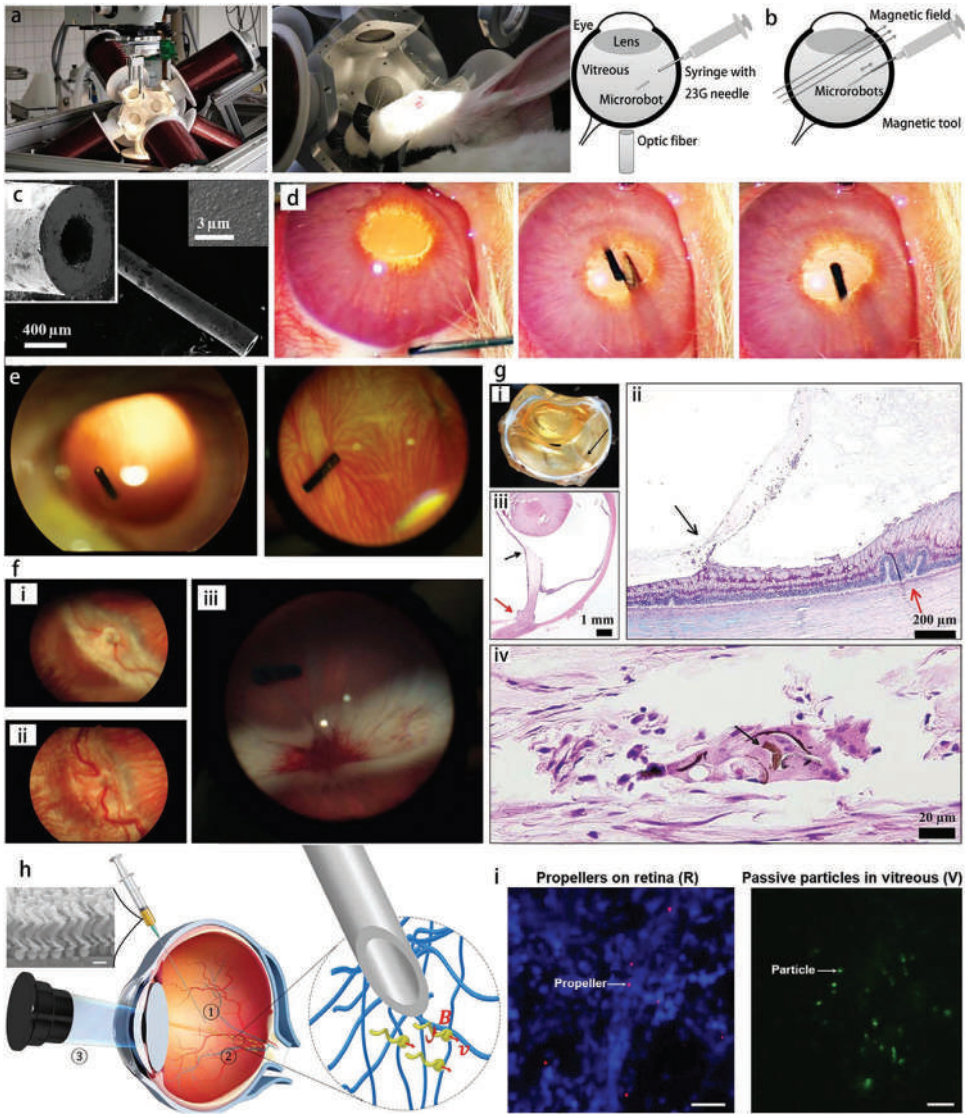

Figure 16. Minimally invasive ocular surgery with microrobots. a) Magnetic actuation system with eight electromagnets for wireless magnetic microrobot control (OctoMag). The lab rabbit was placed at the center of the OctoMag. b) Schematic of the injection and removal of the magnetic microrobot (with a magnetic field applied for orientation of the microrobot). a,b) Reproduced with permission.[344] Copyright 2013, Association for Research in Vision and Ophthalmology; c) SEM images show the magnetic cylindrical CoNi microrobot. d) Successive images show the injection of microrobots into the eye at the center of the vitreous cavity. e) Images show the rabbit eye after one day of microrobot injection. The left one shows the microrobot at the center of the vitreous and the right one shows the microrobot at the posterior area of the vitreous cavity next to the retina. f) Images show the eye i) one day before microrobot injection, ii) 14 days after microrobot injection with optic neuritis, and iii) 28 days after microrobot injection with the complete detachment of the retina. g) Images show the histopathologic changes in eyes after microrobot injection. i) Image shows the hemisected eye with a microrobot in the vitreous. ii) complete detachment of the retina. iii) Image shows the vitreous traction band labelled with black arrow and the retinal fold labelled with red arrow. iv) Image shows foreign matter (may be PPy origin from the microrobot) placed in a multinucleated giant cell labeled with black arrow. c–g) Reproduced with permission.[342] Copyright 2017, Wiley-VCH. h) Schematic of the targeted delivery process of slippery micropropellers with magnetic field. i) Fluorescent images of the retina and the center of vitreous cavity after magnetic actuation of the mixture of the micropropellers (labeled with red fluorescence) and passive particles (labeled with green fluorescence). h,i) Reproduced with permission.[345] Copyright 2018, AAAS.

treatment in a timely manner as tissues in the eye are typically more sensitive than the surrounding ones.

6.3. Targeted Therapy

During the past decades, micro- and nanoparticle-based drug delivery systems have been extensively explored.[346–354] Micro- and nanoparticles shows a lot of merits in drug delivery such as controlled release rate, high loading capacity, and rapid kidney removal.[355–361] However, nanoparticle-based drug delivery commonly relies on the circulatory system, and lack proper drug-targeting and barrier-penetration ability for highly localized therapeutic drug delivery. Sometimes, the passive particles require functionalization to increase the targeting ability. In this respect, active matter and m-bots that can be actuated autonomously or be propelled by external fields, have unique

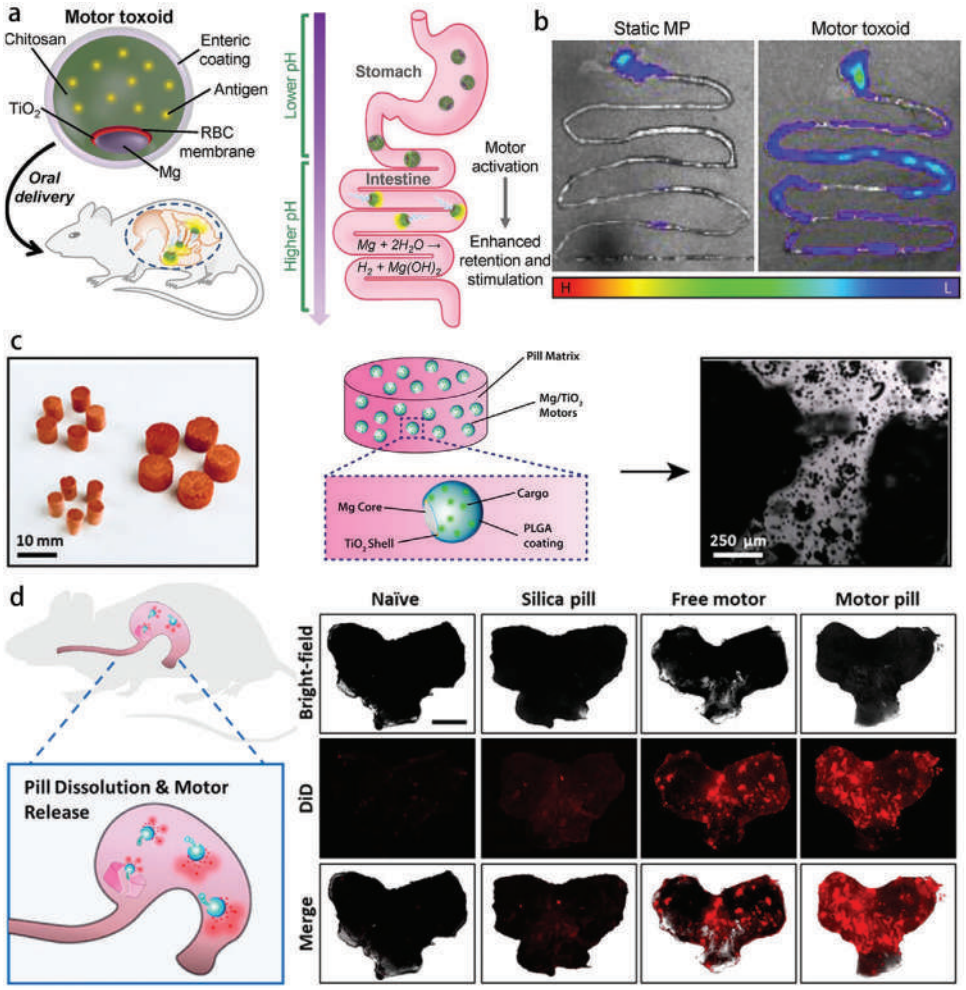

Figure 17. Peroral drug delivery. a) Schematic of micromotor toxoids for oral vaccination. b) Optical images of the gastrointestinal tract of male mice 6 h after the administration of static microparticles or motor toxoids by oral gavage. a,b) Reproduced with permission.[371] Copyright 2019, American Chemical Society. c) Optical image shows the disk-shaped micromotor pills for oral administration. The pill composed of pill matrix and the encapsulated Mg/TiO_2/PLGA micromotors. Right image shows the dissolution and propulsion of the released Mg-based micromotors of a pill in gastric fluid. d) Schematic of the in vivo actuation of a micromotor pill. Bright-field, fluorescent, and merged images shows the mouse stomachs after oral gavage of DI water, fluorescent silica pills, free fluorescent Mg-based micromotors, and fluorescent Mg-based micromotor pills at 4 h. Scale bar is 5 mm. c,d) Reproduced with permission.[373] Copyright 2018, American Chemical Society.

advantages in directed/targeted drug delivery from single cell delivery to local tissue/organ delivery.[362–367] Targeted therapy by m-bots have been achieved for various diseased region via either the peroral route (for gastrointestinal tract) or intravenous injection (via circulatory system) route.[368–370]

6.3.1. Drug Delivery for Gastrointestinal Disease

Mg- and Zn-based m-bots are the most promising among all the m-bots for drug delivery in the peroral route. Guan et al.[55] proposed Mg/Pt-PNIPAM Janus microrobots for the efficient uptake, transport, and temperature-controlled release of drugs. The targeting is achieved by the autonomous motion of the microrobots and on-demand release is realized by the thermoresponsive PNIPAM hydrogel layers. Wang et al.[81] developed an enteric microrobot consisting of a magnesium core and an outer enteric polymer coating. The Mg core allows autonomous propulsion in intestinal fluid and the enteric polymer coating protects the microrobots from being dissolved in the acidic environment of the stomach until the microrobots reach the intestines which have a nonacidic environment. The proposed microrobots can achieve desired biodistribution and enhanced retention in the gastrointestinal tract for site-specific delivery. Based on this strategy, the active delivery of antigens for oral vaccination may be realized as schematically illustrated in **Figure 17**a.[371] When the micromotor toxoid was orally administered to mice, the micromotors entered the stomach and the enteric coating prevented the degradation of the motors in the low pH environment. Improved retention and uptake of antigenic material occurred within the intestinal tract, as demonstrated in Figure 17b. Wang et al.[372] also reported Mg-based microrobots that can autonomously and temporally neutralize gastric acids via the self-propulsion of Mg Janus particles in the gastric fluid by depleting the protons. The drugs loaded within the surface of the pH-responsive polymer layers are, therefore,

autonomously released due to the local pH change caused by Mg neutralization. The in vivo experiment showed that the stomach of the mice treated with Mg microrobots (5 mg) possessed evenly distributed fluorescence intensity generated from the drugs loaded over the entire stomach, demonstrating the microrobots could actively adjust to the stomach environment and dissolve the pH-sensitive polymer for drug release. As for inert PS microparticles, the fluorescence intensity was as low as the DI water control group because the PS microparticles could not change the stomach pH and trigger the dissolution of the pH-responsive polymer for drug release. They[373] further processed the active Mg-based micromotors into micromotor pills that contained the encapsulated micromotors in the pill matrix with other inactive excipients and disintegration-aiding additives from a pharmaceutical strategy (Figure 17c). The in vivo study indicated that the micromotor pill platform effectively protected and carried the active micromotors to the stomach. After the micromotors with the loaded cargo were released from the pill matrix, the micromotors could propel efficiently in the gastric fluid and release the drugs in a concentrated manner. Figure 17d indicated that the florescent Mg/TiO_2/PLGA/chitosan micromotor pill exhibited the most intense signal compared with the DI water, fluorescent silica pill, and free fluorescent Mg/TiO_2/PLGA/chitosan micromotor groups as the micromotor pill enhanced the transportation, dynamic release, and improved retention of the micromotors in the mouse stomach. These results indicated that the combination of traditional pills and the active micromotors offered an appealing route for in vivo motor-based drug delivery applications. Mg and Zn based microrobots[374] show good potential for serving as active drug delivery carriers due to their biodegradable nature that generates harmless by-products and does not require the separation of the microrobots after the delivery process. Further, they[375] fabricated in vivo therapeutic microrobots for active drug delivery for the treatment of a gastric bacterial infection in a mouse model by setting clarithromycin as the model antibiotic for the simulated Helicobacter pylori infection. Compared with passive drug carriers, effective antibiotic delivery was demonstrated by the actuation of the drug-loaded Mg-based microrobots in the gastric media with significant reduction of the bacteria burden in the mouse stomach.

6.3.2. Drug Delivery toward Cancer Therapy

Targeted therapy of tumor is a topic that has attracted extensive research attention.[47,376–382] Pané et al.[382] developed FeGa@P(VDF-TrFE) core–shell magnetoelectric nanowires that can be propelled for targeted drug delivery by using different magnetic fields. The P(VDF-TrFE) nanotubes are prepared by melt-wetting of the AAO template, followed by the electrodeposition of FeGa to generate the FeGa@P(VDF-TrFE) core–shell nanowires. After surface functionalization with polydopamine, the nanowires can be loaded with the anticancer drug paclitaxel. The loaded drug can be released for on-demand killing of cancer cells after alternating magnetic fields are applied to cause the magnetoelectric effect. Intensive drug release may also be realized by the actuated m-bots. Sánchez et al.[376] developed urease-modified mesoporous silica-based core–shell nanorobots that were actuated by enzyme catalysis for the active transport and delivery of the drugs to the sites of interest. Compared with the passive counterparts, a four-fold increase in drug release is achieved by the nanorobots after 6 h of treatment. The authors found that the active DOX-loaded nanorobots shows enhanced effect on HeLa cells compared to passive carriers due to the improved drug release kinetics and ammonia production generated from the catalytic decomposition of urea. A similar strategy is also promoted to treat bladder cancer.[381] The high urea concentration in the bladder acts as the fuel for the autonomous actuation of the nanomotors. Compared with most self-propelled m-bots, the new m-bots that employ enzymes as catalysts open up tremendous application potential for in vivo situations.

6.3.3. Targeted Cell Delivery

Targeted delivery of various cells was also realized by the microrobots.[67,74,383,384] Choi et al.[111] demonstrated the targeted delivery of the cells using the 3D direct laser writing technique. The cage-like microrobots were coated with Ni and Ti layers to endow them with magnetic and biocompatible properties (**Figure 18**a). After being cultured in 3D with the HEK 293 cells, they found that the cells readily adhered, migrated, and proliferated over the scaffold of the 3D microrobots (Figure 18b). The microrobots loaded with cells can be propelled using an external magnetic field gradient. The proposed microrobots can be applied for the targeted micromanipulation of the cells for in vivo applications. Sun et al.[116] proposed another biocompatible burr-like microrobot that can load the cells on the 3D framework via 3D cell culture (Figure 18c) and release them at the desired site with ease (Figure 18d). The in vivo release of stem cells by this kind of microrobots has been also verified from subcutaneous injection at the dorsum of nude mice with the tracking by FI (Figure 18e).

6.4. Thrombus Ablation

Obstruction of blood vessels due to blood clots is one of the leading causes of death in the world.[382,385] Thrombosis may appear at diverse sites and depending on the site of the thrombus, it may lead to ischemic stroke, coronary infarction, pulmonary embolism, and so on. Two strategies are developed for thrombus ablation, namely thrombectomy and thrombolysis. Thrombectomy involves using a catheter to remove the thrombus mechanically through the blood vessel. However, it has many contraindications and the catheter may not reach the vessels with small diameter.

Thrombolysis is another strategy for removing blood clots by drug-induced lysis. Tissue plasminogen activator (tPA) is one of the drugs for thrombolysis that has been approved by US Food and Drug Administration (FDA). It can catalyze the transformation of plasminogen to plasmin and the generated plasmin can break up the thrombus via binding with the fibrin on the blood cells. Commonly, thrombolysis is performed by an intravenous injection and the dose of the tPA should be controlled to less than 0.9 mg kg^{-1} due to potential side effects such as internal hemorrhage. The rapid and efficient delivery of tPA

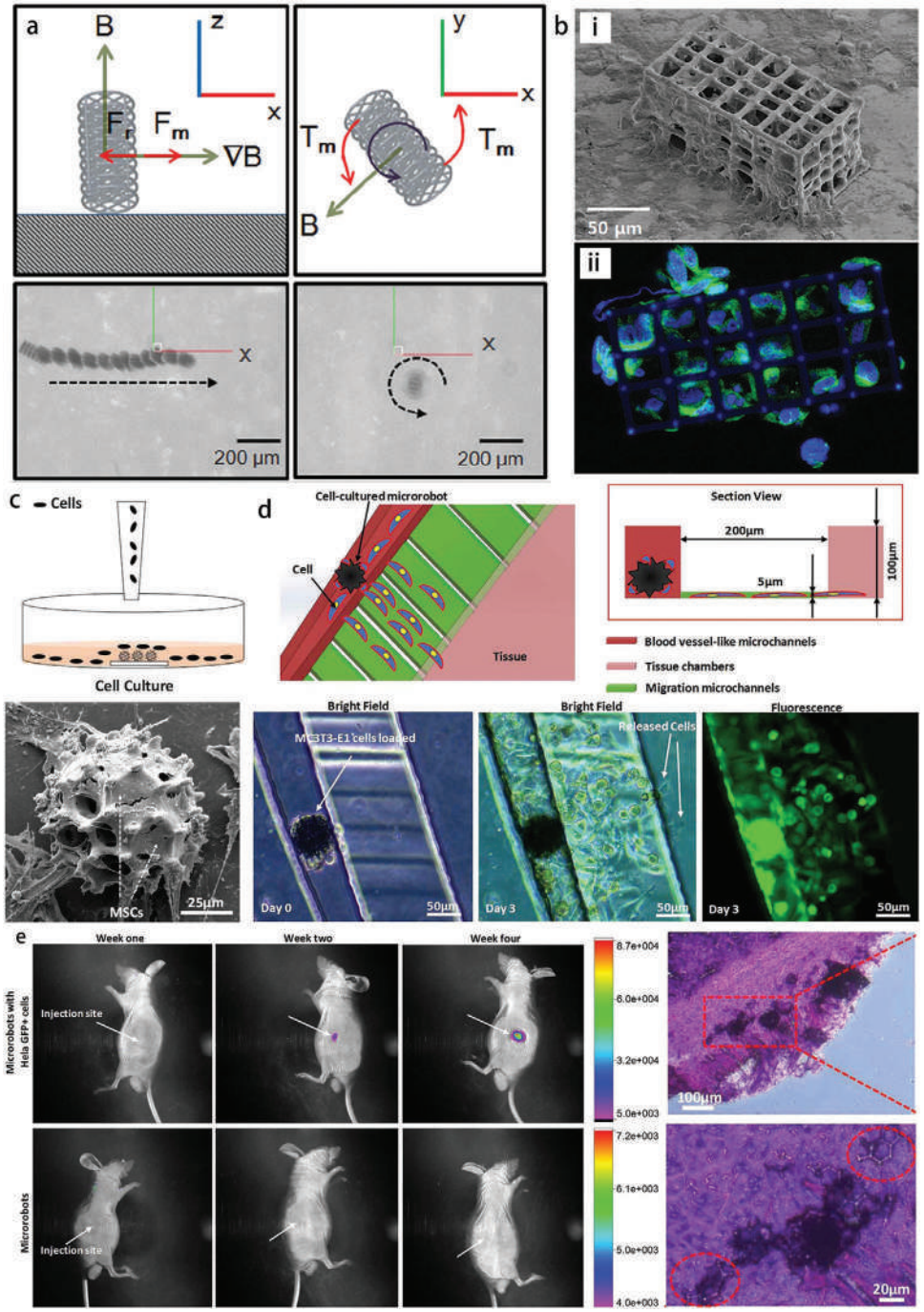

Figure 18. Targeted cell delivery. a) Schematic and optical images show the translational and rotational motion of the microrobots. b) SEM and fluorescent images show the microrobot loaded with cells. a,b) Reproduced with permission.[111] Copyright 2013, Wiley-VCH. c) Cell culture process on the burr-like microrobots. SEM images shows the burr-like microrobot cultured with MSCs for 12 h. d) In vitro cell release process of the burr-like microrobot in a microfluidic chip. e) Fluorescence images show the in vivo cell release experiments on nude mice. The upper images show the left dorsum of mice injected with microrobots carrying HeLa GFP+ cells. The lower images show the right dorsum of mice injected with microrobots carrying no cells. The section of HeLa tumor contains the injected microrobots. c–e) Reproduced with permission.[116] Copyright 2018, AAAS.

by the carriers after the onset of thrombosis is crucial for the treatment. In recent years, due to the rapid development of the field of m-bots, researchers have promoted the utilization of the m-bots in the efficient removal of the thrombus.[132,385–391]

The macroscale helical robots with lengths in the centimeter range were applied to drill holes by mechanical rubbing inside the blood clot with the assistance of thrombolytic agents. Sitti et al.[386] verified and conducted the experiments on the in vitro model and found that mechanical rubbing with the helical robots showed a removal rate approximately three times larger than that of chemical lysis with streptokinase. Moreover, the removal process can be tracked with ultrasound guidance.[387]

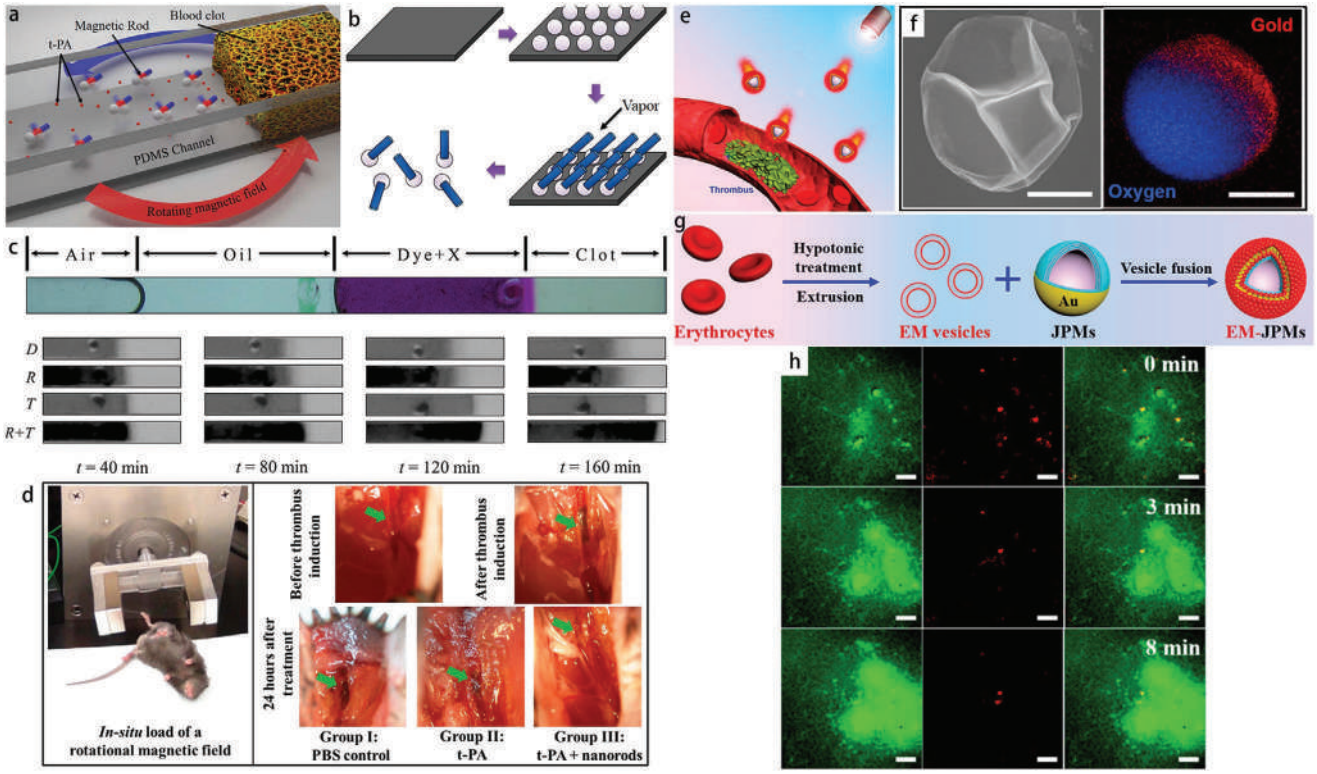

Figure 19. Thrombus ablation. a) Schematic of the nanorobot-enhanced thrombolysis process with free tPA under an external rotating magnetic field. b) Fabrication process of Nickel nanorods. c) Optical images show the in vitro experiment of the thrombolysis process with dye (D), nanorobots (R), tPA (T), and nanorobots + tPA (R+T) at different time points. d) Optical images show the in vivo experiment of the enhanced thrombolysis by the nanomotors in a mice embolism model. a–d) Reproduced with permission.[385] Copyright 2014, American Chemical Society. e) Schematic of photothermal therapy of the thrombus. f) SEM image of Janus polymeric motors after template removal and EDS mapping of the Janus polymeric motors before template removal. Scale bar is 2 µm. g) Schematic of the modification process of Janus polymeric motors with erythrocyte membrane by the vesicle fusion method. h) Successive CLSM images show the variation of fluorescent thrombus in the presence of membrane-cloaked Janus polymeric motors under NIR (760 nm) irradiation. Scale bar is 20 µm. e–h) Reproduced with permission.[389] Copyright 2018, American Chemical Society.

Zhao et al.[385] developed active nickel nanorods to directly guide and enhance the tPA-mediated thrombolysis (**Figure 19**a,b). The results demonstrated that nanorobots can be used for enhancing tPA thrombolysis speed using magnetic-field generated hydrodynamic convection (Figure 19c). Efficiency of thrombolysis is also verified by the in vivo experiment on a mouse (Figure 19d). Engelhard and co-workers[388] applied a rotating permanent magnet to rotate and translate of iron oxide NPs inside the vessel so that the drugs can be directed to the thrombus site with a stagnant flow. Hest et al.[389] constructed erythrocyte membrane-cloaked Janus polymeric microrobots (Figure 19f,g) which were actuated by near-infrared (NIR) laser illumination for thrombus ablation (Figure 19e). These biodegradable and biocompatible microrobots can generate a local thermal gradient under NIR irradiation because of the asymmetric distribution of Au on the surface of the microrobots, causing "on/off" controlled motion of the microrobots by the self-thermophoresis effect generated by the control of the irradiation source. Therapeutic microrobots showed excellent performance in thrombolysis photothermal therapy (Figure 19h). Compared with the traditional methods that involve intravenous injection of tPA, the nanorobot-guided therapy may require smaller doses of the drug due to the locally accelerated flow effect.[392] Accordingly, the potential side effects of tPA may be reduced to some extent. Also, the m-bots can form a thrombin-inhibiting coating that is capable of preventing the regeneration of the thrombus.

6.5. Wound Healing

A wound is an injury to the body that may originate from various external forces such as accidents, violence, or surgery, and may be in the form of abrasions, lacerations, punctures, avulsions, or animal bites. It usually involves the breakage of the organ skin and may cause possible damage to the underlying tissues. Most of the people experience an open wound at some point in their life. Proper treatment of wounds is crucial since inappropriate treatment increases the chances of bacterial infection. Minor wounds can be treated by oneself at home while large or deep wounds are better handled by a doctor. Wound healing can be typically classified into four successive stages, namely, the hemostasis phase, inflammation phase, proliferation phase, and remodeling phase. Open wounds are conventionally closed and healed using skin glue, medical sutures, laser welding etc. However, these strategies are either invasive or require a long time for rehabilitation after treatment, and thus, affect the daily activities of the patient. Nanoparticles, nano scaffolds, and other biomaterials have also been developed to perform topical drug delivery for wound healing.[393–395]

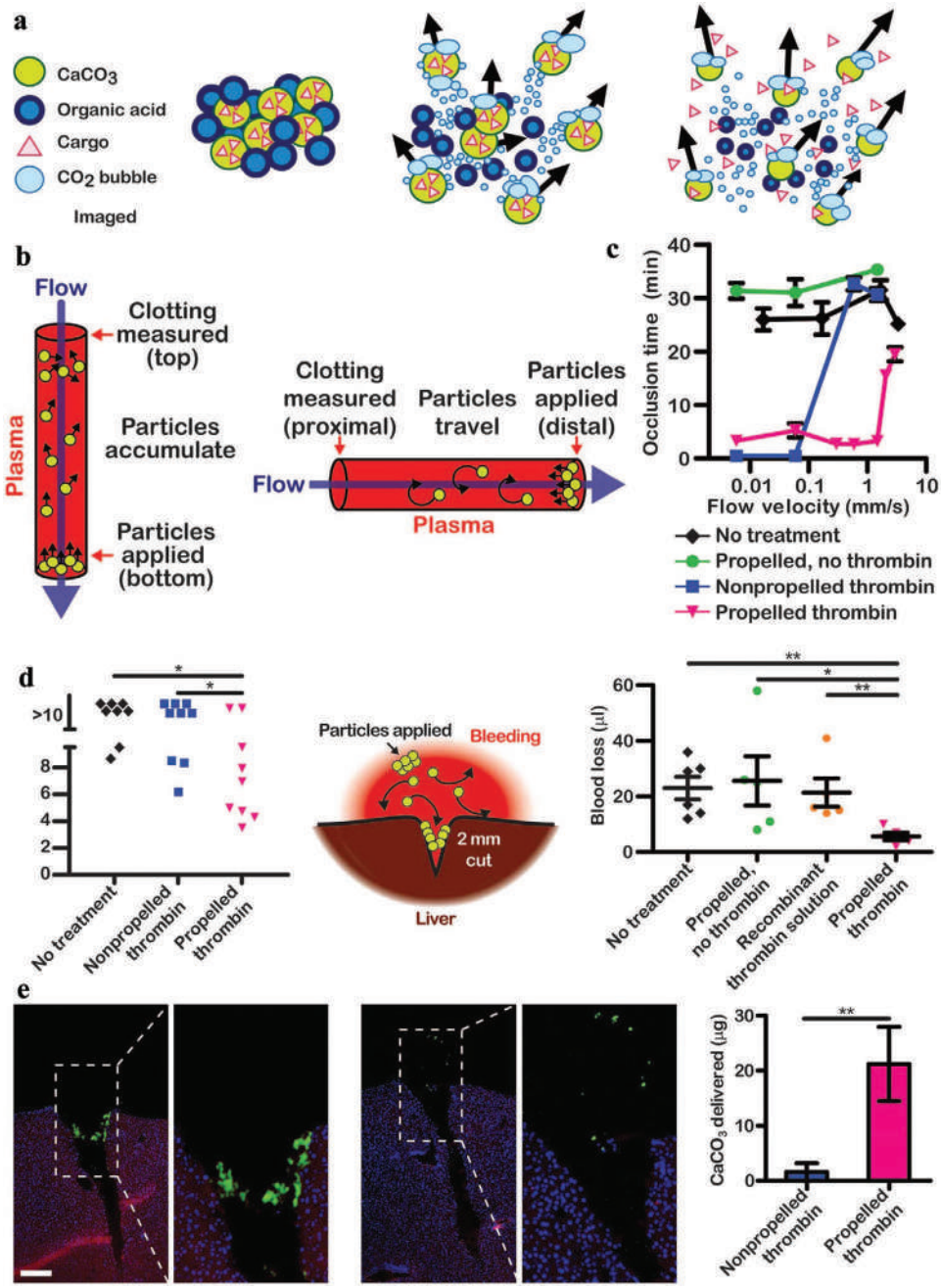

Figure 20. Active motor-based wound healing. a) Schematic of the propulsion of micromotors in water by release of CO_2 and accompanying cargo delivery process. b) Schematic of clotting and occlusion of flowing blood plasma ex vivo in vertical and horizontal directions. c) Relationship between the clotting occlusion time and the flow rate in a vertical orientation. d) Left graph shows the bleeding times of mice after tails were amputated. Right graph shows the volume of blood loss of mice after the livers were punctured and subsequently treated. e) Fluorescent images show the histological sections of liver treated with propelled and nonpropelled thrombin. Right graph shows the dose of the $CaCO_3$ delivered to punctured liver sites. Reproduced with permission.[359] Copyright 2015, AAAS.

However, passive delivery of therapeutics into damaged deep tissue during bleeding remains a challenge due to the outward flow of the blood. The development of the m-bots offers a brand-new strategy for an enhanced healing effect despite the outward blood flow. Treatment of wounds with the micro-/nanomotors results in reduced clotting velocity of the blood and accelerated wound healing rate compared with the conventional treatment methods. Moreover, the nanomotor-based healing techniques are minimally invasive and do not introduce new trauma like traditional stitches.[358]

Kastrup et al.[359] proposed self-propelled micromotors made of carbonate and tranexamic acid (**Figure 20**a) that can navigate through aqueous solutions with a maximum speed of 1.5 cm s^{-1} due to the release of CO_2 and can move against the blood flow. Three animal models, namely, mouse liver, mouse tail, and pig femoral artery, have been used to verify the enhanced delivery

of the coagulation enzyme and staunching of severe hemorrhage (Figure 20b,c). When the micromotors were loaded with thrombin, they could penetrate deeply into the wound (Figure 20c), shorten the bleeding time, and reduce blood loss efficiently (Figure 20d). The system shows far-reaching applications for the delivery of therapeutics, and may potentially be applied for postpartum hemorrhage, which is one of the main risks for maternal mortality in childbirth. He et al.[360] further developed magnetic field- and NIR- actuated Janus micromotors with high controllability for restoration and hemostasis of wound by laser beam irradiation. Local temperature rose in the wound melted the collagen fiber and temperature reduction led to the formation of a collagen film that closed the open wound. Micromotor assisted welding of wounds was verified on beef liver, beef meat, and chicken meat and showed in the improved, laser-controlled halting of bleeding.

Active micromotor-based halting of hemorrhage is significant in the case of severe and massive trauma, such as the postpartum hemorrhage and combat wounds. The patient is at risk for hypovolemic shock and may die due to the exsanguination. Fast-acting active delivery of the hemostatic agent by the micro-/nanomotors locally to the deep, difficult-to-reach wound increases the possibility of saving the patient's life.

6.6. Biomedical Applications of Swarming m-Bots

The swarming behavior of the m-bots not only broadens the scope of understanding related to self-assembly behavior in natural living systems as introduced in Section 4.7, but also brings out the potential for applications such as the multiple cargo manipulation,[273,396,397] antidiffusion by the swarming m-bots,[287] enhanced delivery capability (**Figure 21**a),[398] reconfigurable adjustment of the energy delivery dose for enhanced magnetic hyperthermia (Figure 21b),[399,400] and cell alignment (Figure 21c) and manipulation of intracellular organelles.[401] The in vivo swarming behavior of biological and artificial m-bots have been investigated and explored, and it has been verified that the collective motion behavior of micro-/nanoagents can commonly realize the enhanced delivery of drugs and energy.

By combining the enrichment of MC-1 in the oxygen-depleted hypoxic regions of the tumor and magnetic field guidance, Martel et al.[398] examined the magnetoaerotactic and collective migration behavior of magnetotactic bacteria (MC-1) and applied this to the transportation of drug-loaded nanoliposomes into the hypoxic regions of the tumor for cancer therapy. The peritumoral injection of MC-1 into the tumor xenograft in mice showed that directional magnetic fields can considerably enrich MC-1 in the central hypoxic region of the tumor as shown in Figure 21a. The MC-1 stained with antirabbit FITC-labeled secondary antibodies exhibits a higher density at 4 and 6 cm which is at the center of the tumor than at the boundary region. The surface of the MC-1 can be anchored with several liposomes with drug loaded in them for targeting to the tumor center with a directional magnetic field. The result indicated that the targeting ratio could reach up to 55% (Figure 21a) in the tumor with this kind of collective motion by magnetic field. The work demonstrated the merit of the swarms of microorganisms with magnetoaerotactic behavior could efficiently boost the therapeutic index of various nanocarriers in tumor hypoxic regions.

Zhang et al.[399] developed a new strategy to realize a tunable energy dosage by using a reconfigurable swarm of ferromagnetic particles via remote and nonintrusive magnetic field control combined with a radio-frequency alternating magnetic field. The advantage of this strategy is that the initial particle dose could be maintained at a low level to reduce the toxicity to the surrounding cells/tissue. The local particle concentration could be tuned within a wide range under a magnetic field. The shrinking of the particle swarm pattern would induce a higher localized temperature rise after the alternating magnetic field treatment whereas the swelling of the particle swarm pattern would induce a lower temperature rise (Figure 21b). Also, the locomotion of the particles swarm pattern could be easily controlled for targeted energy delivery of certain location. The magnetic particle swarm offered a new means for achieving enhanced the localized treatment of the tumor with a relatively low initial particle dose.

Wang et al.[401] investigated the ultrasonic propelled axial propulsion and spinning of the Au rod inside the living HeLa cells without chemical fuels. The cells can be properly aligned under the ultrasonic field with a cluster of Au rods (Figure 21c), and the internalized Au rods showed active motion in the cells. The authors suggested that the ultrasonic propulsion of nanomotors may offer a new tool for stimulating the living cell by mechanical excitation and intracellular organelle manipulation.

7. Comprehensive Evaluation of State-of-the-Art In Vivo Applications

To date, in vivo applications of the micro-/nanomachines, such as microsurgery, drug delivery, cell delivery, thrombus ablation, and wound healing have achieved preliminary success in animal models, such as different organs and tissues of mouse, rat, and pig, as listed in **Tables 4** and **5**. Among all the real in vivo applications, three kinds of propulsion modes are extremely popular and favored for the steering and actuation of the micro-/nanomachines, i.e., magnetic field, bubbles, and light field. Studies on other modes of propulsion remain in the stages of in vitro and ex vivo investigation. Among these three propulsion modes, magnetic field-based propulsion and bubble-based propulsion are applicable for both superficial and deep tissues whereas the light field is applied only for superficial treatment like wound healing. As for the imaging of the in vivo treatment procedures with micro-/nanomachines, researchers have hitherto realized the localization of the tiny robots and the nidus using endoscopy, FI, and MRI. Different imaging techniques are usually used for different applications. Endoscopy is applicable for the imaging of micro-/nanomachines in the in vivo ducts. FI is a good candidate for the superficial localization of tiny robots with high-resolution. MRI is a reliable localization technique for deep tissue imaging. The delivery strategies of micro-/nanomachines are commonly completed by catheter delivery from mouse, oral administration, IV injection, topical application and in situ injection. Most of the real applications did not conduct any postclearance process after the treatment. However, for the bubble-propelled micro-/nanomotors based on Mg and $CaCO_3$, the motors gradually dissolved in the stomach and wound site with low cytotoxicity after treatment and no further removal processes were required.

Other proposed applications for micro-/nanomachines, which show tremendous potential for in vivo applications, have

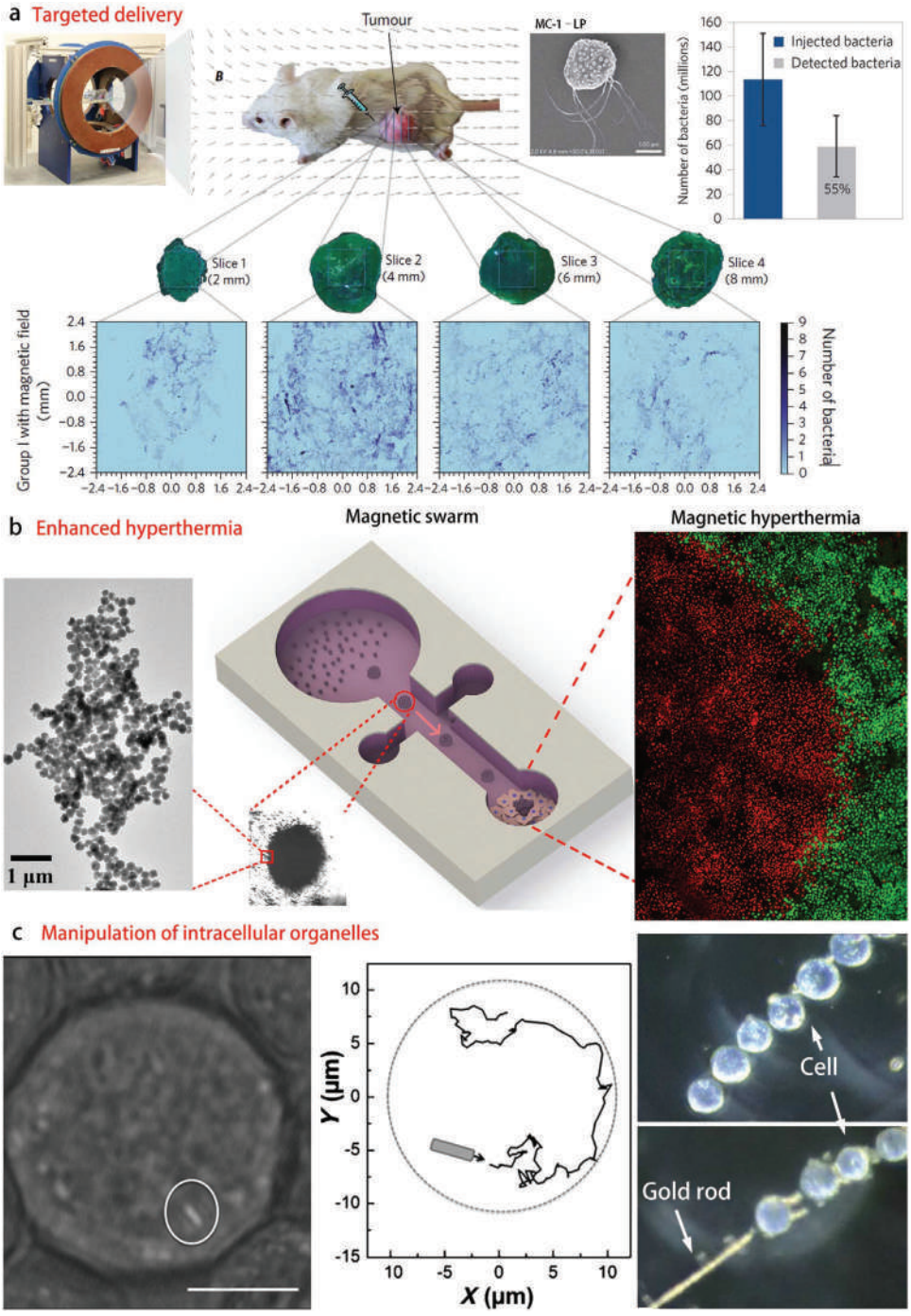

Figure 21. Swarming m-bots toward in vivo applications. a) Optical image shows the magnetotactic directional control system. Peritumoral injection of the MC-1 into the tumor xenograft in mice (the magnetic field direction was aligned to the tumor center). The distribution of MC-1 in tumor sections at different distances from the injection site. The inset in the top right corner gives the SEM image of the MC-1 anchored with drug-loaded liposomes (MC-1-LP) and the estimated amount ratios of the MC-1-LP in the tumor after the magnetic field guided targeting process of a cluster of MC-1-LP. Reproduced with permission.[398] Copyright 2016, Springer Nature. b) The motion of colloidal swarm for targeted and enhanced magnetic hyperthermia (the green color in the fluorescent image represents the live cells, and the red color represents the dead cells). Reproduced with permission.[399] Copyright 2018, Wiley-VCH. c) The trajectory of a gold rod inside a HeLa cell. The optical images show that the gold rods can cause the rotation of HeLa cells to which they bound at the acoustic nodal line. Reproduced with permission.[401] Copyright 2014, Wiley-VCH.

not successfully transferred the in vitro and ex vivo models to the corresponding in vivo cases, such as hyperthermia, micromotor guided neural repair, infertility, and cancer diagnosis. Among all these propulsion modes, the magnetic field is still the most popular one and US propulsion becomes relevant for in vitro and ex vivo applications. We foresee that the US propulsion

Table 4. Summary of the in vitro and ex vivo applications of m-bots.

In vivo/ex vivo trials	Material	Geometry	Propulsion mode	Method	Type of cells	Proposed disease treatment	Delivery site	Imaging method	Year	Refs.
Target interventions in blood	Magnetotactic bacteria	Sphere with flagella	Magnetic	Not mentioned	None	None	None	MRI	2009	305
Guided cell growth	Vaterite	Sphere	Light	Not mentioned	Nerve bras	Neural reparation	Outside cell	BF	2012	336
3D cell culture and transportation	Photoresist, Ni, Ti	Cuboid framework structure	Magnetic	DLW	Human embryonic Kidney 293 cells	Drug delivery and cell delivery	Outside cell	FI	2013	111
Sperm delivery	Photoresist, Ti, Fe	Microtube	Magnetic	Photolithography and PVD	Sperm	infertility	Outside cell	BF	2013	256
	Sperm, photoresist, Ni, Ti	Helical flagella	Magnetic	DLW and PVD	Sperm, oocyte	infertility	Inside cell	BF	2015	257
Cancer diagnosis	GO, Au, DNA	Wire	US	Template-directed electrodeposition and surface grafting	MCF-7, HeLa	Cancer diagnosis	Inside cell	FI	2016	334
Cargo delivery	SU-8, PNIPAM-AAC, Fe_2O_3	Starfish-like gripper	Magnetic	Photolithography	None	None	None	US	2017	319
Hyperthermia	Fe_3O_4	Sphere	Magnetic	Solvothermal	HepG2, HeLa and 3T3	Cancer therapy	Outside cell	FI	2018	399
Thrombus ablation	Erythrocyte membrane, Au	Sphere	Light	LbL assembly and sputter coating	Erythrocyte	Vascular thrombosis	Outside cell	FI	2018	389
Drug delivery	Sperm, photoresist, Fe, Ti	Flagella with a helmet	Magnetic	DLW	Sperm, HeLa	Cancer therapy	Outside cell	BF	2018	259
	SiO_2, Ni, perfluorocarbon coating	Helical structure	Magnetic	Glancing angle deposition	Retina cell	Ocular disease	Porcine eye (ex vivo)	BF and optical coherence tomography	2018	345

may be successfully applied for in vivo cases soon. Among all these propulsion modes, their prospect and significance may be ranked according to the frequency of use in in vivo applications: magnetic field > light field > bubble > US field. The short effective actuation range of the magnetic propulsion system may be a considerable challenge for the translation of these methods from the lab to human clinical cases because the attractive force between the magnetic m-bots and the magnetic field is inversely proportional to no less than the fourth power of the distance. As for the localization of the m-bots, the BF is the most frequently applied imaging mode for in vitro and ex vivo trials, whereas for actual in vivo trials, the FI is the most widely used localization technique. Besides BF, FI and US imaging are also developed for the in vitro/ex vivo applications.

Based on the above discussions, we believe that m-bots hold significant potential for broad development. First, several propulsion modes have not yet developed to the stage of in vivo applications, such as electric field-propelled micro-/nano-machines. As for the implemented propulsion modes for in vivo applications, the targeting regions are limited to, in turn from top to bottom of a mammal, the stomach, bile duct, mouse liver, abdomen, back skin, intra-peritoneal cavity, gastrointestinal tract, and femoral artery. The feasibility of m-bots for the treatment of other organs and tissues of mammal with different pathologies have not yet been verified. Second, existing localization methods of the m-bots for the real in vivo applications are mainly endoscopy, FI, MRI, PACT, OCT, etc. The other kinds of novel imaging techniques should be studied for integration with the propulsion modes toward real in vivo localization. Third, most researchers are aware of the need to avoid cytotoxic materials for in vivo applications, such as the replacement of Ni with Fe_3O_4. However, the clearance of the m-bots is seldom evaluated in most cases according to the data in Tables 4 and 5, though several researchers have used biodegradable materials that self-dissolved after use and magnetic materials that can be retrieved using a magnetic catheter tip.

8. Conclusion and Outlook

Although considerable efforts have been made in the development of microrobotic platforms for the biomedical applications, it is still a huge challenge to achieve realistic biomedical tasks in vivo due to several issues in the design, functionalization, actuation, and localization of m-bots, and the integration of the actuation system and real-time imaging system with living organisms for specific tasks and treatments.

8.1. Design

For an in vivo application, the usage of biocompatible/biodegradable materials is fundamental to the initial design and fabrication process. Inevitably, some m-bots use toxic materials as

Table 5. Summary of the in vivo applications of m-bots.

In vivo applications	Material	Geometry	Propulsion mode	Method	Animal model	Targeting site	Delivery method	Imaging method	Clearance	Year	Refs.
Microsurgery	Cu, Ni, Cr, Si, polymer	Starfish-like gripper	Magnetic	Photolithography	Pig	Bile duct	Catheter from mouth	Endoscopic imaging	Remove with magnetic catheter tip	2013	54
Thrombus ablation	PS, Ni	Rod-like	Magnetic	Oblique angle deposition	Mouse	Femoral vessel	Retro-orbital IV injection	None	Not mentioned	2014	385
Delivery	Photoresist, Ni, Ti, NIR-797 dye	Helical flagella	Magnetic	DLW and surface grafting	Mouse	Intraperitoneal cavity	Injected in intraperitoneal cavity	FI	Not mentioned	2015	44
Wound healing	$CaCO_3$, Organic acid,	Sphere	Bubble propulsion	Wet chemical method	Mouse and pig	Mouse liver and tail, pig femoral artery	Topical application	None	Dissolved	2015	359
	SiO_2, Fe_3O_4, PEM, Au	Sphere	Magnetic, light	LBL	Mouse	Back skin	Topical application	None	Not mentioned	2016	360
Drug delivery	Mg, Au, PEDOT enteric coating	Tubular	Bubble propulsion	Template method	Mouse	Gastrointestinal Tract	Oral administration	Ex vivo imaging with FI	Dissolved	2016	81
	Magnetotactic bacteria, LP	Sphere with flagellum	Magnetic	Surface grafting	Mouse	Abdomen	Peritumoral injection	None	Not mentioned	2016	398
	Mg, TiO_2, PLGA	Janus sphere	Bubble propulsion	ALD	Mouse	Stomach	Oral administration	Ex vivo imaging with FI	Dissolved	2018	373
Intraocular surgery	CoNi, Au, PPy	Cylindrical structure	Magnetic	Electroless deposition	Rabbit	Posterior segment of eye	Sutureless injection	BF	Not mentioned	2017	342
Delivery	Spirulina microalgae, Fe_3O_4	Helical	Magnetic	Dip-coating	Mouse and rat	Intraperitoneal cavity and stomach	In situ injection and oral administration	FI and MRI	Not mentioned	2017	64
3D cell delivery	Photoresist, Ni, Ti	Burr-like framework structure	Magnetic	DLW	Mouse	Dorsum	Subcutaneous injection	FI	Not mentioned	2018	116

the important components, which may limit their further applications in in vivo therapy. For instance, nickel is an efficient material that is usually applied for the fabrication of magnetic m-bots, in photolithography, direct laser writing, electrodeposition techniques, etc. However, nickel is commonly deemed as a toxic material for cells and tissues that should be avoided or at least encapsulated in biocompatible soft shells to prevent direct contact with cells for in vivo applications. To improve the biocompatibility, FePt and Fe_3O_4 with much lower cytotoxicity may be applied for the in vivo applications. Besides, the design and fabrication of micro- and nanorobots are depending mainly on ≈20 elements, and most of them are the transition metals with a few of them from the Group IIA, IIIA, IVA, VA, and VIA elements of the periodic table. More than two-thirds of the transition metals are excavated for use as core materials of m-bots. The future directions of the design and fabrication may shift to the use of other elements for the integration of multifunctionality.

8.2. Functionalization

With the development of the bioconjugate techniques, the surface functionalization and labeling of the m-bots with ligands, peptides, proteins, nucleic acids, lipids, polymers, and functional QDs through certain target groups have been performed well. The surface wetting property is usually neglected for the m-bots even though it has been widely considered in the design of macroscale robots for locomotion on the water surface and water/oil interfaces, as in the water strider.[402–405] M-bots are always intrinsically hydrophilic and can be navigated in water-based media. The surface functionalization with special wetting molecules[403–405] may offer brand-new applications for the m-bots for interface-based navigation that shows reduced resistance to the swimming. Fischer et al.[345] have given a good example that the drag force and adhesion can be well reduced via hydrophobic coating during the navigation of m-bots inside body.

8.3. Actuation

In most cases, the actuation and steering of m-bots occur in the 2D planar situation. However, for practical applications, the navigation of a m-bot inside a blood vessel is quite sophisticated. To date, a few studies have been conducted to study the motion of m-bots in 3D space with feedbacks of the 3D localization.[265,406] The future investigation of the m-bots may pay

significantly more attention to the locomotion of the m-bots in the 3D form, especially for the 3D navigation of multiagents and the swarming of a cluster of m-bots. Second, several types of m-bots still lack the directional steering required for targeted locomotion. Some external fields, such as the magnetic field and electric field, exhibit their unique merits in directional control. Therefore, combination of different motion mechanisms will facilitate the mainstream application of the m-bots. Third, the external field, such as magnetic field, electric field, and ultrasound field, generally possesses an effective working distance for the propulsion of the m-bots. Currently, the in vivo actuation and control of the m-bots based on these external fields work well as the animal models used are mainly that of small mammals like mice. However, m-bot-based therapy must ultimately be used for human beings who are much larger than the animals used as models. The external fields must have the capability for propelling and controlling the m-bots at the deep tissue level. Therefore, the scale-up of the therapy system based on m-bots should be improved.

8.4. Localization

The current medical image techniques are generally suitable for macroscale in vivo imaging as they have limited resolutions and imaging contrast. Therefore, the clinical imaging tools-based localization of m-bot swarms may be affordable whereas the in vivo localization of individual micro and nanoscale robots for precise surgery is still challenging.[407]

8.5. Applications

Although m-bots have been investigated extensively for various applications from the microscale manipulation and transportation of objects to biomedical applications such as in vitro and in vivo diagnosis, drug delivery, thrombus ablation, tissue reparation, and regeneration, these application related to the m-bots still lack of a "killer application" that can be only addressed by the m-bot technology.

The critical challenge for the bioapplication of autonomous and self-propelled m-bots is the use of nontoxic fuels. Although a few enzyme-catalysis-propelled m-bots have been developed based on nontoxic fuels such as urea, the field has a long way to go. Other types of novel enzyme-catalysis-propelled m-bots should be explored for certain particular in vivo applications. Another solution is substitution of the toxic fuels with external applied energies.

The influence of the navigation of m-bots caused by the complex in vivo fluidic environment should be addressed. As distinct from the macroscale objects in the fluidic environment, the motion in micro-/nanoscale is prominently weakened by the liquid viscosity and Brownian motion. In in vitro applications, the properties of the liquid environment such as mobility, viscosity, and pH can be artificially controlled to an optimized condition that is proper for the navigation and steering of the m-bots. Extra surfactant may be added to reduce the adhesion force between the surface and the m-bots to facilitate navigation control. However, the ideal fluidic environment is often inconsistent with the real in vivo environment, which is much more complex and contains many biomolecules that may react with the injected m-bots and show unspecific affinity. These unexpected phenomena may not only alter the motion forms and speed of the m-bots, but also result in failure of in vivo applications. Fischer et al.[408] have provided a good example for addressing this problem. Inspired by Helicobacter pylori, they functionalized helical microrobots with the enzyme urease that could locally raise the pH and consequently liquefy mucus to overcome the mucus barrier and actuate the microrobots. This case is only the tip of the iceberg, and biological barriers in the organism are ubiquitous. To realize the delivery of the m-bots in vivo, this aspect may require broad and profound investigation.

8.5.1. All-in-One Integration of Micro-/Nanomachines and Their Functionalization, Actuation, Localization, and In Vivo Applications

While impressive strides have been made in the development of various kinds of m-bots, especially in design and actuation, among the five aspects showed in Figure 1, the achievement of real biomedical applications may require further improvements in several other aspects such as functionalization, biocompatibility, localization, and systematization. To date, the harmonization of these aspects to realize the visualizable in vivo diagnosis and therapy with micro-/nanorobotic systems is extremely rare. We foresee that the bioapplication of the m-bots should not be limited to the simplified platforms under manual operations with poor integration of the actuation system and the localization system. For the future investigation, efforts should be paid in the design of the automated platforms[409,410] that integrate the multiple functions in complex biological systems and the actuation and control of the m-bots become more functionalized and self-regulated. It is worth noting that, several specific fields related to m-bots are still in the preliminary stages, such as the swarming and localization of m-bots and their application to thrombus ablation. These fields may require the further development before an integrated procedure can be developed for translation from lab to clinic.

Acknowledgements

The authors thank the comments and discussions with Prof. Z.G. Guo from Lanzhou Institute of Chemical Physics, CAS, and discussion with Prof. T.T. Xu from Shenzhen Institutes of Advanced Technology (SIAT), CAS. This work was partially supported by the Hong Kong RGC Joint Laboratory Funding Scheme (JLFS) with Project No. JLFS/E-402/18, the RGC Collaborative Research Fund (CRF) with Project No. C4063-18GF, the projects funded by the Hong Kong ITC with Project Numbers MRP/036/18X and ITS/374/18FP, the projects from CUHK internal grants, and the support from SIAT-CUHK Joint Laboratory of Robotics and Intelligent Systems. B.W. would like to thank the financial support from the Impact Postdoctoral Fellowship Scheme from the Chinese University of Hong Kong.

Conflict of Interest

The authors declare no conflict of interest.

Keywords

biomedical application, micro-/nanorobots, real-time imaging, swarm, targeted delivery

Received: March 24, 2020
Revised: August 24, 2020
Published online:

[1] a) B. J. Nelson, I. K. Kaliakatsos, J. J. Abbott, *Annu. Rev. Biomed. Eng.* **2010**, *12*, 55; b) E. W. H. Jager, O. Inganas, I. Lundstrom, *Science* **2000**, *288*, 2335.
[2] H. Ceylan, I. C. Yasa, U. Kilic, W. Hu, M. Sitti, *Prog. Biomed. Eng.* **2019**, *1*, 012002.
[3] M. Safdar, S. U. Khan, J. Janis, *Adv. Mater.* **2018**, *30*, 1703660.
[4] M. Medina-Sánchez, V. Magdanz, M. Guix, V. M. Fomin, O. G. Schmidt, *Adv. Funct. Mater.* **2018**, *28*, 1707228.
[5] J. Parmar, D. Vilela, K. Villa, J. Wang, S. Sańchez, *J. Am. Chem. Soc.* **2018**, *140*, 9317.
[6] J. Li, B. E. de Avila, W. Gao, L. Zhang, J. Wang, *Sci. Rob.* **2017**, *2*, eaam6431.
[7] a) B. Xu, B. Zhang, G. Huang, Y. Mei, *Adv. Funct. Mater.* **2018**, *28*, 1705872; b) W. Liu, X. Chen, X. Lu, J. Wang, Y. Zhang, Z. Gu, *Adv. Funct. Mater.* **2020**, *30*, 2003195.
[8] J. M. McCracken, B. R. Donovan, T. J. White, *Adv. Mater.* **2020**, *32*, 1906564.
[9] a) Z. Wu, Y. Chen, D. Mukasa, O. S. Pak, W. Gao, *Chem. Soc. Rev.* **2020**, https://doi.org/10.1039/d0cs00309c; b) H. Wang, M. Pumera, *Adv. Funct. Mater.* **2018**, *28*, 1705421.
[10] L. Sun, Y. Yu, Z. Chen, F. Bian, F. Ye, L. Sun, Y. Zhao, *Chem. Soc. Rev. 49*, 4043, **2020**.
[11] H. Ceylan, J. Giltinan, K. Kozielski, M. Sitti, *Lab Chip* **2017**, *17*, 1705.
[12] C. Gao, Z. Lin, X. K. Lin, Q. He, *Adv. Ther.* **2018**, *1*, 1800056.
[13] S. Campuzano, B. Esteban-Fernandez de Avila, P. Yanez-Sedeno, J. M. Pingarron, J. Wang, *Chem. Sci.* **2017**, *8*, 6750.
[14] R. D. Field, P. N. Anandakumaran, S. K. Sia, *Appl. Phys. Rev.* **2019**, *6*, 041305.
[15] S. M. Douglas, I. Bachelet, G. M. Church, *Science* **2012**, *335*, 831.
[16] Y.-J. Chen, B. Groves, R. A. Muscat, G. Seelig, *Nat. Nanotechnol.* **2015**, *10*, 748.
[17] S. P. Li, Q. Jiang, S. L. Liu, Y. L. Zhang, Y. H. Tian, C. Song, J. Wang, Y. G. Zou, G. J. Anderson, J.-Y. Han, Y. Chang, Y. Liu, C. Zhang, L. Chen, G. B. Zhou, G. J. Nie, H. Yan, B. Q. Ding, Y. L. Zhao, *Nat. Biotechnol.* **2018**, *36*, 264.
[18] Q. Jiang, S. Liu, J. Liu, Z. Wang, B. Ding, *Adv. Mater.* **2019**, *31*, 1804785.
[19] Y. Ji, X. Lin, H. Zhang, Y. Wu, J. Li, Q. He, *Angew. Chem., Int. Ed.* **2019**, *58*, 4184.
[20] M. Guix, S. M. Weiz, O. G. Schmidt, M. Medina-Sánchez, *Part. Part. Syst. Charact.* **2018**, *35*, 1700382.
[21] Z. Wu, X. Lin, T. Si, Q. He, *Small* **2016**, *12*, 3080.
[22] X. Zhao, K. Gentile, F. Mohajerani, A. Sen, *Acc. Chem. Res.* **2018**, *51*, 2373.
[23] T. Patiño, X. Arqué, R. Mestre, L. Palacios, S. Sánchez, *Acc. Chem. Res.* **2018**, *51*, 2662.
[24] S. Keller, B. J. Toebes, D. A. Wilson, *Biomacromolecules* **2019**, *20*, 1135.
[25] M. Sitti, D. S. Wiersma, *Adv. Mater.* **2020**, *32*, 1906766.
[26] T. Xu, W. Gao, L. Xu, X. Zhang, S. Wang, *Adv. Mater.* **2017**, *29*, 1603250.
[27] a) C. R. Chen, E. Karshalev, J. G. Guan, J. Wang, *Small* **2018**, *14*, 1704252; b) X. X. Le, W. Lu, J. W. Zhang, T. Chen, *Adv. Sci.* **2019**, *6*, 1801584; c) A. Barbot, H. Tan, M. Power, F. Seichepine, G.-Z. Yang, *Sci. Rob.* **2019**, *4*, eaax8336; d) S. Ghosh, A. Ghosh, *Sci. Rob.* **2018**, *3*, eaaq0076.
[28] a) L. Zhang, T. Petit, K. Peyer, B. Nelson, *Nanomedicine* **2012**, *8*, 1074; b) T. Petit, L. Zhang, K. Peyer, B. Kratochvil, B. Nelson, *Nano Lett.* **2012**, *12*, 156.
[29] S. K. Srivastava, M. Guix, O. G. Schmidt, *Nano Lett.* **2016**, *16*, 817.
[30] J. Orozco, G. Z. Cheng, D. Vilela, S. Sattayasamitsathit, R. Vazquez-Duhalt, G. ValdØs-Ramírez, O. S. Pak, A. Escarpa, C. Y. Kan, J. Wang, *Angew. Chem., Int. Ed.* **2013**, *52*, 13276.
[31] F. Z. Mou, D. Pan, C. R. Chen, Y. R. Cao, L. L. Xu, J. G. Guan, *Adv. Funct. Mater.* **2015**, *25*, 6173.
[32] E. Karshalev, B. E. de Ávila, J. Wang, *J. Am. Chem. Soc.* **2018**, *140*, 3810.
[33] W. J. Huang, M. Manjare, Y. P. Zhao, *J. Phys. Chem. C* **2013**, *117*, 21590.
[34] B. Jurado-Sáncheza, J. Wang, *Environ. Sci.: Nano* **2018**, *5*, 1530.
[35] J. X. Li, I. Rozen, J. Wang, *ACS Nano* **2016**, *10*, 5619.
[36] S. Palagi, P. Fischer, *Nat. Rev. Mater.* **2018**, *3*, 113.
[37] R. Maria-Hormigos, B. Jurado-Sánchez, A. Escarpa, *Lab Chip* **2016**, *16*, 2397.
[38] L. L. Xu, F. Z. Mou, H. T. Gong, M. Luo, J. G. Guan, *Chem. Soc. Rev.* **2017**, *46*, 6905.
[39] O. S. Wolfbeis, *Chem. Soc. Rev.* **2015**, *44*, 4743.
[40] C. Y. Wen, H. Xie, Z. Zhang, L. Wu, J. Hu, M. Tang, M. Wu, D. Pang, *Nanoscale* **2016**, *8*, 12406.
[41] J. J. Abbott, K. E. Peyer, M. C. Lagomarisino, L. Zhang, L. X. Dong, I. K. Kaliakatsos, B. J. Nelson, *Int. J. Rob. Res.* **2009**, *28*, 1434.
[42] a) M. Medina-Sanchez, O. Schmidt, *Nature* **2017**, *545*, 406; b) W. Wang, W. T. Duan, S. Ahmed, A. Sen, T. E. Mallouk, *Acc. Chem. Res.* **2015**, *48*, 1938.
[43] C. Gao, Y. Wang, Z. Ye, Z. Lin, X. Ma, Q. He, *Adv. Mater.* **2020**, *32*, 2000512.
[44] A. Servant, F. M. Qiu, M. Mazza, K. Kostarelos, B. J. Nelson, *Adv. Mater.* **2015**, *27*, 2981.
[45] S. Tottori, L. Zhang, F. Qiu, K. K. Krawczyk, A. Franco-Obregõn, B. J. Nelson, *Adv. Mater.* **2012**, *24*, 811.
[46] Z. G. Wu, X. K. Lin, Y. J. Wu, T. Y. Si, J. M. Sun, Q. He, *ACS Nano* **2014**, *8*, 6097.
[47] X.-Z. Chen, M. Hoop, N. Shamsudhin, T. Y. Huang, B. Ozkale, Q. Li, E. Siringil, F. Mushtaq, L. D. Tizio, B. J. Nelson, S. Pan, *Adv. Mater.* **2017**, *29*, 1605458.
[48] S. Fournier-Bidoz, A. C. Arsenault, I. Manners, G. a. Ozin, *Chem. Commun.* **2005**, *4*, 441.
[49] R. Dong, Q. Zhang, W. Gao, A. Pei, B. Ren, *ACS Nano* **2016**, *10*, 839.
[50] L. F. Valadares, Y. G. Tao, N. S. Zacharia, V. Kitaev, F. Galembeck, R. Kapral, G. a. Ozin, *Small* **2010**, *6*, 565.
[51] W. Z. Teo, H. Wang, M. Pumera, *Chem. Commun.* **2016**, *52*, 4333.
[52] V. V. Singh, B. Jurado-Sánchez, S. Sattayasamitsathit, J. Orozco, J. Li, M. Galarnyk, Y. Fedorak J. Wang, *Adv. Funct. Mater.* **2015**, *25*, 2147.
[53] T. Li, J. Li, H. Zhang, X. Chang, W. Song, Y. Hu, G. Shao, E. Sandraz, G. Zhang, L. Li, J. Wang, *Small* **2016**, *12*, 6098.
[54] T. G. Leong, C. L. Randall, B. R. Benson, N. Bassik, G. M. Stern, D. H. Gracias, *Proc. Natl. Acad. Sci. USA* **2009**, *106*, 703.
[55] F. Z. Mou, C. R. Chen, Q. Zhong, Y. X. Yin, H. R. Ma, J. G. Guan, *ACS Appl. Mater. Interfaces* **2014**, *6*, 9897.
[56] B. Jurado-Sanchez, A. Escarpa, J. Wang, *Chem. Commun.* **2015**, *51*, 14088.
[57] S. Balasubramanian, D. Kagan, C.-M. Jack Hu, S. Campuzano, M. J. Lobo-Castanon, N. Lim, D. Y. Kang, M. Zimmerman, L. Zhang, J. Wang, *Angew. Chem., Int. Ed.* **2011**, *50*, 4161.
[58] D. L. Fan, Z. Z. Yin, R. Cheung, F. Q. Zhu, A. Levchenko, R. C. Cammarata, C. L. Chien, A. Levchenko, *Nat. Nanotechnol.* **2010**, *5*, 545.

[59] N. Hu, M. M. Sun, X. K. Lin, C. Y. Gao, H. Xie, B. Zhang, C. Zheng, Q. He, *Adv. Funct. Mater.* **2018**, *28*, 1705684.
[60] D. Kagan, M. J. Benchimol, J. C. Claussen, E. Chuluun-Erdene, S. Esener, J. Wang, *Angew. Chem., Int. Ed.* **2012**, *51*, 7519.
[61] Z. Wu, T. Si, W. Gao, X. Lin, J. Wang, Q. He, *Small* **2016**, *12*, 577.
[62] F. C. Meng, W. Hao, S. T. Yu, R. Feng, Y. M. Liu, F. Yu, P. Tao, W. Shang, J. B. Wu, C. Y. Song, T. Deng, *J. Am. Chem. Soc.* **2017**, *139*, 12362.
[63] J. Vialetto, M. Hayakawa, N. Kavokine, M. Takinoue, S. N. Varanakkottu, S. Rudiuk, M. Anyfantakis, M. Morel, D. Baigl, *Angew. Chem., Int. Ed.* **2017**, *56*, 16565.
[64] X. Yan, Q. Zhou, M. Vincent, Y. Deng, J. Yu, J. Xu, T. Xu, T. Tang, L. Bian, Y. Wang, K. Kostarelos, L. Zhang, *Sci. Rob.* **2017**, *2*, eaaq1155.
[65] S. Wen, L. Zhao, Q. Zhao, C. Liu, Z. Yu, M. Shen, J. Majoral, S. Mignani, J. Zhao, X. Shi, *J. Mater. Chem. B* **2017**, *5*, 3810.
[66] S. Kesner, R. D. Howe, *Int. J. Rob. Res.* **2014**, *33*, 631.
[67] D. Vilela, U. Cossío, J. Parmar, A. M. Martínez-Villacorta, V. Gómez-Vallejo, J. Llop, S. Sánchez, *ACS Nano* **2018**, *12*, 1220.
[68] H. Hong, F. Wang, Y. Zhang, S. A. Graves, S. B. Z. Eddine, Y. Yang, C. P. Theuer, R. J. Nickles, X. Wang, W. Cai, *ACS Appl. Mater. Interfaces* **2015**, *7*, 3373.
[69] D. Karnaushenko, T. Kang, V. K. Bandari, F. Zhu, O. G. Schmidt, *Adv. Mater.* **2020**, *32*, 1902994.
[70] J. X. Shao, M. J. Xuan, L. R. Dai, T. Y. Si, J. B. Li, Q. He, *Angew. Chem., Int. Ed.* **2015**, *54*, 12782.
[71] W. Gao, J. Wang, *ACS Nano* **2014**, *8*, 3170.
[72] L. Zhang, J. J. Abbott, L. Dong, B. E. Kratochvil, D. Bell, B. J. Nelson, *Appl. Phys. Lett.* **2009**, *94*, 064107.
[73] I. S. Khalil, H. C. Dijkslag, L. Abelmann, S. Misra, *Appl. Phys. Lett.* **2014**, *104*, 223701.
[74] A. A. Solovev, Y. F. Mei, E. B. Urena, G. S. Huang, O. G. Schmidt, *Small* **2009**, *5*, 1688.
[75] S. Sanchez, A. N. Ananth, V. M. Fomin, M. Viehrig, O. G. Schmidt, *J. Am. Chem. Soc.* **2011**, *133*, 14860.
[76] M. Liu, L. Liu, W. Gao, M. Su, Y. Ge, L. Shi, H. Zhang, B. Dong, C. Y. Li, *Nanoscale* **2014**, *6*, 8601.
[77] M. Safdar, T. Do Minh, N. Kinnunen, J. Janis, *ACS Appl. Mater. Interfaces* **2016**, *8*, 32624.
[78] W. Gao, R. Dong, S. Thamphiwatana, J. Li, W. Gao, L. Zhang, J. Wang, *ACS Nano* **2015**, *9*, 117.
[79] C. Chen, E. Karshalev, J. Li, F. Soto, R. Castillo, I. Campos, F. Mou, J. Guan, J. Wang, *ACS Nano* **2016**, *10*, 10389.
[80] J. Li, V. V. Singh, S. Sattayasamitsathit, J. Orozco, K. Kaufmann, R. Dong, W. Gao, B. Jurado-sanchez, Y. Fedorak, J. Wang, *ACS Nano* **2014**, *8*, 11118.
[81] J. Li, S. Thamphiwatana, W. Liu, B. Esteban-Fernandez De Avila, P. Angsantikul, E. Sandraz, J. Wang, T. Xu, F. Soto, V. Ramez, X. Wang, W. Gao, L. Zhang, J. Wang, *ACS Nano* **2016**, *10*, 9536.
[82] W. Gao, A. Pei, R. Dong, J. Wang, *J. Am. Chem. Soc.* **2014**, *136*, 2276.
[83] W. Z. Teo, R. Zboril, I. Medrik, M. Pumera, *Chem. - Eur. J.* **2016**, *22*, 4789.
[84] X. Ma, A. Jannasch, U. R. Albrecht, K. Hahn, A. Miguel-Lopez, E. Schaffer, S. Sanchez, *Nano Lett.* **2015**, *15*, 7043.
[85] B. Dai, J. Wang, Z. Xiong, X. Zhan, W. Dai, C.-C. Li, S.-P. Feng, J. Tang, *Nat. Nanotechnol.* **2016**, *11*, 1087.
[86] D. P. Singh, U. Choudhury, P. Fischer, A. G. Mark, *Adv. Mater.* **2017**, *29*, 1701328.
[87] R. Dreyfus, J. Baudry, M. L. Roper, M. Fermigier, H. A. Stone, J. Bibette, *Nature* **2005**, *437*, 862.
[88] W. Hu, G. Z. Lum, M. Mastrangeli, M. Sitti, *Nature* **2018**, *554*, 81.
[89] J. Cui, T. Huang, Z. Luo, P. Testa, H. Gu, X. Chen, B. Nelson, L. J. Heyderman, *Nature* **2019**, *575*, 164.
[90] a) Y. Wu, J. K. Yim, J. M. Liang, Z. C. Shao, M. J. Qi, J. W. Zhong, Z. H. Luo, X. J. Yan, M. Zhang, X. H. Wang, R. S. Fearing, R. J. Full, L. W. Lin, *Sci. Rob.* **2019**, *4*, eaax1594; b) Y. Kim, G. A. Parada, S. Liu, X. Zhao, *Sci. Rob.* **2019**, *4*, eaax7329.
[91] X. Du, H. Cui, T. Xu, C. Huang, Y. Wang, Q. Zhao, Y. Xu, X. Wu, *Adv. Funct. Mater.* **2020**, *30*, 1909202.
[92] X. Fan, M. Sun, L. Sun, H. Xie, *Adv. Funct. Mater.* **2020**, *30*, 2000138.
[93] X. Wang, X. Qin, C. Hu, A. Terzopoulou, X. Chen, T. Huang, K. Maniura-Weber, S. Pane, B. J. Nelson, *Adv. Funct. Mater.* **2018**, *28*, 1804107.
[94] H. Huang, T. Huang, M. Charilaou, S. Lyttle, Q. Zhang, S. Pane, B. J. Nelson, *Adv. Funct. Mater.* **2018**, *28*, 1802110.
[95] a) Y. Jian, B. Wu, X. Le, Y. Liang, Y. Zhang, D. Zhang, L. Zhang, W. Lu, J. Zhang, T. Chen, *Research* **2019**, *2019*, 2384347; b) X. Zhou, T. Li, J. Wang, F. Chen, D. Zhou, Q. Liu, B. Li, J. Cheng, X. Zhou, B. Zheng, *ACS Appl. Mater. Interfaces* **2018**, *10*, 9077.
[96] X. Du, H. Cui, Q. Zhao, J. Wang, H. Chen, Y. Wang, *Research* **2019**, *2019*, 6398296.
[97] a) C. Appiah, C. Arndt, K. Siemsen, A. Heitmann, A. Staubitz, C. Selhuber-Unkel, *Adv. Mater.* **2019**, *31*, 1807747; b) H. Wang, M. Totaro, L. Beccai, *Adv. Sci.* **2018**, *5*, 1800541; c) L. Zhu, B. Wang, S. Handschuh-Wang, X. Zhou, *Small* **2020**, *16*, 1903841; d) Y. Chen, T. Zhou, Y. Li, L. Zhu, S. Handschuh-Wang, D. Zhu, X. Zhou, T. Gan, X. Zhou, *Adv. Funct. Mater.* **2018**, *28*, 1706277.
[98] a) M. Liu, Y. Wang, Y. Kuai, J. Cong, Y. Xu, H.-G. Piao, L. Pan, Y. Liu, *Small* **2019**, *15*, 1905446; b) T. S. Gan, W. H. Shang, S. Handschuh-Wang, X. C. Zhou, *Small* **2019**, *15*, 1804838; c) S. Keller, G. X. Hu, M. I. Gherghina-Tudor, S. P. Teora, D. A. Wilson, *Adv. Funct. Mater.* **2019**, *29*, 1904889.
[99] C. Z. Hu, S. Pane, B. J. Nelson, *Annu. Rev. Control Rob. Auton. Syst.* **2018**, *1*, 53.
[100] W. Gao, S. Sattayasamitsathit, K. M. Manesh, D. Weihs, J. Wang, *J. Am. Chem. Soc.* **2010**, *132*, 14403.
[101] T. Xu, J. Zhang, M. Salehizadeh, O. Onaizah, E. Diller, *Sci. Rob.* **2019**, *4*, eaav4494.
[102] T. Li, J. Li, K. I. Morozov, Z. Wu, T. Xu, I. Rozen, A. M. Leshansky, L. Li, J. Wang, *Nano Lett.* **2017**, *17*, 5092.
[103] V. M. Kadiri, C. Bussi, A. W. Holle, K. Son, H. Kwon, G. Schütz, M. G. Gutierrez, P. Fischer, *Adv. Mater.* **2020**, *32*, 2001114.
[104] X. P. Wang, X.-H. Qin, C. Z. Hu, A. Terzopoulou, X.-Z. Chen, T.-Y. Huang, K. Maniur-Weber, S. Pané, B. J. Nelson, *Adv. Funct. Mater.* **2018**, *28*, 1804107.
[105] R. Yang, T. Wei, H. Goldberg, W. Wang, K. Cullion, D. S. Kohane, *Adv. Mater.* **2017**, *29*, 1606596.
[106] M. A. Dobrovolskaia, P. Aggarwal, J. B. Hall, S. E. McNeil, *Mol. Pharmaceutics* **2008**, *5*, 487.
[107] J. N. Hu, S. Huang, L. Zhu, W. J. Huang, Y. P. Zhao, K. L. Jin, Q. C. ZhuGe, *ACS Appl. Mater. Interfaces* **2018**, *10*, 32988.
[108] F. Novotny, H. Wang, M. Pumera, *Chem* **2020**, *6*, 867.
[109] L. Zhang, J. J. Abbott, L. X. Dong, K. E. Peyer, B. E. Kratochvil, H. X. Zhang, C. Bergeles, B. J. Nelson, *Nano Lett.* **2009**, *9*, 3663.
[110] H. Zeng, P. Wasylczyk, C. Parmeggiani, D. Martella, M. Burresi, D. S. Wiersma, *Adv. Mater.* **2015**, *27*, 3883.
[111] S. Kim, F. Qiu, S. Kim, A. Ghanbari, C. Moon, L. Zhang, B. J. Nelson, H. Choi, *Adv. Mater.* **2013**, *25*, 5863.
[112] L. Q. Ren, D. K. Zhou, Z. M. Mao, P. T. Xu, T. J. Huang, T. E. Mallouk, *ACS Nano* **2017**, *11*, 10591.
[113] J. G. Gibbs, S. Kothari, D. Saintillan, Y.-P. Zhao, *Nano Lett.* **2011**, *11*, 2543.
[114] M. Xuan, R. Mestre, C. Y. Gao, C. Zhou, Q. He, S. Sanchez, *Angew. Chem., Int. Ed.* **2018**, *57*, 6838.
[115] Z. Wu, J. Li, B. E. de Ávila, T. Li, W. Gao, Q. He, L. Zhang, J. Wang, *Adv. Funct. Mater.* **2015**, *25*, 7497.

[116] J. Li, X. Li, T. Luo, R. Wang, C. Liu, S. Chen, D. Li, J. Yue, S. Cheng, D. Sun, *Sci. Rob.* **2018**, *3*, eaat8829.
[117] Q. Rao, T. Si, Z. Wu, M. Xuan, Q. He, *Sci. Rep.* **2017**, *7*, 4621.
[118] T. Y. Huang, M. S. Sakar, A. Mao, A. J. Petruska, F. Qiu, X. B. Chen, S. Kennedy, D. Mooney, B. J. Nelson, *Adv. Mater.* **2015**, *27*, 6644.
[119] E. B. Steager, M. S. Sakar, C. Magee, M. Kennedy, A. Cowley, V. Kumar, *Int. J. Rob. Res.* **2013**, *32*, 346.
[120] J. Palacci, S. Sacanna, A. Vatchinsky, P. M. Chaikin, D. J. Pine, *J. Am. Chem. Soc.* **2013**, *135*, 15978.
[121] E. Diller, M. Sitti, *Adv. Funct. Mater.* **2014**, *24*, 4397.
[122] H. W. Huang, M. S. Sakar, A. J. Petruska, S. Pane, B. J. Nelson, *Nat. Commun.* **2016**, *7*, 12263.
[123] D. Vilela, J. Orozco, G. Cheng, S. Sattayasamitsathit, M. Galarnyk, C. Kanwie, J. Wang, A. Escarpa, *Lab Chip* **2014**, *14*, 3505.
[124] B. E. de Ávila, M. A. Lopez-Ramirez, D. F. Báez, A. Jodra, V. V. Singh, K. Kaufmann, J. Wang, *ACS Sens.* **2016**, *1*, 217.
[125] M. Kiristi, V. V. Singh, B. E. de Avila, M. Uygun, F. Soto, D. A. Uygun, J. Wang, *ACS Nano* **2015**, *9*, 9252.
[126] S. Campuzano, J. Orozco, D. Kagan, M. Guix, W. Gao, S. Sattayasamitsathit, J. C. Claussen, A. Merkoçi, J. Wang, *Nano Lett.* **2012**, *12*, 396.
[127] C. J. Hu, L. Zhang, S. Aryal, C. Cheung, R. H. Fang, L. Zhang, *Proc. Natl. Acad. Sci. USA* **2011**, *108*, 10980.
[128] H. Yan, D. Shao, Y. Lao, M. Li, H. Hu, K. W. Leong, *Adv. Sci.* **2019**, *6*, 1900605.
[129] C. J. Hu, R. H. Fang, J. Copp, B. T. Luk, L. Zhang, *Nat. Nanotechnol.* **2013**, *8*, 336.
[130] Z. G. Wu, T. L. Li, J. X. Li, W. Gao, T. L. Xu, C. Christianson, W. W. Gao, M. Galarnyk, Q. He, L. F. Zhang, J. Wang, *ACS Nano* **2014**, *8*, 12041.
[131] I. C. Yasa, H. Ceylan, U. Bozuyuk, A. Wild, M. Sitti, *Sci. Rob.* **2020**, *5*, eaaz3867.
[132] M. Wan, Q. Wang, R. Wang, R. Wu, T. Li, D. Fang, Y. Huang, Y. Yu, L. Fang, X. Wang, Y. Zhang, Z. Miao, B. Zhao, F. Wang, C. Mao, Q. Jiang, X. Xu, D. Shi, *Sci. Adv.* **2020**, *6*, eaaz9014.
[133] J. Shao, M. Xuan, H. Zhang, X. Lin, Z. Wu, Q. He, *Angew. Chem. Int. Ed.* **2017**, *56*, 12935.
[134] F. Kuralay, S. Sattayasamitsathit, W. Gao, A. Uygun, A. Katzenberg, J. Wang, *J. Am. Chem. Soc.* **2012**, *134*, 15217.
[135] A. M. Maier, C. Weig, P. Oswald, E. Frey, P. Fischer, T. Liedl, *Nano Lett.* **2016**, *16*, 906.
[136] B. Wang, Y. Liu, Y. B. Zhang, Z. G. Guo, H. Zhang, J. H. Xin, L. Zhang, *Adv. Mater. Interfaces* **2015**, *2*, 1500234.
[137] K. E. Peyer, L. Zhang, B. J. Nelson, *Nanoscale* **2013**, *5*, 1259.
[138] T. L. Li, A. N. Zhang, G. B. Shao, M. Wei, B. Guo, G. Y. Zhang, L. Q. Li, W. Wang, *Adv. Funct. Mater.* **2018**, *28*, 1706066.
[139] M. Suter, O. Ergeneman, J. Zuecher, S. Schmid, A. Camenzind, B. Nelson, C. Hierold, *J. Micromech. Microeng.* **2011**, *21*, 025023.
[140] L. Yang, X. Chen, L. Wang, Z. Hu, C. Xin, M. Hippler, W. Zhu, Y. Hu, J. Li, Y. Wang, L. Zhang, D. Wu, J. Chu, *Adv. Funct. Mater.* **2019**, *29*, 1905745.
[141] A. M. Leshansky, K. I. Morozova, B. Y. Rubinstein, *Nanoscale* **2016**, *8*, 14127.
[142] K. I. Morozov, A. M. Leshansky, *Nanoscale* **2014**, *6*, 12142.
[143] L. Zhang, E. Ruh, D. Grützmacher, L. X. Dong, D. J. Bell, B. J. Nelson, C. Schönenberger, *Nano Lett.* **2006**, *6*, 1311.
[144] A. Ghosh, P. Fischer, *Nano Lett.* **2009**, *9*, 2243.
[145] D. Walker, M. Kübler, K. I. Morozov, P. Fischer, A. M. Leshansky, *Nano Lett.* **2015**, *15*, 4412.
[146] D. Schamel, A. G. Mark, J. G. Gibbs, C. Miksch, K. I. Morozov, A. M. Leshansky, P. Ficher, *ACS Nano* **2014**, *8*, 8794.
[147] P. L. Venugopalan, S. Jain, S. Shivashankar, A. Ghosh, *Nanoscale* **2018**, *10*, 2327.
[148] D. F. Li, Y. T. Liu, Y. Y. Yang, Y. J. Shen, *Nanoscale* **2018**, *10*, 19673.
[149] M. Suter, L. Zhang, E. C. Siringil, C. Peters, T. Luehmann, O. Ergeneman, K. E. Peyer, B. J. Nelson, C. Hierold, *Biomed. Microdevices* **2013**, *15*, 997.
[150] C. Peters, O. Ergeneman, P. D. W. Garcia, M. Muller, S. Pane, B. J. Nelson, C. Hierold, *Adv. Funct. Mater.* **2014**, *24*, 5269.
[151] A. Ghosh, D. Dasgupta, M. Pal, K. I. Morozov, A. M. Leshansky, A. Ghosh, *Adv. Funct. Mater.* **2018**, *28*, 1705687.
[152] J. Li, S. Sattayasamitsathit, R. Dong, W. Gao, R. Tam, X. Feng, S. Ai, J. Wang, *Nanoscale* **2014**, *6*, 9415.
[153] L. Liu, S. H. Yoo, S. A. Lee, S. Park, *Nano Lett.* **2011**, *11*, 3979.
[154] W. Gao, X. Feng, A. Pei, C. R. Kane, R. Tam, C. Hennessy, J. Wang, *Nano Lett.* **2014**, *14*, 305.
[155] X. H. Yan, Q. Zhou, J. F. Yu, T. T. Xu, Y. Deng, T. Tang, Q. Feng, L. M. Bian, Y. Zhang, A. Ferreira, L. Zhang, *Adv. Funct. Mater.* **2015**, *25*, 5333.
[156] D. Zhong, W. Li, Y. Qi, J. He, M. Zhou, *Adv. Funct. Mater.* **2020**, *30*, 1910395.
[157] Y. R. Yu, L. R. Shang, W. Gao, Z. Zhao, H. Wang, Y. J. Zhao, *Angew. Chem., Int. Ed.* **2017**, *56*, 12127.
[158] U. K. Cheang, F. Meshkati, D. Kim, M. J. Kim, H. C. Fu, *Phys. Rev. E* **2014**, *90*, 033007.
[159] K. Han, C. W. Shields IV, N. M. Diwakar, B. Bharti, G. P. López, O. D. Velev, *Sci. Adv.* **2017**, *3*, e1701108.
[160] a) Y. Wang, Y. Liu, Y. Li, D. Xu, X. Pan, Y. Chen, D. Zhou, B. Wang, H. Feng, X. Ma, *Research* **2020**, *2020*, 7962024. b) Q. Wang, L. Yang, J. Yu, L. Zhang, *Rob. Biomim.* **2017**, *4*, 20.
[161] K. I. Morozov, Y. Mirzae, O. Kenneth, A. Leshansky, *Phys. Rev. Fluids* **2017**, *2*, 044202.
[162] S. Tottori, B. J. Nelson, *Small* **2018**, *14*, 1800722.
[163] G. Boussinot, M. Apel, J. Zielinski, U. Hecht, J. H. Schleifenbaum, *Phys. Rev. Appl.* **2019**, *11*, 014025.
[164] P. J. Vach, P. Fratzl, S. Klumpp, D. Faivre, *Nano Lett.* **2015**, *15*, 7064.
[165] P. J. Vach, N. Brun, M. Bennet, L. Bertinetti, M. Widdrat, J. Baumgartner, S. Klumpp, P. Fratzl, D. Faivre, *Nano Lett.* **2013**, *13*, 5373.
[166] Y. Mirzae, O. Dubrovski, O. Kenneth, K. I. Morozov, A. M. Leshansky, *Sci. Rob.* **2018**, *3*, eaas8713.
[167] C. H. Bi, M. Guix, B. V. Johnson, W. M. Jing, D. J. Cappelleri, *Micromachines* **2018**, *9*, 68.
[168] a) T. L. Xu, L.-P. Xu, X. J. Zhang, *Appl. Mater. Today* **2017**, *9*, 493; b) S. Ahmed, W. Wang, L. J. Bai, D. T. Gentekos, M. Hoyos, T. E. Mallouk, *ACS Nano* **2016**, *10*, 4763.
[169] W. Wang, L. A. Castro, M. Hoyos, T. E. Mallouk, *ACS Nano* **2012**, *6*, 6122.
[170] T. Xu, F. Soto, W. Gao, V. Garcia-Gradilla, J. Li, X. Zhang, J. Wang, *J. Am. Chem. Soc.* **2014**, *136*, 8552.
[171] D. Ahmed, T. Baasch, B. Jang, S. Pane, J. Dual, B. J. Nelson, *Nano Lett.* **2016**, *16*, 4968.
[172] C. Zhou, L. Zhao, M. Wie, W. Wang, *ACS Nano* **2017**, *11*, 12668.
[173] K. J. Rao, F. Li, L. Meng, H. Zheng, F. Cai, W. Wang, *Small* **2015**, *11*, 2836.
[174] A. L. Balk, L. O. Mair, P. P. Mathai, P. N. Patrone, W. Wang, S. Ahmed, T. Mallouk, J. A. Liddle, S. M. Stavis, *ACS Nano* **2014**, *8*, 8300.
[175] T. Ren, P. Chen, L. Gu, M. G. Ogut, U. Demirci, *Adv. Mater.* **2020**, *32*, 1905713.
[176] F. Soto, A. Martin, S. Ibsen, M. Vaidyanathan, V. Garcia-Gradilla, Y. Levin, A. Escarpa, S. C. Esener, J. Wang, *ACS Nano* **2016**, *10*, 1522.
[177] M. Safdar, J. Simmchen, J. Jänis, *Environ. Sci.: Nano* **2017**, *4*, 1602.
[178] a) U. Choudhury, D. P. Singh, T. Qiu, P. Fisher, *Adv. Mater.* **2019**, *31*, 1807382; b) X. Zhan, J. Zheng, Y. Zhao, B. Zhu, R. Cheng, J. Wang, J. Liu, J. Tang, J. Tang, *Adv. Mater.* **2019**, *31*, 1903329; c) J. Zheng, J. Wang, Z. Xiong, Z. Wan, X. Zhan, S. Yang, J. Chen,

J. Dai, J. Tang, *Adv. Funct. Mater.* **2019**, *29*, 1901768; d) Z. Zhan, F. Wie, J. Zheng, C. Yin, W. Yang, L. Yao, S. Tang, D. Liu, *Mater. Lett.* **2020**, *258*, 126825.
[179] X.-Z. Chen, B. J. Jang, D. Ahmed, C. Z. Hu, C. D. Marco, M. Hoop, F. Mushtaq, B. J. Nelson, S. Pané, *Adv. Mater.* **2018**, *30*, 1705061.
[180] H. Eskandarloo, A. Kierulf, A. Abbaspourrad, *Nanoscale* **2017**, *9*, 12218.
[181] L. Shao, M. Käll, *Adv. Funct. Mater.* **2018**, *28*, 1706272.
[182] H. Kim, J.-H. Kang, Y. Zhou, A. S. Suenstler, Y. Kim, C. Chen, T. Emrick, R. C. Hayward, *Adv. Mater.* **2019**, *31*, 1900932.
[183] B. Jurado-Sánchez, M. Pacheco, R. Maria-Hormigos, A. Escarpa, *Appl. Mater. Today* **2017**, *9*, 407.
[184] B. Jang, A. Hong, H. E. Kang, C. Alcantara, S. Charreyron, F. Mushtaq, E. Pellicer, R. Büchel, J. Sort, S. S. Lee, B. J. Nelson, S. Pané, *ACS Nano* **2017**, *11*, 6146.
[185] Q. Zhang, R. F. Dong, Y. F. Wu, W. Gao, Z. H. He, B. Y. Ren, *ACS Appl. Mater. Interfaces* **2017**, *9*, 4674.
[186] D. K. Zhou, Y. C. Li, P. T. Xu, N. S. McCool, L. Q. Li, W. Wang, T. E. Mallouk, *Nanoscale* **2017**, *9*, 75.
[187] Z. R. Ye, Y. Y. Sun, H. Zhang, B. Song, B. Dong, *Nanoscale* **2017**, *9*, 18516.
[188] V. Sridhar, B.-W. Park, M. Sitti, *Adv. Funct. Mater.* **2018**, *28*, 1704902.
[189] D. K. Zhou, Y. C. Li, P. T. Xu, L. Q. Ren, G. Y. Zhang, T. E. Mallouk, L. Q. Li, *Nanoscale* **2017**, *9*, 11434.
[190] W. F. Paxton, K. C. Kistler, C. C. Olmeda, A. Sen, S. K. St. Angelo, Y. Cao, T. E. Mallouk, P. E. Lammert, V. H. Crespi, *J. Am. Chem. Soc.* **2004**, *126*, 13424.
[191] Y. Wang, C. Zhou, W. Wang, D. Xu, F. Zeng, C. Zhan, J. Gu, M. Li, W. Zhao, J. Zhang, J. Guo, H. Feng, X. Ma, *Angew. Chem., Int. Ed.* **2018**, *57*, 13110.
[192] R. F. Dong, Y. Hu, Y. F. Wu, W. Gao, B. Y. Ren, Q. L. Wang, Y. P. Cai, *J. Am. Chem. Soc.* **2017**, *139*, 1722.
[193] F. Z. Mou, Y. Li, C. R. Chen, W. Li, Y. X. Yin, H. R. Ma, J. G. Guan, *Adv. Funct. Mater.* **2018**, *28*, 1705867.
[194] W. Gao, A. Pei, J. Wang, *ACS Nano* **2012**, *6*, 8432.
[195] Y. F. Tu, F. Oeng, J. M. Heuvelmans, S. W. Liu, R. J. M. Nolte, D. A. Wilson, *Angew. Chem., Int. Ed.* **2019**, *58*, 8687.
[196] a) M. Pacheco, B. Jurado-Sánchez, A. Escarpa, *Chem. Sci.* **2018**, *9*, 8056; b) W. Qin, T. Peng, Y. Gao, F. Wang, X. Hu, K. Wang, J. Shi, D. Li, J. Ren, C. Fan, *Angew. Chem., Int. Ed.* **2017**, *56*, 515.
[197] A. Nourhani, E. Karshalev, F. Soto, J. Wang, *Research* **2020**, *2020*, 7823615.
[198] S. Sengupta, M. E. Ibele, A. Sen, *Angew. Chem., Int. Ed.* **2012**, *51*, 8434.
[199] Y. Wang, W. Duan, C. Zhou, Q. Liu, J. Gu, H. Ye, M. Li, W. Wang, X. Ma, *Adv. Mater.* **2019**, *31*, 1905067.
[200] X. M. Feng, Y. Zhang, Y. Li, Z. D. Huang, S. F. Chen, Y. W. Ma, L. Zhang, L. H. Wang, X. H. Yan, *Chem. Lett.* **2015**, *44*, 399.
[201] B. Jurado-Sánchez, S. Sattayasamitsathit, W. Gao, L. Santos, Y. Fedorak, V. V. Singh, J. Orozco, M. Galarnyk, J. Wang, *Small* **2015**, *11*, 499.
[202] J. Orozco, L. A. Mercante, R. Pol, A. Merkoçi, *J. Mater. Chem. A* **2016**, *4*, 3371.
[203] L. Soler, V. Magdanz, V. M. Fomin, S. Sanchez, O. G. Schmidt, *ACS Nano* **2013**, *7*, 9611.
[204] H. Wang, G. J. Zhao, M. Pumera, *J. Am. Chem. Soc.* **2014**, *136*, 2719.
[205] R. Maria-Hormigos, B. Jurado-Sanchez, L. Vazquez, A. Escarpa, *Chem. Mater.* **2016**, *28*, 8962.
[206] B. Jurado-Sánchez, J. Wang, A. Escarpa, *ACS Appl. Mater. Interfaces* **2016**, *8*, 19618.
[207] J.-Z. Jiang, L.-Q. Ren, Y.-P. Huang, X.-D. Li, S.-H. Wu, J.-J. Sun, *Adv. Mater. Interfaces* **2018**, *5*, 1701689.
[208] J. X. Li, X. Yu, M. L. Xu, W. J. Liu, E. Sandraz, H. Lan, J. Wang, S. M. Cohen, *J. Am. Chem. Soc.* **2017**, *139*, 611.
[209] H. Ye, J. Kang, G. F. Ma, H. Q. Sun, S. B. Wang, *J. Colloid Interface Sci.* **2018**, *528*, 271.
[210] J. G. S. Moo, C. C. Mayorga-Martinez, H. Wang, W. Z. Teo, B. H. Tan, T. D. Luong, S. R. Gonzalez-Avila, C.-D. Ohl, M. Pumera, *Adv. Funct. Mater.* **2018**, *28*, 1702618.
[211] J. Sun, Y. Q. Fu, R. Li, W. Feng, *Chem. Mater.* **2018**, *30*, 1625.
[212] G. Gallino, F. Gallaire, E. Lauga, S. Michelin, *Adv. Funct. Mater.* **2018**, *28*, 1800686.
[213] T. Maric, C. C. Mayorga-Martinez, B. Khezri, M. Z. M. Nasir, X. Chia, M. Pumera, *Adv. Funct. Mater.* **2018**, *28*, 1802762.
[214] H. Ye, G. F. Ma, J. Kang, H. Q. Sun, S. B. Wang, *Chem. Commun.* **2018**, *54*, 4653.
[215] K. K. Dey, X. Zhao, B. M. Tansi, W. J. Méndez-Ortiz, U. M. Córdova-Figueroa, R. Golestanian, A. Sen, *Nano Lett.* **2015**, *15*, 8311.
[216] L. K. E. A. Abdelmohsen, M. Nijemeisland, G. M. Pawar, G. A. Janssen, R. J. M. Nolte, J. C. M. van Hest, D. A. Wilson, *ACS Nano* **2016**, *10*, 2652.
[217] T. Patina, A. Porchetta, A. Jannasch, A. Llado, T. Stumpp, E. Schaffer, F. Ricci, S. Sanchez, *Nano Lett.* **2019**, *19*, 3440.
[218] F. M. Mazar, J. G. Martinez, M. Tyagi, M. Alijanianzadeh, A. P. F. Turner, E. W. H. Jager, *Adv. Mater.* **2019**, *31*, 1901677.
[219] T. Patiño, N. Feiner-Gracia, X. Arqué, A. Miguel-López, A. Jannasch, T. Stumpp, E. Schäffer, L. Albertazzi, S. Sánchez, *J. Am. Chem. Soc.* **2018**, *140*, 7896.
[220] D. Pantarotto, W. R. Browne, B. L. Feringa, *Chem. Commun.* **2008**, *10*, 1533.
[221] S. Sanchez, A. A. Solovev, Y. Mei, O. G. Schmidt, *J. Am. Chem. Soc.* **2010**, *132*, 13144.
[222] J. Orozco, V. García-Gradilla, M. D'Agostino, W. Gao, A. Cortés, J. Wang, *ACS Nano* **2013**, *7*, 818.
[223] X. Ma, A. C. Hortelao, A. Miguel-Lopez, S. Sanchez, *J. Am. Chem. Soc.* **2016**, *138*, 13782.
[224] M. Wan, H. Chen, Q. Wang, Q. Niu, P. Xu, Y. Yu, T. Zhu, C. Mao, J. Shen, *Nat. Commun.* **2019**, *10*, 966.
[225] L. K. E. A. Abdelmohsen, F. Peng, Y. F. Tu, D. A. Wilson, *J. Mater. Chem. B* **2014**, *2*, 2395.
[226] D. L. Fan, F. Q. Zhu, R. C. Cammarata, C. L. Chien, *Phys. Rev. Lett.* **2005**, *94*, 247208.
[227] K. Han, C. W. Shields, O. D. Velev, *Adv. Funct. Mater.* **2018**, *28*, 1705953.
[228] O. D. Velev, B. G. Prevo, K. H. Bhatt, *Nature* **2003**, *426*, 515.
[229] P. Calvo-Marzal, S. Sattayasamitsathit, S. Balasubramanian, J. R. Windmiller, C. Dao, J. Wang, *Chem. Commun.* **2010**, *46*, 1623.
[230] G. Loget, A. Kuhn, *Nat. Commun.* **2011**, *2*, 535.
[231] A. M. Brooks, M. Tasinkevych, S. Sabrina, D. Velegol, A. Sen, K. J. M. Bishop, *Nat. Commun.* **2019**, *10*, 495.
[232] J. Wang, W. Gao, *ACS Nano* **2012**, *6*, 5745.
[233] a) K. Kim, X. B. Xu, J. H. Guo, D. L. Fan, *Nat. Commun.* **2014**, *5*, 3632; b) X. Xu, K. Kim, D. Fan, *Angew. Chem., Int. Ed.* **2015**, *54*, 2525.
[234] J. H. Guo, K. Kim, K. W. Lei, D. L. Fan, *Nanoscale* **2015**, *7*, 11363.
[235] K. Kim, Z. X. Liang, M. L. Liu, D. L. Fan, *ACS Appl. Mater. Interfaces* **2017**, *9*, 6144.
[236] J. Sachs, K. I. Morozov, O. Kenneth, T. Qiu, N. Segreto, P. Fischer, A. M. Leshansky, *Phys. Rev. E* **2018**, *98*, 063105.
[237] K. Ichimura, S. K. Oh, M. Nakagawa, *Science* **2000**, *288*, 1624.
[238] A. Diguet, R. M. Guillermic, N. Magome, A. Saint-Jalmes, Y. Chen, K. Yoshikawa, D. Baigl, *Angew. Chem., Int. Ed.* **2009**, *121*, 9445.
[239] Y. Norikane, S. Tanaka, E. Uchida, *CrystEngComm* **2016**, *18*, 7225.
[240] Y. L. Liang, Y. B. Xu, W. Ye, D. H. Yao, Y. H. Chen, C. Y. Wang, *J. Mater. Chem. A* **2018**, *6*, 16838.
[241] A. Venancio-Marques, D. Baigl, *Langmuir* **2014**, *30*, 4207.

[242] N. Kavokine, M. Anyfantakis, M. Morel, S. Rudiuk, T. Bickel, D. Baigl, *Angew. Chem., Int. Ed.* **2016**, *55*, 11183.
[243] M. Xiao, C. Jiang, F. Shi, *NPG Asia Mater* **2014**, *6*, e128.
[244] M. Xiao, M. J. Cheng, Y. J. Zhang, F. Shi, *Small* **2013**, *9*, 2509.
[245] W. Wang, Y.-Q. Liu, Y. Liu, B. Han, H. Wang, D.-D. Han, J.-N. Wang, Y.-L. Zhang, H.-B. Sun, *Adv. Funct. Mater.* **2017**, *27*, 1702946.
[246] A. Kausar, H. Nagano, T. Ogata, T. Nonaka, S. Kurihara, *Angew. Chem., Int. Ed.* **2009**, *48*, 2144.
[247] M. Manjare, F. C. Yang, R. Qiao, Y. P. Zhao, *J. Phys. Chem. C* **2015**, *119*, 28361.
[248] C. Chen, F. Soto, E. Karshalev, J. Li, J. Wang, *Adv. Funct. Mater.* **2019**, *29*, 1806290.
[249] J. Li, T. Li, T. Xu, M. Kiristi, W. Liu, Z. Wu, J. Wang, *Nano Lett.* **2015**, *15*, 4814.
[250] L. Q. Ren, W. Wang, T. E. Mallouk, *Acc. Chem. Res.* **2018**, *51*, 1948.
[251] R. M. Hormigos, B. J. Sánchez, A. Escarpa, *Angew. Chem., Int. Ed.* **2019**, *58*, 3128.
[252] S. Tang, F. Zhang, J. Zhao, W. Talaat, F. Soto, E. Karshalev, C. Chen, Z. Hu, X. Lu, J. Li, Z. Lin, H. Dong, X. Zhang, A. Nourhani, J. Wang, *Adv. Funct. Mater.* **2019**, *29*, 1809003.
[253] W. Gao, K. M. Manesh, J. Hua, S. Sattayasamitsathit, J. Wang, *Small* **2011**, *7*, 2047.
[254] Y. G. Dong, M. Liu, H. Zhang, B. Dong, *Nanoscale* **2016**, *8*, 8378.
[255] Z. H. Li, L. J. Bai, C. Zhou, X. H. Yan, L. Mair, A. N. Zhang, L. Zhang, W. Wang, *Part. Part. Syst. Charact.* **2017**, *34*, 1600277.
[256] V. Magdanz, S. Sanchez, O. G. Schmidt, *Adv. Mater.* **2013**, *25*, 6581.
[257] M. Medina-Sánchez, L. Schwarz, A. K. Meyer, F. Hebenstreit, O. G. Schmidt, *Nano Lett.* **2016**, *16*, 555.
[258] C. Chen, X. Chang, P. Angsantikul, J. Li, B. E. de Ávila, E. Karshalev, W. Liu, F. Mou, S. He, R. Castillo, Y. Liang, J. Guan, L. Zhang, J. Wang, *Adv. Biosyst.* **2018**, *2*, 1700160.
[259] H. F. Xu, M. Medina-Sanchez, V. Magdanz, L. Schwarz, F. Hebenstreit, O. G. Schmidt, *ACS Nano* **2018**, *12*, 327.
[260] Y. F. Tu, F. Peng, A. A. M. André, Y. J. Men, M. Srinivas, D. A. Wilson, *ACS Nano* **2017**, *11*, 1957.
[261] H. Wang, M. G. Patroz, J. A. Jackman, B. Khezri, T. Maric, N.-J. Cho, M. Pumera, *Adv. Funct. Mater.* **2017**, *27*, 1702338.
[262] F. Soto, M. A. Lopez-Ramirez, I. Jeerapan, B. Esteban-Fernandez de Avila, R. K. Mishra, X. Lu, I. Chai, C. Chen, D. Kupor, A. Nourhani, J. Wang, *Adv. Funct. Mater.* **2019**, *29*, 1900658.
[263] Y. B. Zhang, K. Yan, F. T. Ji, L. Zhang, *Adv. Funct. Mater.* **2018**, *28*, 1806340.
[264] M. M. Stanton, B.-W. Park, A. Miguel-Lopez, X. Ma, M. Sitti, S. Sanchez, *Small* **2017**, *13*, 1603679.
[265] B.-W. Park, J. Zhuang, O. Yasa, M. Sitti, *ACS Nano* **2017**, *11*, 8910.
[266] M. M. Stanton, B.-W. Park, D. Vilela, K. Bente, D. Faivre, M. Sitti, S. Sanchez, *ACS Nano* **2017**, *11*, 9968.
[267] Z. Hosseinidoust, B. Mostaghaci, O. Yasa, B.-W. Park, A. V. Singh, M. Sitti, *Adv. Drug Delivery Rev.* **2016**, *106*, 27.
[268] Y. Alapan, O. Yasa, O. Schauer, J. Giltinan, A. F. Tabak, V. Sourjik, M. Sitti, *Sci. Rob.* **2018**, *3*, eaar4423.
[269] P. Illien, R. Golestanian, A. Sen, *Chem. Soc. Rev.* **2017**, *46*, 5508.
[270] a) H. Wang, M. Pumera, *Chem. Soc. Rev.* **2020**, *49*, 3211; b) B. Wang, Y. Zhang, Z. Guo, L. Zhang, *Mater. Today* **2019**, *25*, 112.
[271] B. Wang, F. Ji, J. Yu, L. Yang, Q. Wang, L. Zhang, *iScience* **2019**, *19*, 760.
[272] F. Mou, J. Zhang, Z. Wu, D. Du, Z. Zhang, L. Xu, J. Guan, *iScience* **2019**, *19*, 415.
[273] E. Lauga, T. R. Powers, *Rep. Prog. Phys.* **2009**, *72*, 096601.
[274] M. Ibele, T. E. Mallouk, A. Sen, *Angew. Chem., Int. Ed.* **2009**, *48*, 3308.
[275] G. Calzaferri, *Catal. Today* **1997**, *39*, 145.
[276] J. Palacci, S. Sacanna, A. P. Steinberg, D. J. Pine, P. M. Chaikin, *Science* **2013**, *339*, 936.
[277] I. Buttinoni, J. Bialké, F. Kümmel, H. Löwen, C. Bechinger, T. Speck, *Phys. Rev. Lett.* **2013**, *110*, 238301.
[278] Y. Hong, M. Diaz, U. M. Córdova-Figueroa, A. Sen, *Adv. Funct. Mater.* **2010**, *20*, 1568.
[279] Z. H. Lin, T. Y. Si, Z. G. Wu, C. Y. Gao, X. K. Lin, Q. He, *Angew. Chem., Int. Ed.* **2017**, *56*, 13517.
[280] Y. R. Gao, F. Z. Mou, Y. Z. Feng, S. P. Che, W. Li, L. L. Xu, J. G. Guan, *ACS Appl. Mater. Interfaces* **2017**, *9*, 22704.
[281] D. Feldmann, S. R. Maduar, M. Santer, N. Lomadze, O. I. Vinogradova, S. Santer, *Sci. Rep.* **2016**, *6*, 36443.
[282] B. M. Tansi, M. L. Peris, O. E. Shklyaev, A. C. Balazs, A. Sen, *Angew. Chem., Int. Ed.* **2019**, *58*, 2295.
[283] a) J. Yu, T. Xu, Z. Lu, C. Vong, L. Zhang, *IEEE Trans. Rob.* **2017**, *33*, 1213; b) Q. Wang, J. Yu, K. Yuan, L. Yang, D. Jin, L. Zhang, *Appl. Mater. Today* **2020**, *18*, 100489.
[284] a) J. Yu, L. Yang, L. Zhang, *Int. J. Rob. Res.* **2018**, *37*, 912; b) J. Yu, Q. Wang, M. Li, C. Liu, L. Wang, T. Xu, L. Zhang, *IEEE Rob. Autom. Lett.* **2019**, *4*, 2942.
[285] a) D. D. Jin, J. F. Yu, K. Yuan, L. Zhang, *ACS Nano* **2019**, *13*, 5999; b) F. Ji, B. Wang, L. Zhang, *Research* **2020**, *2020*, 6380794.
[286] H. Xie, M. Sun, X. Fan, Z. Lin, W. Chen, L. Wang, L. Dong, Q. He, *Sci. Rob.* **2019**, *4*, eaav8006.
[287] J. F. Yu, B. Wang, X. Z. Du, Q. Q. Wang, L. Zhang, *Nat. Commun.* **2018**, *9*, 3260.
[288] a) F. Ji, D. Jin, B. Wang, L. Zhang, *ACS Nano* **2020**, *14*, 6990; b) J. Yu, D. Jin, K. Chan, K. Yuan, L. Zhang, *Nat. Commun.* **2019**, *10*, 5631.
[289] a) K. Terayama, H. Habe, M. Sakagami, *IPSJ Transactions on Computer Vision and Applications* **2016**, *8*, 4; b) R. F. Storms, C. Carere, F. Zoratto, C. K. Hemelrijk, *Behav. Ecol. Sociobiol.* **2019**, *73*, 10.
[290] D. Ahmed, T. Baasch, N. Blondel, N. Laubli, J. Dual, B. J. Nelson, *Nat. Commun.* **2017**, *8*, 770.
[291] D. K. Zhou, Y. Gao, J. J. Yang, Y. C. Li, G. B. Shao, G. Y. Zhang, T. L. Li, L. Q. Li, *Adv. Sci.* **2018**, *5*, 1800122.
[292] L. Shang, S. Dong, G. U. Nienhaus, *Nano Today* **2011**, *6*, 401.
[293] X. Wu, H. Liu, J. Liu, K. N. Haley, J. A. Treadway, J. P. Larson, N. Ge, F. Peale, M. P. Bruchez, *Nat. Biotechnol.* **2003**, *21*, 41.
[294] Y. Ma, H. Su, X. Kuang, X. Li, T. Zhang, B. Tang, *Anal. Chem.* **2014**, *86*, 11459.
[295] M. Sitti, H. Ceylan, W. Hu, J. Giltinan, M. Turan, S. Yim, E. Diller, *Proc. IEEE* **2015**, *103*, 205.
[296] J. Christensen, L. Norgaard, R. Bro, S. B. Engelsen, *Chem. Rev.* **2006**, *106*, 1979.
[297] M. Chen, M. Yin, *Prog. Polym. Sci.* **2014**, *39*, 365.
[298] K. D. Wegner, N. Hildebrandt, *Chem. Soc. Rev.* **2015**, *44*, 4792.
[299] X. Michalet, F. F. Pinaud, L. A. Bentolila, J. M. Tsay, S. Doose, J. J. Li, G. Sundaresan, A. M. Wu, S. S. Gambhir, S. Weiss, *Science* **2005**, *307*, 538.
[300] a) G. Hong, S. Diao, A. L. Antaris, H. Dai, *Chem. Rev.* **2015**, *115*, 10816; b) L. Yang, Y. Zhang, Q. Wang, K. Chan, L. Zhang, *IEEE Trans. Autom. Sci. Eng.* **2020**, *17*, 490.
[301] B. Jurado-Sánchez, M. Pacheco, J. Rojo, A. Escarpa, *Angew. Chem., Int. Ed.* **2017**, *56*, 6957.
[302] B. Wang, Y. B. Zhang, L. Zhang, *Quant. Imaging Med. Surg.* **2018**, *8*, 461.
[303] D. L. Ni, W. B. Bu, E. B. Ehlerding, W. B. Cai, J. L. Shi, *Chem. Soc. Rev.* **2017**, *46*, 7438.
[304] D. Faivre, D. Schuler, *Chem. Rev.* **2008**, *108*, 4875.

[305] S. Martel, O. Felfoul, J. B. Mathieu, A. Chanu, S. Tamaz, M. Mohammadi, M. Mankiewicz, N. Tabatabaei, *Int. J. Rob. Res.* **2009**, *28*, 1169.
[306] O. Felfoul, S. Martel, *Biomed. Microdevices* **2013**, *15*, 1015.
[307] D. de Lanauze, O. Felfoul, J. P. Turcot, M. Mohammadi, S. Martel, *Int. J. Rob. Res.* **2014**, *33*, 359.
[308] S. Taherkhani, M. Mohammadi, J. Daoud, S. Martel, M. Tabrizian, *ACS Nano* **2014**, *8*, 5049.
[309] S. Martel, C. C. Tremblay, S. Ngakeng, G. Langlois, *Appl. Phys. Lett.* **2006**, *89*, 233904.
[310] S. Martel, M. Mohammadi, O. Felfoul, Z. Lu, P. Pouponneau, *Int. J. Rob. Res.* **2009**, *28*, 571.
[311] B. Behkam, M. Sitti, in *Int. Conf. on Advanced Intelligent Mechanotronics*, IEEE, Piscataway, NJ **2005**, p. 37.
[312] A. Sanchez, A. Magdanz, O. G. Schmidt, S. Misra, in *5th IEEE RAS & EMBS Int. Conf. on Biomedical Robotics and Biomechatronics (BioRob)*, IEEE, Piscataway, NJ **2014**, p. 169.
[313] E. S. Olson, J. Orozco, Z. Wu, C. D. Malone, B. Yi, W. Gao, M. Eghtedari, J. Wang, R. F. Mattrey, *Biomaterials* **2013**, *34*, 8918.
[314] I. S. M. Khalil, P. Ferreira, R. Eleuterio, C. L. Korte, S. Misra, in *IEEE Int. Conf. on Robotics & Automation (ICRA)*, IEEE, Piscataway, NJ **2014**, p. 3807.
[315] J. Peng, Z. F. Qin, S. P. Chen, in *2016 IEEE Int. Ultrasonics Symp. (IUS) Tours*, (Ed: S. Freear) IEEE, Piscataway, NJ **2016**, p. 1.
[316] Q. Wang, L. Yang, J. Yu, P. Chiu, Y. Zheng, L. Zhang, *IEEE Trans. Biomed. Eng.* **2020**, https://doi.org/10.1109/TBME.2020.2987045.
[317] Q. Wang, L. Zhang, *IEEE Open J. Nanotechnol.* **2020**, *1*, 6.
[318] Q. Wang, B. Wang, J. Yu, K. Schweizer, B. J. Nelson, L. Zhang, in *IEEE Int. Conf. on Robotics and Automation (ICRA2020)*, IEEE, Piscataway, NJ **2020**.
[319] S. Scheggi, K. K. T. Chandrasekar, C. Yoon, B. Sawaryn, G. Steeg, D. H. Gracias, S. Misra, in *2017 IEEE Int. Conf. on Robotics and Automation (ICRA)*, IEEE, Piscataway, NJ **2017**, p. 6156.
[320] S. L. Pimlott, A. Sutherland, *Chem. Soc. Rev.* **2011**, *40*, 149.
[321] L. Cunha, I. Horvath, S. Ferreira, J. Lemos, P. Costa, D. Vieira, D. S. Veres, K. Szigeti, T. Summavielle, D. Máthé, L. F. Metello, *Mol. Diagn. Ther.* **2014**, *18*, 153.
[322] Z. Wu, L. Li, Y. Yang, P. Hu, Y. Li, S. Y. Yang, L. Wang, W. Gao, *Sci. Rob.* **2019**, *4*, eaax0613.
[323] a) J. T. Kim, U. Choudhury, H.-H. Jeong, P. Fischer, *Adv. Mater.* **2017**, *29*, 1701024; b) X. Lin, B. Xu, H. Zhu, J. Liu, A. Solovev, Y. Mei, *Research* **2020**, *2020*, 7659749.
[324] Y. B. Zhang, L. Zhang, L. D. Yang, C. I. Vong, K. F. Chan, W. K. K. Wu, T. N. Y. Kwong, N. W. S. Lo, M. Ip, S. H. Wong, J. J. Y. Sung, P. W. Y. Chiu, L. Zhang, *Sci. Adv.* **2019**, *5*, eaau9650.
[325] Y. Zhang, K. Yuan, L. Zhang, *Adv. Mater. Technol.* **2019**, *4*, 1800636.
[326] P. Xu, Y. Yu, T. Li, H. Chen, Q. Wang, M. Wang, M. Wan, C. Mao, *Anal. Chim. Acta 1129*, 60, **2020**.
[327] C. S. Mayorga-Martinez, M. Pumera, *Adv. Funct. Mater.* **2020**, *30*, 1906449.
[328] J. Orozco, A. Cortés, G. Cheng, S. Sattayasamitsathit, W. Gao, X. Feng, Y. Shen, J. Wang, *J. Am. Chem. Soc.* **2013**, *135*, 5336.
[329] V. V. Singh, A. Martin, K. Kaufmann, S. D. S. de Oliveira, J. Wang, *Chem. Mater.* **2015**, *27*, 8162.
[330] J. Orozco, B. Jurado-Sánchez, G. Wagner, W. Gao, R. Vazquez-Duhalt, S. Sattayasamitsathit, M. Galarnyk, A. Cortés, D. Saintillan, J. Wang, *Langmuir* **2014**, *30*, 5082.
[331] V. V. Singh, K. Kaufmann, B. Esteban-Fernández de Ávila, E. Karshalev, J. Wang, *Adv. Funct. Mater.* **2016**, *26*, 6270.
[332] Y. Yoshizumi, K. Okubo, M. Yokokawa, H. Suzuki, *Langmuir* **2016**, *32*, 9381.
[333] B. E. de Ávila, P. Angsantikul, D. E. Ramírez-Herrera, F. Soto, H. Teymourian, D. Dehaini, Y. J. Chen, L. F. Zhang, J. Wang, *Sci. Rob.* **2018**, *3*, eaat0485.
[334] B. E. de Avila, A. Martin, F. Soto, M. A. Lopez-Ramirez, S. Campuzano, G. M. Vasques-Machado, W. Gao, L. Zhang, J. Wang, *ACS Nano* **2015**, *9*, 6756.
[335] S. Honda, Y. Kirino, *Nucleic Acids Res.* **2015**, *43*, e77.
[336] T. Wu, T. A. Nieminen, S. Mohanty, J. Miotke, R. L. Meyer, H. Rubinsztein-Dunlop, M. W. Berns, *Nat. Photonics* **2012**, *6*, 62.
[337] L. Liu, B. Chen, K. Liu, J. Gao, Y. Ye, Z. Wang, N. Qin, D. A. Wilson, Y. Tu, F. Peng, *Adv. Funct. Mater.* **2020**, *30*, 1910108.
[338] V. Iacovacci, L. Ricotti, E. Sinibaldi, G. Signore, F. Vistoli, A. Menciassi, *Adv. Sci.* **2018**, *5*, 1800807.
[339] R. Fernandes, D. H. Gracias, *Mater. Today* **2009**, *12*, 14.
[340] K. Malachowski, M. Jamal, Q. Jin, B. Polat, C. J. Morris, D. H. Gracias, *Nano Lett.* **2014**, *14*, 4164.
[341] E. Gultepe, J. S. Randhawa, S. Kadam, S. Yamanaka, F. M. Selaru, E. J. Shin, A. N. Kalloo, D. H. Gracias, *Adv. Mater.* **2013**, *25*, 514.
[342] J. Pokki, O. Ergeneman, G. Chatzipirpiridis, T. Luhmann, J. Sort, E. Pellicer, S. A. Pot, B. M. Spiess, S. Pane, B. J. Nelson, *J. Biomed. Mate. Res., Part B* **2017**, *105*, 836.
[343] M. Kummer, J. Abbott, B. Kratochvil, R. Borer, A. Sengul, B. Nelson, *IEEE Trans. Rob.* **2010**, *26*, 1006.
[344] F. Ullrich, C. Bergeles, J. Pokki, O. Ergeneman, S. Erni, G. Chatzipirpiridis, S. Pane, C. Framme, B. J. Nelson, *IOVS* **2013**, *54*, 2853.
[345] Z. Wu, J. Troll, H. Jeong, Q. Wei, M. Stang, F. Ziemssen, Z. Wang, M. Dong, S. Schnichels, T. Qiu, P. Fischer, *Sci. Adv.* **2018**, *4*, eaat4388.
[346] a) P. Erkoc, I. C. Yasa, H. Ceylan, O. Yasa, Y. Alapan, M. Sitti, *Adv. Ther.* **2019**, *2*, 1800064; b) S. H. Wang, K. Liu, F. Wang, F. Peng, Y. F. Tu, *Chem. – Asian J.* **2019**, *14*, 2336.
[347] G. Chen, Y. Yu, X. Wu, G. Wang, G. Gu, F. Wang, J. Ren, H. Zhang, Y. Zhao, *Research* **2019**, *2019*, 6175398.
[348] D. Cheng, X. Zhang, Y. Chen, H. Chen, Z. Qiao, H. Wang, *iScience* **2020**, *23*, 101144.
[349] O. S. Fenton, K. N. Olafson, P. S. Pillai, M. J. Mitchell, R. Langer, *Adv. Mater.* **2018**, *30*, 1705328.
[350] D. Chu, X. Dong, X. Shi, C. Zhang, Z. Wang, *Adv. Mater.* **2018**, *30*, 1706245.
[351] T. Simon-Yarza, A. Mielcarek, P. Couvreur, C. Serre, *Adv. Mater.* **2018**, *30*, 1707365.
[352] X. Yan, J. Xu, Q. Zhou, D. Jin, C. Vong, Q. Feng, D. Ng, L. Bian, L. Zhang, *Appl. Mater. Today* **2019**, *15*, 242.
[353] Q. Zhou, T. Petit, H. Choi, B. Nelson, L. Zhang, *Adv. Funct. Mater.* **2017**, *27*, 1604571.
[354] L. Zhang, T. Petit, Y. Lu, B. Kratochvil, K. Peyer, R. Pei, J. Lou, B. Nelson, *ACS Nano* **2010**, *4*, 6228.
[355] S. Tang, F. Zhang, H. Gong, F. Wie, J. Zhuang, E. Karshalev, B. E. de Ávila, C. Huang, Z. Zhou, Z. Li, L. Yin, H. Dong, R. H. Fang, X. Zhang, L. Zhang, J. Wang, *Sci. Rob.* **2020**, *5*, eaba6137.
[356] Y. Q. Zhang, J. C. Yu, H. N. Bomba, Y. Zhu, Z. Gu, *Chem. Rev.* **2016**, *116*, 12536.
[357] J. Wen, K. Yang, F. Y. Liu, H. J. Li, Y. Q. Xu, S. G. Sun, *Chem. Soc. Rev.* **2017**, *46*, 6024.
[358] F. Peng, Y. F. Tu, D. A. Wilson, *Chem. Soc. Rev.* **2017**, *46*, 5289.
[359] J. R. Baylis, J. H. Yeon, M. H. Thomson, A. Kazerooni, X. Wang, A. E. St. John, E. B. Lim, D. Chien, A. Lee, J. Q. Zhang, J. M. Piret, L. S. Machan, T. F. Burke, N. J. White, C. J. Kastrup, *Sci. Adv.* **2015**, *1*, e1500379.
[360] W. P. He, J. Frueh, N. Hu, L. P. Liu, M. Y. Cai, Q. He, *Adv. Sci.* **2016**, *3*, 1600206.
[361] W. Li, L. Y. Zhang, X. H. Ge, B. Y. Xu, W. X. Zhang, L. L. Qu, C.-H. Choi, J. H. Xu, A. F. Zhang, H. Lee, D. A. Weitz, *Chem. Soc. Rev.* **2018**, *47*, 5646.

[362] S. K. Srivastava, M. Medina-Sánchez, B. Koch, O. G. Schmidt, *Adv. Mater.* **2016**, *28*, 832.
[363] D. Patra, S. Sengupta, W. T. Duan, H. Zhang, R. Pavlick, A. Sen, *Nanoscale* **2013**, *5*, 1273.
[364] S. Sattayasamitsathit, H. Kou, W. Gao, W. Thavarajah, K. Kaufmann, L. F. Zhang, J. Wang, *Small* **2014**, *10*, 2830.
[365] B. Esteban-Fernández de Ávila, P. Angsantikul, J. X. Li, W. Gao, L. F. Zhang, J. Wang, *Adv. Funct. Mater.* **2018**, *28*, 1705640.
[366] L. L. Wang, H. L. Zhu, Y. Shi, Y. Ge, X. M. Feng, R. Q. Liu, Y. Li, Y. W. Ma, L. H. Wang, *Nanoscale* **2018**, *10*, 11384.
[367] A. V. Singh, Z. Hosseinidoust, B.-W. Park, O. Yasa, M. Sitti, *ACS Nano* **2017**, *11*, 9759.
[368] M. Luo, Y. Z. Feng, T. W. Wang, J. G. Guan, *Adv. Funct. Mater.* **2018**, *28*, 1706100.
[369] W. Gao, J. Wang, *Nanoscale* **2014**, *6*, 10486.
[370] A. Pourazary, A. Katzenberg, W. Gao, Y. F. Shen, J. Wang, *ACS Nano* **2013**, *7*, 9232.
[371] X. Wei, M. Beltran-Gastelum, E. Karshalev, B. Esteban-Fernandez de Avila, J. Zhou, D. Ran, P. Angsantikul, R. H. Fang, J. Wang, L. Zhang, *Nano Lett.* **2019**, *19*, 1914.
[372] J. X. Li, P. Angsantikul, W. J. Liu, B. E. de Avila, S. Thamphiwatana, M. L. Xu, E. Sandraz, X. L. Wang, J. Delezuk, W. W. Gao, L. F. Zhang, J. Wang, *Angew. Chem., Int. Ed.* **2017**, *56*, 2156.
[373] E. Karshalev, B. E. de Ávila, M. Beltrán-Gastélum, P. Angsantikul, S. S. Tang, R. Mundaca-Uribe, F. Y. Zhang, J. Zhao, L. F. Zhang, J. Wang, *ACS Nano* **2018**, *12*, 8397.
[374] W. Gao, R. F. Dong, S. Thamphiwatana, J. X. Li, W. W. Gao, L. F. Zhang, J. Wang, *ACS Nano* **2015**, *9*, 117.
[375] B. E. de ávila, P. Angsantikul, J. X. Li, M. A. Lopez-Ramirez, D. E. Ramírez-Herrera, S. Thamphiwatana, C. R. Chen, J. Delezuk, R. Samakapiruk, V. Ramez, M. Obonyo, L. F. Zhang, J. Wang, *Nat. Commun.* **2017**, *8*, 272.
[376] A. C. Hortelão, T. Patiño, A. Perez-Jiménez, À. Blanco, S. Sánchez, *Adv. Funct. Mater.* **2018**, *28*, 1705086.
[377] K. Villa, L. Krejčová, F. Novotný, Z. Heger, Z. Sofer, M. Pumera, *Adv. Funct. Mater.* **2018**, *28*, 1804343.
[378] Q. Liu, K. Zhao, C. Wang, Z. Z. Zhang, C. X. Zheng, Y. Zhao, Y. D. Zheng, C. Y. Liu, Y. L. An, L. Q. Shi, C. S. Kang, Y. Liu, *Adv. Sci.* **2019**, *6*, 1801423.
[379] Y. J. Liu, P. Bhattarai, Z. F. Dai, X. Y. Chen, *Chem. Soc. Rev.* **2019**, *48*, 2053.
[380] D. Xu, C. Zhou, C. Zhan, Y. Wang, Y. You, X. Pan, J. Jiao, R. Zhang, Z. Dong, W. Wang, X. Ma, *Adv. Funct. Mater.* **2019**, *29*, 1807727.
[381] A. C. Hortelão, R. Carrascosa, N. Murillo-Cremaes, T. Patino, S. Sánchez, *ACS Nano* **2019**, *13*, 429.
[382] N. Korin, M. Kanapathipillai, B. D. Matthews, M. Crescente, A. Brill, T. Mammoto, K. Ghosh, S. Jurek, S. A. Bencherif, D. Bhatta, A. U. Coskun, C. L. Feldman, D. D. Wagner, D. E. Ingber, *Science* **2012**, *337*, 738.
[383] a) M. Dong, X. Wang, X. Chen, F. Mushtaq, S. Deng, C. Zhu, H. Torlakcik, A. Terzopoulou, X. Qin, X. Xiao, J. Puigmartí-Luis, H. Choi, A. P. Pêgo, Q. Shen, B. J. Nelson, S. Pané, *Adv. Funct. Mater.* **2020**, *30*, 1910323; b) I. C. Yasa, A. F. Tabak, O. Yasa, H. Ceylan, M. Sitti, *Adv. Funct. Mater.* **2019**, *29*, 1808992.
[384] a) G. Go, S.-G. Jeong, A. Yoo, J. Han, B. Kang, K. T. Nguy, Z. Jin, C.-S. Kim, Y. R. Seo, J. Y. Kang, J. Y. Na, E. K. Song, Y. Jeong, J. K. Seon, J.-O. Park, E. Choi, *Sci. Rob.* **2020**, *5*, eaay6626; b) S. Jeon, S. Kim, S. Ha, S. Lee, E. Kim, S. Y. Kim, S. H. Park, J. H. Jeon, S. W. Kim, C. Moon, B. J. Nelson, J.-Y. Kim, S.-W. Yu, H. Choi, *Sci. Rob.* **2019**, *4*, eaav4317.
[385] R. Cheng, W. J. Huang, L. J. Huang, B. Yang, L. D. Mao, K. L. Jin, Q. C. ZhuGe, Y. P. Zhao, *ACS Nano* **2014**, *8*, 7746.
[386] I. S. M. Khalil, A. F. Tabak, K. Sadek, D. Mahdy, N. Hamdi, M. Sitti, *IEEE Rob. Autom. Lett.* **2017**, *2*, 927.
[387] I. S. M. Khalil, D. Mahdy, A. E. Sharkawy, R. R. Moustafa, A. F. Tabak, M. E. Mitwally, S. Hesham, N. Hamdi, A. Klingner, A. Mohamed, M. Sitti, *IEEE Rob. Autom. Lett.* **2018**, *3*, 1112.
[388] H. H. Engelhard, S. P. Pernal, Z. A. Gaertner, A. G. Levin, Y. Y. Pan, S. C. Morris, M. E. Sabo, F. M. Creighton, *IEEE Magn. Lett.* **2017**, *8*, 1.
[389] J. X. Shao, M. Abdelghani, G. Z. Shen, S. P. Cao, D. S. Williams, J. C. M. van Hest, *ACS Nano* **2018**, *12*, 4877.
[390] M. Xie, W. Zhang, C. Fan, C. Wu, Q. Feng, J. Wu, Y. Li, R. Gao, Z. Li, Q. Wang, Y. Cheng, B. He, *Adv. Mater.* **2020**, *32*, 2000366.
[391] A. Ghosh, W. Xu, N. Gupta, D. H. Gracias, *Nano Today* **2020**, *31*, 100836.
[392] T. O. Tasci, D. Disharoon, R. M. Schoeman, K. Rana, P. S. Herson, D. W. M. Marr, K. B. Neeves, *Small* **2017**, *13*, 1700954.
[393] N. K. Rajendran, S. S. D. Kumar, N. N. Houreld, H. Abrahamse, *J. Drug Delivery Sci. Technol.* **2018**, *44*, 421.
[394] N. Tejavibulya, D. A. M. Colburn, F. A. Marcogliese, K. Yang, V. Guo, S. Chowdhury, M. N. Stojanovic, S. K. Sia, *iScience* **2019**, *21*, 328.
[395] X. Zhang, G. Chen, Y. Yu, L. Sun, Y. Zhao, *Research* **2020**, *2020*, 3672120.
[396] W. Gao, A. Pei, X. M. Feng, C. Hennessy, J. Wang, *J. Am. Chem. Soc.* **2013**, *135*, 998.
[397] R. Li, D. Jin, D. Pan, S. Ji, C. Xin, G. Liu, S. Fan, H. Wu, J. Li, Y. Hu, D. Wu, L. Zhang, J. Chu, *ACS Nano* **2020**, *14*, 5233.
[398] O. Felfoul, M. Mohammadi, S. Taherkhani, D. de Lanauze, Y. Xu, D. Loghin, S. Essa, S. Jancik, D. Houle, M. Lafleur, L. Gaboury, M. Tabrizian, N. Kaou, M. Atkin, T. Vuong, G. Batist, N. Beauchemin, D. Radzioch, S. Martel, *Nat. Nanotechnol.* **2016**, *11*, 941.
[399] B. Wang, K. F. Chan, J. F. Yu, Q. Q. Wang, L. D. Yang, P. W. Y. Chiu, L. Zhang, *Adv. Funct. Mater.* **2018**, *28*, 1705701.
[400] Y. Yu, E. Miyako, *iScience* **2018**, *3*, 134.
[401] W. Wang, S. X. Li, L. Mair, S. Ahmed, T. J. Huang, T. E. Mallouk, *Angew. Chem., Int. Ed.* **2014**, *53*, 3201.
[402] D. L. Hu, B. Chan, J. W. M. Bush, *Nature* **2003**, *424*, 663.
[403] B. Wang, W. X. Liang, Z. G. Guo, W. M. Liu, *Chem. Soc. Rev.* **2015**, *44*, 336.
[404] C. Ye, J. Liu, X. Wu, B. Wang, L. Zhang, Y. Zheng, T. Xu, *Micromachines* **2019**, *10*, 175.
[405] X. Wang, C. Hu, L. Schurz, C. D. Marco, X. Chen, S. Pané, B. J. Nelson, *ACS Nano* **2018**, *12*, 6210.
[406] I. S. M. Khalil1, V. Magdanz, S. Sanchez, O. G. Schmidt, S. Misra, *Int. J. Adv. Rob. Syst.* **2015**, *12*, 2.
[407] G. T. van Moolenbroek, T. Patiño, J. Llop, S. Sánchez, *Adv. Intell. Syst.* **2020**, *2*, 2000087.
[408] D. Walker, B. T. Kasdorf, H.-H. Jeong, O. Lieleg, P. Fischer, *Sci. Adv.* **2015**, *1*, e1500501.
[409] Z. Yang, L. Zhang, *Adv. Intell. Syst.* **2020**, *2*, 2000082.
[410] L. D. Yang, Y. B. Zhang, L. Zhang, *IEEE. Trans. Biomed. Eng.* **2019**, *67*, 1517.

Ben Wang obtained his Ph.D. degree at the Department of Biomedical Engineering, The Chinese University of Hong Kong (CUHK), in Prof. Li Zhang's group. Then, he worked as a postdoctoral fellow at the same group in Department of Mechanical and Automation Engineering, supported by the Impact Postdoctoral Fellowship Scheme of CUHK. He joined Shenzhen University in December 2019, as an assistant professor in the College of Chemistry and Environmental Engineering. His current research interests are focused on surface functionalization, magnetic nanoparticles, and soft robots for remote actuation and targeted delivery.

Kostas Kostarelos currently is Professor of Nanomedicine at the Faculty of Biology, Medicine & Health and the National Graphene Institute (NGI) of the University of Manchester and is the Severo Ochoa Distinguished Professor at the Catalan Institute of Nanoscience and Nanotechnology (ICN2). He is a Fellow of the Royal Society of Chemistry (FRSC), Fellow of the Royal Society of Medicine (FRSM), and Fellow of the Royal Society of Arts (FRSA) all in the United Kingdom. In 2010 he was awarded the Japanese Society for the Promotion of Science (JSPS) Professorial Fellowship with the National Institute of Advanced Industrial Science and Technology (AIST) in Tsukuba, Japan. His expertise lies with the biomedical and clinical translation of novel nanomaterials and nanotechnologies and leads nanomedicine labs in the UK and Spain.

Bradley J. Nelson has been the professor of Robotics and Intelligent Systems at ETH Zürich since 2002. Before moving to Europe, Prof. Nelson worked as an engineer at Honeywell and Motorola and served as a United States Peace Corps Volunteer in Botswana, Africa. He has also been a professor at the University of Minnesota and the University of Illinois at Chicago. He has over 30 years of experience in the field of robotics. He serves on the advisory boards of a number of academic departments and research institutes across North America, Europe, and Asia.

Li Zhang received his Ph.D. degree from the University of Basel, Switzerland, in 2007. From 2007 to 2012, he was with the Institute of Robotics and Intelligent Systems, ETH Zürich, Switzerland, as a postdoctoral fellow and then as a senior scientist. He is currently an associate professor in the Department of Mechanical and Automation Engineering, The Chinese University of Hong Kong, and a director of SIAT(CAS)-CUHK Joint Laboratory of Robotics and Intelligent Systems. His main research interests include micro-/nanorobotics for biomedical applications. He is an IEEE NTC distinguished lecturer.